

Thèse de doctorat de l'université Paris VII

Spécialité : Champs, particules, matière

présenté par

Björn Nadrowski

pour obtenir le grade de

Docteur de l'université Paris VII

Propriétés mécaniques de touffes ciliaires actives

soutenu le 22 novembre 2004, devant le jury composé de :

F. Gallet	président
F. Jülicher	directeur
T. Duke	rapporteur
M. Göpfert	rapporteur
P. Martin	
J.-F. Joanny	



Ph.D. thesis of Paris VII University

Specialty: Physics

presented by

Björn Nadrowski

to obtain the title of

Doctor of Paris VII University

Mechanical properties of active hair-bundles

Defended on november 22nd, 2004

Comittee members:

F. Gallet	President
F. Jülicher	Supervisor
T. Duke	Referee
M. Göpfert	Referee
P. Martin	
J.-F. Joanny	

Acknowledgments

The first third of this Ph.D. project took place at the Institut Curie, Paris, while the rest of it was accomplished at the Max-Planck-Institut für Physik komplexer Systeme, Dresden.

I would like to thank my supervisor, Frank Jülicher, for his guidance and help, and Pascal Martin for the time he spent giving me an insight in theoretical and experimental knowledge of hair-bundles and their environment, and for many inspiring discussions.

Many thanks also go to Tom Duke and Martin Göpfert for acting as referees for my thesis, and to François Gallet and Jean-François Joanny for taking part in the committee.

Furthermore, I would like to thank Jacques Prost, Ken Sekimoto, Imre Derényi, and Sebastien Camalet for many interesting discussions during the time I spent at the Institut Curie. Many thanks do also go to Hakim Boukellal, Philippe Girard, Alexander Zumdieck, Christian Simm, Gernot Klein, Tobias Bollenbach, Nilüfer Baba, Nils Becker, Andreas Hilfinger, and many other Ph.D. students at the Institut Curie and the Max-Planck-Institut für Physik komplexer Systeme, for making this hard period a little bit more bearable.

I would like to thank Santhanam, Carsten Svaneborg, Victor Gopar, Mikhail Titov, Janaki Balakrishnan, Anatole Kenfack and many other persons for a lot of discussions about physical and slightly less physical subjects.

In addition, I would like to thank all those people whom I did not mention above. Please consider yourselves thanked!

Special thanks go to my friends Thomas Risler, for his help during the initial part of the writing-up, and who was a great support in many mathematical questions, Karsten Kruse for his moral support, many discussions about all sorts of subjects, and his calmness, Vincent Rossetto for his invaluable help during the last months of my Ph.D.

Another set of special thanks go to Ewa Paluch and Otger Campas for their help in the fierce battle against the evil forces of administration and bureaucracy.

I would like to thank Aneta Panek for her continuous support and love during all the many dark periods which I had during this project.

Finally, I would like to thank my family for their unshakable support and belief in me.

Résumé

L'oreille interne est un des organes sensoriels les plus importants chez les vertébrés. Elle fait preuve d'une performance extraordinaire, avec une grande gamme dynamique, une excellente discrimination fréquentielle et une grande sensibilité.

Il s'agit d'un système qui fait preuve d'activité : l'oreille interne peut émettre des ondes sonores, un phénomène appelé émissions spontanées oto-acoustiques.

Le sens d'audition est basé sur la transformation de stimuli mécaniques en stimuli électriques, tâche accomplie par la cellule sensorielle de l'oreille interne, la cellule ciliée. L'organe mécanosensible de la touffe ciliée est la touffe ciliaire. Les touffes ciliaires du saccule de la grenouille peuvent osciller d'une manière spontanée. Ces oscillations spontanées sont donc un candidat naturel pour la source d'activité de l'oreille interne. Ce travail est une étude théorique des propriétés mécaniques de la touffe ciliaire.

Nous discutons les principes physiques qui sous-tendent la détection d'oscillations basée sur des oscillateurs critiques, ainsi qu'une description détaillée de mécanismes spécifiques qui peuvent mener à un comportement actif et des oscillations spontanées de touffes ciliaires. Nous présentons un diagramme d'états et nous montrons que des fluctuations ont une influence majeure sur les fonctions de réponse du système. Nous discutons des sources différentes de fluctuations et estimons leurs influences sur les propriétés mécaniques de la touffe ciliaire. Les fonctions de réponse linéaire et non-linéaire calculées numériquement sont en accord quantitatif avec des expériences.

Abstract

The inner ear is one of the most important sensitive organs of all vertebrates. It shows an extraordinary performance, with a large dynamic range, high sensitivity and an exquisite frequency selectivity.

The inner ear is not simply a passive detector, but a nonlinear active amplifier. The most striking manifestation of this activity is the fact that the ear does not only detect sound, but it can also emit one to several tones: the so-called spontaneous oto-acoustic emissions.

The auditory sense is based on the transformation of mechanical stimuli into electrical signals, which is done by the sensory cells of the inner ear, the haircells. The mechanosensitive organelle of the haircell is the hair-bundle.

Hair-bundles are active structures, they are namely displaying spontaneous oscillations. These spontaneous oscillations are a natural candidate for the active process underlying the activity of the inner ear. This work is a theoretical study of the mechanical properties of the hair-bundle.

We discuss the physical principles underlying detection based on critical oscillations as well as specific mechanisms that can lead to oscillations and active behavior by hair-bundles. We present a simple description of active hair-bundle mechanics. We calculate the state diagram and show that fluctuations fundamentally change the mechanical response functions. We discuss different sources of fluctuations and estimate their influence on the hair-bundle's mechanical properties. Furthermore, the linear and nonlinear response functions calculated numerically account for the observed properties of active hair-bundles.

Contents

1	Introduction	1
1.1	Hearing in vertebrates	1
1.2	Active amplification in hearing	3
1.3	Amplification by critical oscillators	7
1.4	Biophysics of hair cells	9
1.5	The Gating-Spring model	11
1.6	Spontaneous oscillations of hair-bundles of the sacculus of the bullfrog	15
2	Physical description of hair-bundles	17
2.1	Geometry and displacement variables	17
2.2	Ion-channel gating	21
2.3	Adaptation motors and calcium-feedback	24
2.4	A simple model of the hair-bundle	26
2.4.1	Stationary solutions	27
2.4.2	Dependence of stationary states on the external calcium-concentration	28
2.4.3	The extent spring K_E	31
3	Theory of hair-bundle oscillations	35
3.1	State Diagram	35
3.2	Physical mechanisms of oscillations	37
3.2.1	Fast calcium-feedback	38
3.2.2	Fixed motor position	43
3.2.3	Fast mechanical relaxation	45
3.2.4	Collective motor oscillations	50
3.2.5	Conclusion	52
4	Generic properties of critical oscillators	55

4.1	Hopf bifurcation	55
4.2	Response of stable states	57
4.3	Response of oscillating states	59
4.4	Response of noisy oscillators	61
5	Spontaneous movements and response of hair-bundles in the presence of fluctuations	65
5.1	Experimental observations: linear and nonlinear response	65
5.2	Noise sources in the hair-bundle	66
5.3	Numerical results	70
6	Mechanical response to step-displacements	75
6.1	Calcium-dependent free-energy change: $\Delta G(C)$	81
6.2	Calcium-dependent gating-swing distance: $D(C)$	84
6.3	Calcium-dependent gating-spring stiffness: $K_{GS}(C)$	86
6.4	Calcium-dependent rest-length of the gating-spring: $X_{GS}(C)$	88
6.5	Conclusion	89
7	Discussion and outlook	93
A	Table of Symbols	99
B	Parameter values	105
	Bibliography	109

Chapter 1

Introduction

The human ear is a fantastic organ. Its dynamic range stretches over 6 orders of magnitude of sound-pressures, from ~ 0 - 120 dB, and the audible frequencies cover three orders of magnitude from ~ 20 Hz - 20 kHz, with a frequency discrimination of $\sim 0.2\%$ at ~ 2 kHz. In the inner ear, specialized sensory cells, the haircells, translate the mechanical stimuli of sound waves into nervous signals. The mechanically sensitive organelle of the hair cell is the hair-bundle, a tuft of stiff finger-like structures, called stereocilia, which protrudes from the surface of the cell. This work studies the mechanical properties of the hair-bundle. It is a theoretical and numerical approach to questions that concern some of the physical principles underlying hearing.

1.1 Hearing in vertebrates

All vertebrates have developed structurally similar hearing organs for the detection of sound [48, 75]. Inside the inner ear, several organs are dedicated to different tasks. One is the detection of sound, but the inner ear also hosts the sense of balance, i.e. structures devoted to the detection of the head's posture as well as its linear and angular accelerations. In mammals, the organ specialized in the detection of sound is the cochlea [20]. Lower vertebrates have developed organs resembling the cochlea. In all of the organs of the inner ear, the hair cells translate mechanical stimuli into electrical signals, a process called mechano-electrical transduction [46].

In mammals, the outer ear works as a kind of hearing horn that collects environmental sound, and concentrates the oscillating air pressure onto the eardrum (fig. 1.1). The middle ear translates the vibrations of the eardrum into an oscillatory pressure difference in the fluids of the inner ear [86]. The last of the bones of the middle ear (the stapes or stirrup) stimulates the oval window, a membrane in the side of the membranous labyrinth. The pressure waves created by the vibrations of the oval window finally enter the cochlea itself, creating a pressure gradient

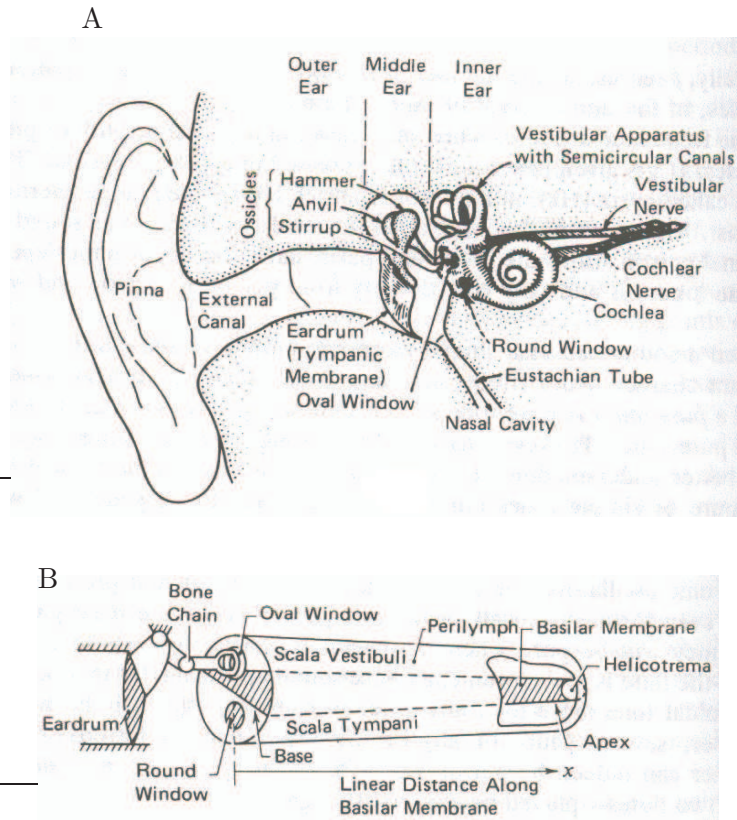


Figure 1.1: Sketch of the human ear. A, Overview of the human ear. Sound waves arrive at the pinna and are transmitted, via the ossicles of the middle ear, to the cochlea. Inside the cochlea, hair cells transform this mechanical signal into an electrical signal which is sent to the central nervous system. B, Schematic drawing of the ear and the cochlea stretched out. Taken from [95].

across the basilar membrane, an elastic membrane inside the cochlea, which is a bone-enclosed spiral with a linear length of about 3.5 cm in humans [20, 93]. This initiates a wave of displacement of the basilar membrane, which travels from its base, the end of the membrane in vicinity to the oval window, to its apex, the end of the membrane situated in the tip of the cochlea's spiral [11, 98, 94].

The organ of Corti, the mechanically sensitive organ of the cochlea, is located on the basilar membrane and consists of sensory cells (hair cells) and supporting cells (fig. 1.2). A human cochlea contains approximately 16000 hair cells in the organ of Corti. Two specialized types of hair cells have developed: the outer hair cells (OHC) and the inner hair cells (IHC). There are three rows of outer hair cells, and one row of inner hair cells. The tips of the hair-bundles of the outer hair cells are attached to the tectorial membrane, a structure which is situated above the organ of Corti. The oscillation of the basilar membrane leads to a shearing displacement of the tectorial membrane with respect to the reticular lamina (the

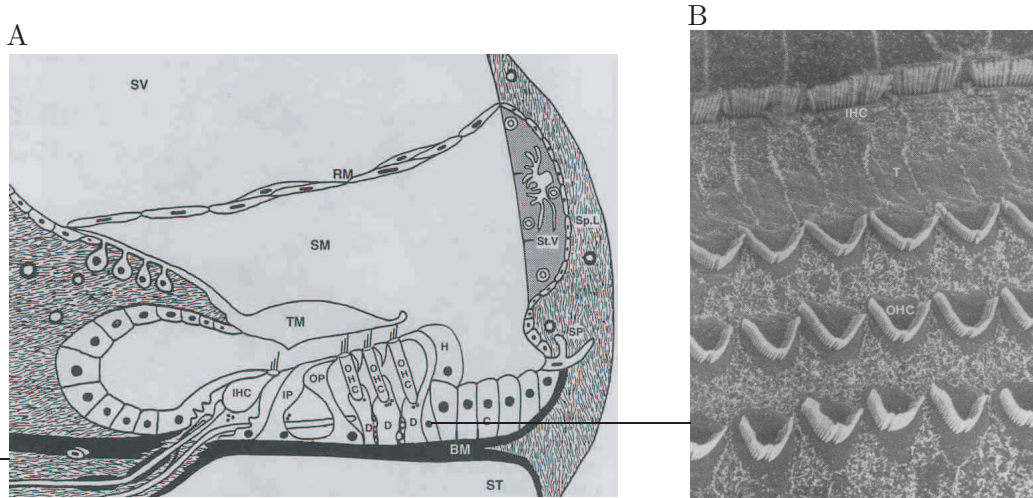


Figure 1.2: Hair cells in the inner ear. A, schematic drawing of the organ of Corti and electron micrograph. The inner hair cells (IHC) and outer hair cells (OHC) are embedded in the elaborate structure of the organ of Corti, which is situated on the basilar membrane (BM). The three separated fluid-filled chambers of the basilar membrane are indicated: Scala Media (SM), Scala Vestibuli (SV), Scala tympani (ST). The tectorial membrane (TM) covers the hair cells. There are three rows of outer hair cells and one row of inner hair cells. B, top view of the organ of Corti. Three rows of W-shaped OHCs and one row of IHCs can be seen. Taken from [20]

apical surface of the hair cells), which is detected by the hair cells and transduced into an electrical signal [46, 48, 92, 29].

Every hair cell has its own characteristic frequency, which is decreasing towards the apex of the basilar membrane [92, 88]. The highest frequencies are located close to the base whereas the lowest frequencies are detected close to the apex of the basilar membrane, in the tip of the spiral which forms the cochlea.

1.2 Active amplification in hearing

More than 100 years ago, von Helmholtz described the cochlea as a series of independent passive resonant elements [38]. He separated the process of sound detection into two processes: he assumed a nonlinear process in the middle ear, while the cochlea was assumed to be a linear sound detector, the analog of a Fourier-Analyzer, resembling a set of strings each with a different characteristic frequency, excited by the sound wave entering the cochlea.

Von Békésy's experiments on the cochleae of dead humans and animals described the passive mechanics of the cochlea [11]. He found that vibrations of the stapes induce a traveling wave of displacements of the basilar membrane, beginning at the base and then going to the apex. The frequency selectivity at a given point on the basilar membrane was found to be very poor, which was inferred from the

width of the curve described by the amplitude of basilar-membrane displacements for varying frequencies, called the tuning curve.

Measurements of the motion of the basilar membrane in living animals, however, showed a very different situation [98, 97, 94]. In contrast to von Békésy's results, the response of the basilar membrane was highly localized, and strongly frequency-dependent. A hint concerning activity of the cochlea was given by the following facts. During the experiment, the condition of the cochlea deteriorated, and that coincided with the observation that the thresholds¹ increased and the tuning curves broadened [86]. The observation that the cochlea's performance is greatly decreased when the animal dies, has led to the assumption that there is indeed an active amplification mechanism at work: the cochlear amplifier [21, 19, 93].

The proposal of an active process underlying the remarkable performances of the cochlea was not new: as early as 1948, Thomas Gold proposed that the ear is an active amplifier and detector [34]. He postulated the presence of a regenerative element in cochlear mechanics, an active element able to overcome the damping effect of hydrodynamic friction.

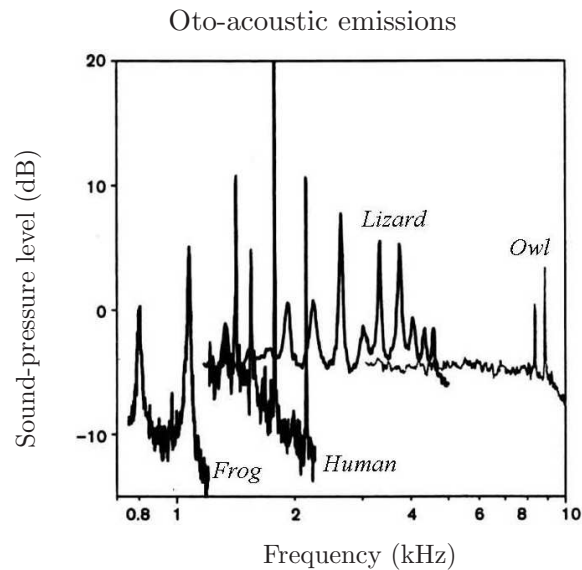


Figure 1.3: Spontaneous oto-acoustic emissions from individuals of different species. Taken from [75]

The most striking manifestation of an active process in the inner ear is given by the spontaneous oto-acoustic emissions [7, 95]. This term refers to the fact that the ears of a variety of vertebrates do not only detect sound, they also emit sound waves at varying frequencies and amplitudes (fig. 1.3). It has been proposed that

¹threshold: the stimulus intensity necessary to produce a certain amplitude of vibration

spontaneous oto-acoustic emissions are the signature of the inner ear's activity [33, 51, 72, 74, 71, 93, 25].

But what is the origin of the active process in the cochlea? Two phenomena at the cellular scale have been identified, which might be at the origin of the active process of the cochlear amplifier. The first one is the observation of somatic electromotility, the electrically induced longitudinal deformation of outer hair cells [9]. Somatic electromotility consists of a rapid elongation and shortening of outer hair cells in response to hyperpolarization or depolarization of their transmembrane potentials [59, 2, 19]. The second possible origin is the activity of the hair-bundle itself. Already in 1985, the turtle cochlear hair cells were proposed to be able to generate forces and show spontaneous oscillations [18]. More recently, it has been demonstrated that spontaneous oscillations of the hair-bundle can amplify its response to sinusoidal stimuli [79]. Furthermore, the spontaneous oscillations of the hair-bundle have been shown to result from an active process in the cell [81]. It has been proposed that myosin motors are involved in the activity of the hair-bundle [100, 50, 10, 32, 41, 5]. These molecular motors are able to generate forces by interaction with actin filaments at the core of the stereocilia of the hair-bundle. In this work, we will study the implications of such an active force-generating mechanism on the mechanics of the hair-bundle.

Spontaneous oto-acoustic emissions (see fig. 1.3) have been found in very different vertebrates, such as frogs [24], lizards [64, 73], birds [105], and humans [95]. Since frogs do not have the elaborate structure of the cochlea, and only mammals possess the outer hair cells which show somatic electromotility, the universal feature of the hearing organs of all these organs is the hair-bundle. It has been proposed that active hair-bundle motility could be involved in the active process underlying the hearing process both in mammals and non-mammals [51, 85, 29, 108]. In order to address general questions concerning the active amplification process involved in hearing, it is therefore useful to study the active mechanics of the hair-bundle.

In the following, we will discuss the activity of the cochlea in more detail. This will help us to compare the observations concerning cochlear mechanics to the observations concerning hair-bundle mechanics.

The cochlea displays four essential properties which can be explained by an active process involved in the hearing process:

- Spontaneous oto-acoustic emissions
- Amplification of weak stimuli
- Frequency-selective amplification
- Compressive nonlinearity of the response to sinusoidal stimuli with varying amplitude, which is well characterized by a power law

To determine the response to weak stimuli and its frequency dependence, the amplitude vibrations or velocities of the basilar membrane are measured. The amplitude of the velocity of this oscillation can be measured as a function of the stimulus sound-pressure amplitude at a given frequency. Every point on the basilar membrane will typically display a behavior as in fig. 1.4, which shows clearly the frequency-dependent response of the basilar membrane. The characteristic frequency of this point of the basilar membrane is about 8 kHz. Another position on the basilar membrane would show a maximum of the sensitivity, defined as the basilar-membrane velocity divided by stimulus pressure, at another frequency.

A

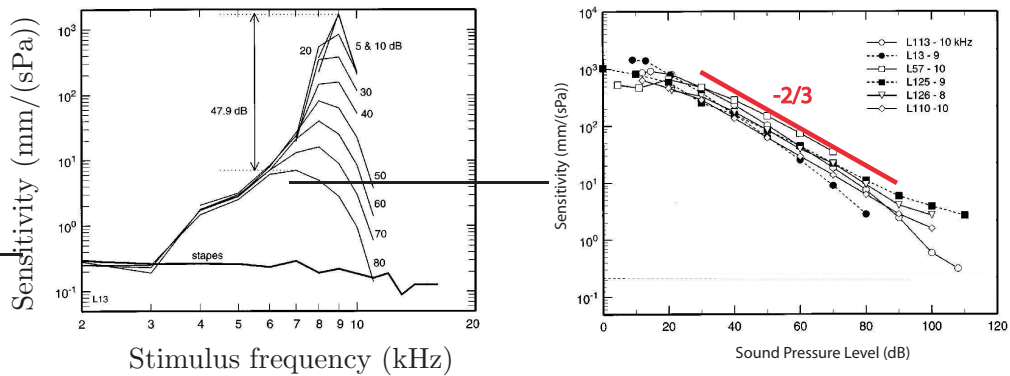


Figure 1.4: Basilar-membrane responses to sound stimuli in the chinchilla cochlea. A, Family of iso-intensity curves showing the sensitivity (basilar-membrane velocity divided by stimulus pressure) as a function of frequency at different stimulus magnitudes. Note the amplitude-dependent location of the most responsive frequency. B, Sensitivity as a function of stimulus pressure, for frequencies between 8 and 10 kHz, which is close to the characteristic frequency of the location of measurement along the axis of the cochlea. The red line indicates a slope of $-2/3$. The different symbols correspond to different cochleae. Taken from [96].

The characteristic frequency for this position of the basilar membrane, i.e. the frequency which shows the greatest sensitivity for a given stimulus amplitude, is slightly shifting with the magnitude of the stimulus. The sensitivity difference between low- and high level stimuli at the characteristic frequency, often referred to as the gain of the cochlear amplifier, can be as much as 3 orders of magnitude. The compressive nonlinearity of the cochlear amplifier is shown in fig. 1.4 B. For about four orders of magnitude, the sensitivity shows a nonlinear decay as a function of the stimulus amplitude, well characterized by a power-law with an exponent $-2/3$.

The intrinsic nonlinear character of the cochlea's response also leads to interferences of two pure tones of different frequency. This leads to the appearance of new frequencies in the response of the cochlea, called combination tones. It also leads to a phenomenon called two-tone suppression: the response of the cochlea to a stimulus containing two pure tones reveals systematically lower amplitudes

at the stimulus frequencies than the response to each of the tones would be in the absence of the second tone [95, 56].

All cited properties have been recognized as signatures of a dynamical system operating near an oscillatory instability, the Hopf bifurcation [13, 14]. In the following, some of the generic aspects of amplification by such a system are discussed.

1.3 Amplification by critical oscillators

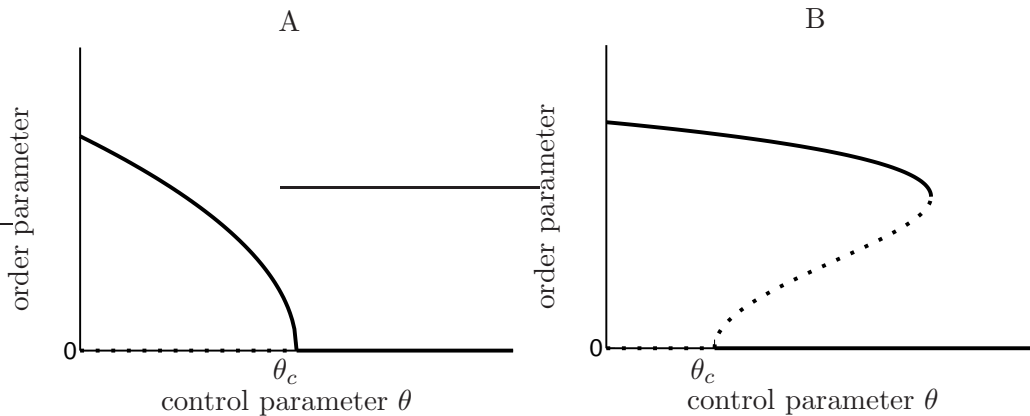


Figure 1.5: Schematic representation of the Hopf bifurcation. Stable solutions of the generic equation 1.1 for the order parameter are indicated by solid lines. For a dynamical system like the hair-bundle, the order parameter would be the dominant Fourier-mode of the bundle-displacement. A, Supercritical bifurcation. For values of the control-parameter $\theta < \theta_c$, the system oscillates spontaneously. B, subcritical bifurcation. The dotted line is an unstable branch. Spontaneous oscillations of non-vanishing amplitude occur for $\theta < \theta_c$, in every case. The hysteresis of the bifurcation is indicated. For $\theta < \theta_c$, two stable solutions, one quiescent and one oscillating, exist.

Consider a dynamical system, governed by a control parameter θ . If such a system is quiescent, i.e. only has stable solutions for a certain range of values of $\theta > \theta_c$, but displays spontaneous oscillations for a range of values $\theta < \theta_c$, we say that the system undergoes a supercritical Hopf bifurcation at the critical point θ_c (if the amplitude of the oscillations vanishes at this point; otherwise, we have a subcritical Hopf bifurcation displaying a hysteresis cycle). This bifurcation is characterized by the fact that two complex conjugated eigenvalues of the dynamical system change the sign of their real parts, whereas all other eigenvalues have negative real parts [104]. At the critical point, such a system shows generic response and amplification properties, independent of the physical mechanisms producing such a bifurcation. Close to this bifurcation, the dynamics of the system can be described by the

normal form [63]:

$$\frac{d}{dt}Z = -(r + i\omega_0)Z - (u + iu_i)|Z|^2Z + O(|Z|^5) \quad , \quad (1.1)$$

where Z is a complex variable and the parameters r, ω_0, u, u_i are real. Note that the parameters in general depend on the control parameter θ , see chapter 4 for details. Exactly at the Hopf bifurcation, $r = 0$. The system allows the trivial solution $Z(t) = 0$, which becomes unstable for $r < 0$. Another solution $Z(t) = \sqrt{-r/ue^{-i\omega_s t}}$ is possible, with $\omega_s = \omega_0 - ru_i/u$; this solution exists for $r < 0$ if $u > 0$, and for $r > 0$ if $u < 0$. This allows us to distinguish supercritical and subcritical bifurcations. The first case $u > 0$ describes the supercritical bifurcation. The oscillating solution exists and is stable on the oscillating side of the bifurcation $r < 0$. This solution is called the limit cycle solution. The second case $u < 0$ describes the subcritical bifurcation. The oscillating solution exists for $r > 0$ and is unstable. In this case, higher-order non-linearities in Z can stabilize another oscillating solution, as shown in fig. 1.5.

We are especially interested in the response $X(t)$ of a physical system to a sinusoidal stimulus force $F(t) = \widehat{F}e^{i\omega t} + \widehat{F}^*e^{-i\omega t}$, where the star denotes complex conjugation. In the absence of spontaneous oscillations, all Eigenvalues have negative real part, and $X(t)$ can be expressed by a Fourier Series of the form $X(t) = \sum X_n e^{in\omega t}$. The dominant Fourier mode $X_1 = \widehat{X}$ obeys the following generic equation [13]:

$$\widehat{F} = \widehat{X}A + B|\widehat{X}|^2\widehat{X} + O(|\widehat{X}|^5) \quad . \quad (1.2)$$

The coefficients $A(\omega, \theta)$ and $B(\omega, \theta)$ are complex values depending on the order parameter as well as on the stimulus frequency ω . At the Hopf bifurcation, the linear term A vanishes: $A(\omega_c, \theta_c) = 0$, and the response of the system can be written:

$$|\widehat{X}| = |B|^{-1/3}|\widehat{F}|^{1/3} \quad . \quad (1.3)$$

Therefore, the sensitivity, defined as $|\widehat{X}|/|\widehat{F}|$, is proportional to $\widehat{F}^{-2/3}$ at the bifurcation point. This nonlinear regime only exists for very small stimuli, if the system is exactly at the bifurcation point $\theta = \theta_c$ and $\omega = \omega_c$. Frequency-mismatch $\omega \neq \omega_c$, or parameter mismatch $\theta \neq \theta_c$ leads to a linear regime for small stimuli. A system which is close to the Hopf bifurcation will therefore display three different regimes in response to stimuli of varying amplitude. For small enough stimuli, we expect the linear regime to be dominant, $|\widehat{X}| \propto |\widehat{F}|$. For larger stimuli, the cubic term becomes dominant, and we expect the compressive nonlinearity $|\widehat{X}|/|\widehat{F}| \propto \widehat{F}^{-2/3}$.

The hearing organs of vertebrates display many of the essential nonlinear properties of a system close to a Hopf bifurcation (see section 1.2), which has therefore been proposed to be the basis of the remarkable performances of the inner ear [13, 27, 70, 26]. The sensory cell of the inner ear, the hair cell, is likely to play a crucial role in this process [48, 13, 93, 85].

1.4 Biophysics of hair cells

Despite the widely varying size and geometry of hair cells, some general features can be observed. All hair cells are embedded in an epithelial layer separating two distinct kinds of fluids. Most of the hair-bundles are connected to an overlying structure, and hair-bundle deflection leads to the generation of electrical signals[46].

Hair cell physiology In all the sensory organs of the inner ear, the hair cell's body is sunk into the epithelium, and only the hair-bundle protrudes on one side, which is called the apical side, the opposite side being called basal (fig. 1.6 and fig. 2.1). Size and geometry of hair cells vary greatly, many specialized types have developed. Inside a hearing organ, hair-bundles of hair cells of the same type generally show a systematic variation of morphology, which is correlated with their position in the organ [106]. The hair cell's apical surface forms tight junctions with surrounding supporting cells of the epithelium, thereby effectively separating the apical side from the basal one. The apical side is in contact with endolymph, which has a composition close to intracellular fluid. It is characterized by a high concentration of potassium and a low concentration of calcium and sodium as compared to perilymph. The basal side is in contact with perilymph, which is a typical extracellular fluid, with a high concentration of sodium and calcium and a low concentration of potassium. On the basal side, the body of the hair cells are innervated by both efferent and afferent nerve fibers [20, 54].

The membrane overlying the epithelium typically creates a shear force acting on the hair-bundles upon appropriate stimulation. If the tips of the bundles are not connected to an overlying membrane, as for example are the bundles of the inner hair cells in the mammalian cochlea [20], they are presumably deflected by hydrodynamic coupling to the endolymph. In vivo, the plasma membrane of hair cells is held at a negative potential with respect to the surrounding environment [20]. Deflection of the hair-bundle opens ion-channels, which allows the influx of K^+ and Ca^{2+} inside the hair cell. The influx of ions depolarizes the cell's membrane potential, which controls the release of neurotransmitters at the basal end of the cell, where the synapses of the innervating neurons are found [20]. Therefore, a mechanical stimulus influences the firing rate of the axons leading to the central nervous system.

Hair-bundle anatomy The hair-bundle itself consists of 10 to 300 hair-like, stiff protrusions from the apical surface, called stereocilia. The cell's plasma membrane encloses them like fingers in a glove. In addition to the stereocilia, many hair-bundles possess one additional hair-like protrusion, the kinocilium (see fig. 1.6) [46, 92].

The dominant structural feature of the stereocilium is its rigid, microfilamentous cytoskeleton. The diameter of stereocilia ranges from 100 to 800 nm, their

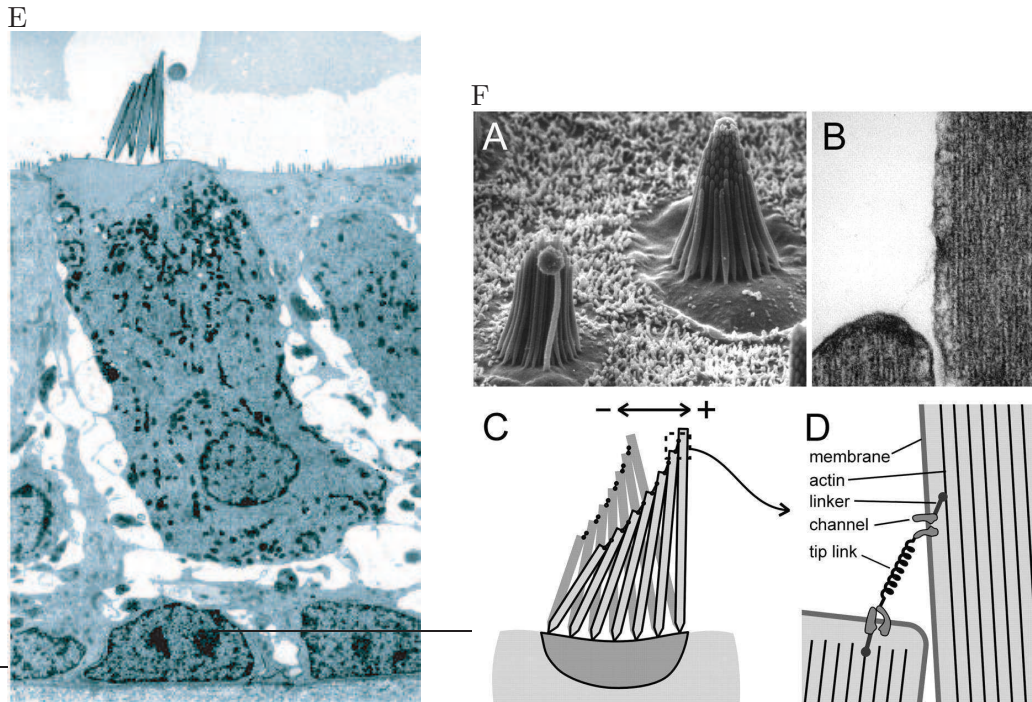


Figure 1.6: The hair cell of the bullfrog's sacculus. E, cut through the hair cell of the bullfrog's sacculus. The hair-bundle with kinocilium and the kinociliary bulb connected to the otolithic membrane can be seen in the top half. Taken from <http://www.rockefeller.edu/labheads/hudspeth>. F, electron micrographs and schematic view of the bullfrog's sacculus. Taken from [40].

height from 1 to 15 μm . They contain between 50 and 3000 actin filaments, depending on their diameter. Although they are isodiametric along most of their length, they taper over a distance of about 1 μm before their insertion into the apex of the cell. In this region, most of the filaments terminate on the cell's plasma membrane. Only a few dozens central filaments extend into the apex of the cell, forming tiny rootlets anchoring the stereocilia to the cell. The rootlets of the stereocilia are anchored into a structure which is called the cuticular plate. It is a dense structure which provides a stable platform upon which the stereocilia are able to tilt. The actin filaments are extensively cross-linked inside the stereocilia, which gives them an exceptional rigidity. They do essentially behave like stiff rods pivoting around their insertion point in the cuticular plate. The bending stiffness of the stereociliary rootlet confers an angular stiffness to the stereocilium [45].

In contrast to the stereocilia, the kinocilium is a true cilium, which means that it contains a structure called the axoneme at its core. The axoneme is composed entirely of microtubules and accessory proteins. In the axoneme, the microtubules form a structure composed of nine doublet microtubules in a circle, surrounding a pair of two single microtubules. The most important accessory protein is ciliary

dynein, whose heads interact with adjacent microtubules to create a sliding force. The kinocilium, which is typically one of the largest cilia in the bundle, is attached to the nearest stereocilia by a set of filaments, and is itself connected directly or by filaments to the overlying membrane.

The stereocilia are generally arranged in a hexagonal pattern with approximately constant center-to-center spacing, while the shape of the hair-bundle's cross-section can have different forms. This shape is typically round in the case of hair-bundles of the vestibular system (fig. 1.6). The kinocilium is placed at one end of the hair-bundle. It is approximately mirror-symmetric with respect to a plane which runs through the kinocilium. The intersection of this plane with the apical surface of the bundle is called the line of bilateral symmetry. Typically, the stereocilia are arranged in rows of constant height which are perpendicular to the line of bilateral symmetry. The highest stereocilia are found close to the kinocilium, and the height decreases monotonically in the opposite direction (fig. 2.1). The decrements in height from row to row are approximately equal [46].

Numerous lateral links connect the stereocilia with their direct neighbors. In general, three kind of links are present. The most interesting kind of link between stereocilia are the tip-links. These filaments connect the tip of one stereocilium with its longest neighbor. This thin filament is thought to play a major role in signal transduction, see 1.5. They are about 5 nm in diameter and about 150 nm in length[60]. It has recently been proposed that Cadherin 23 is an essential component of the tip-link [102, 101]. Closer to the the apical surface, additional links between adjacent stereocilia can be found [46].

The non-stimulated hair cell exhibits a constant current of inflowing ions, called receptor current, indicating that some of the channels are open even in the resting state of the hair-bundle. It exhibits a strong directional sensitivity. Stimuli in the direction of the kinocilium, the excitatory direction, increases the current, thereby depolarizing the membrane potential. Stimuli in the opposite direction reduce the current, hyperpolarizing the membrane. Stimuli perpendicular to the excitatory axis have little or no effect on the receptor current (see for example [47, 43]).

1.5 The Gating-Spring model

The gating spring model reflects the results of a large body of evidence obtained by experiments conducted on the hair-bundle ([15, 44, 3]; reviewed in [49, 52]; see fig. 1.7).

In the formulation of this model, each of the stereocilia bear 1-2 transduction channels[42, 46], which are situated at the distal end of the stereocilia, [67], where the tip-links are found in fig. 1.7. The channel's molecular gate is attached to an elastic element, the gating-spring. This element connects the channel complex of one stereocilium with the top of its shorter, adjacent neighbor. Tension of the gating spring increases the open probability of the ion channel. The tip-link, or

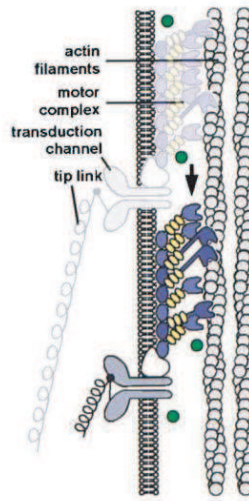


Figure 1.7: Gating-spring model of transduction. Ion-channels are connected to an insertional plaque carrying approximately 50 myosin motors, which are interacting with the actin filaments at the core of the stereocilium. The molecular gate of the channel is attached to the gating-spring, which connects a stereocilium's channel to the tip of the adjacent, smaller stereocilium. Part of the gating-spring distance as inferred from experiments [82] might stem from a conformational change of the Ion-channels, indicated by the change of the lever arm. The motor complex is thought to slide down the stereocilium if the tension in the gating-spring is too high. Taken from [41]

any compliant element in series with it, is thought to be an essential element of the gating-spring [45].

When a channel opens, the gating-spring relaxes, which corresponds to a reduction of its length by a certain distance, called the gating-swing. The gating-swing is the effective shortening of the gating-spring upon opening [44]. This phenomenon can have several origins: A conformational change of the channel between open and closed state can account for part of the gating-swing. If the spring is attached via a kind of lever to the channel, the observed swing might be larger than can be expected from a simple conformational change. Provided that part of the gating-spring stiffness is determined by elements at the intracellular side of the ion-channel, it is also possible that the inflowing Ca^{2+} -Ions change the properties of these elements (stiffness, length at rest or attachment point)².

The relaxation of the gating-spring upon opening of the channels gives rise to the phenomenon called gating-compliance: the stiffness of the bundle depends upon the magnitude of the deflection [44]. For small deflections, this stiffness has been shown to be smaller than for larger displacements. In recent experiments,

²Because the channel complex is connected to an ensemble of myosin motors (see below), the internal calcium concentration might influence the stiffness of their tails or the state of their heads [82, 41].

this stiffness has been found to be negative in a narrow range around the greatest slope of the open probability curve. Inside this region of negative stiffness, the position of the hair-bundle is unstable. A stationary force is not sufficient to fix the bundle's position in this region; a feedback mechanism has to be applied [82].

The channel complex is connected to approximately 50 myosin motors, which are concentrated on an insertional plaque [52]. The myosin motors are constantly pulling on the gating-spring, creating a tension in the gating-spring. The force which is necessary to stall the molecular motors therefore determines the tension of the gating-spring. The stronger the molecular motors, the higher the tension in the gating-spring, and therefore the higher the open probability.

The activity of the myosin motors gives rise to the phenomenon called adaptation: after deflection of the bundle in the excitatory direction, the stereocilia pivot around their insertion points in the cuticular plate, leading to a shearing movement between adjacent stereocilia (fig. 1.8). The increased tension in the gating spring induces the channels to open, and the motors to slide down the stereocilium, restoring the tension of the gating spring to a value close to the one which has been observed before the deflection. Because the bundle restores thereby its sensitivity for a new deflection in the excitatory direction, this process is called adaptation [3].

It has been observed, that the open probability of the channels is different before a prolonged stimulus, as it is at the end of the stimulus [99]. In the case of stimuli in the excitatory direction, the open probability after the deflection is larger than in the resting bundle. This shows that adaptation is incomplete: the bundle restores its sensitivity, but not to its full extent. To explain this observation, another elastic element is thought to connect the insertional plaque to the actin filaments of the same stereocilium: the extent spring [99]. Upon deflection in the excitatory direction, the molecular motors are unable to relax the tension of the gating-springs completely, because both the force of the molecular motors and the higher tension of the extent spring have to be counterbalanced by the tension of the gating-spring.

In order to summarize the gating-spring model, fig. 1.8 shows the effect of a 60 nm step displacement applied to the tip of a hair-bundle for 0.2 seconds. Part A of this figure corresponds to the external stimulus applied to the top of the bundle, part B and D are theoretical curves calculated with the help of a description of the hair-bundle based on the gating-spring model, and part C represents the different states of the bundle according to the gating-spring model. These curves are in accordance with experimental observations [37, 3, 99].

In this example, the channels' open probability at its resting position is approximately 15% (i), corresponding to values which have been measured in experiments with a high external calcium concentration [15].

The positive stimulus first opens the ion-channels, increasing the transduction current of ions entering through the channels. The peak value of the current

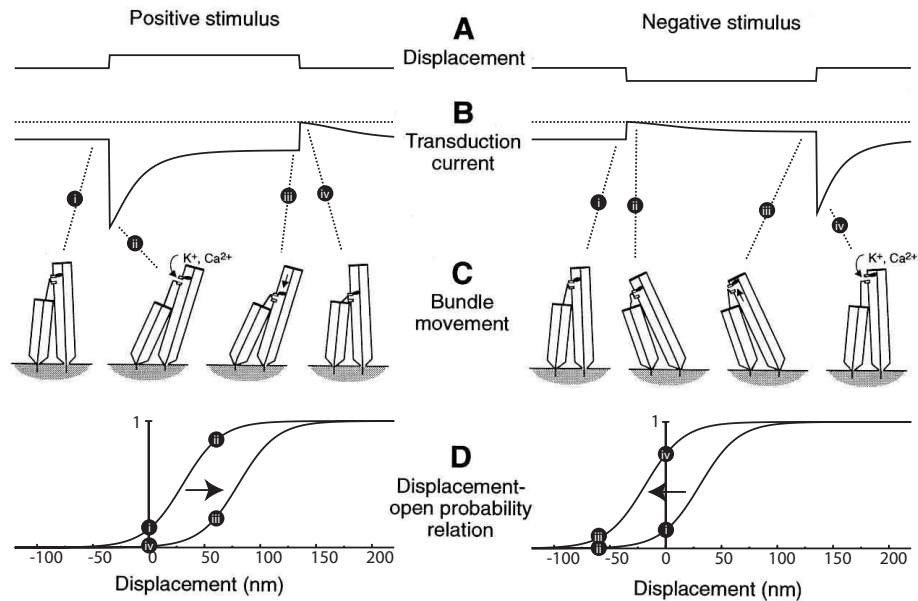


Figure 1.8: The gating-spring model of transduction: Adaptation and displacement-response curve. A, the diagram depicts a hair-bundle under the influence of a 60 nm, 200 ms stimulus step. B, evolution of the transducer current during the stimulus. C, sketch of the hair-bundle before (i), immediately after the onset of the stimulus (ii), immediately before the end of the stimulus (iii), and immediately after the end of the stimulus (iv). D, displacement-open probability curves relating the displacement of the tip of the hair-bundle and the open probability reached immediately after the onset of the step, before adaptation has set in. Curves are calculated for the model of the hair-bundle presented in chapter 2, with parameter values given in column A of table B.1 in appendix B. Modified from [52].

at (ii) is proportional to the open probability of the channels immediately after deflection, before adaptation has set in. Using stimuli of varying amplitude, one can therefore measure these curves sketched in fig. 1.8 D, relating the amplitude of the step to the open probability. These curves have a sigmoidal shape, which is explained in chapter 2. Due to the incomplete adaptation, this displacement-open probability curve is not shifted by the 60 nm given by the step amplitude, but by only 48 nm (see section 2.4.3 for details).

After the application of a positive stimulus (see fig. 1.8, left column), the molecular motors begin to slide down the stereocilia, decreasing the tension in the gating-spring and closing the channels, resulting in an open probability slightly larger than the original one (iii). This phase of slow adaptation can be described by a single exponential with a time constant of the order of tens of milliseconds [43]. The end of the stimulus reduces the tension of the gating-springs so that the channels close (iv), before the motors begin to adapt to the new situation to restore the original open probability and tension.

1.6. SPONTANEOUS OSCILLATIONS OF HAIR-BUNDLES OF THE SACculus OF THE BULLFROG

A negative stimulus (see fig. 1.8, right column) first closes the channels, before the adaptation of the motors sets in to restore an open probability (iii) slightly below the original open probability (i). The end of the stimulus opens the channels, before the motors restore the original open probability.

1.6 Spontaneous oscillations of hair-bundles of the sacculus of the bullfrog

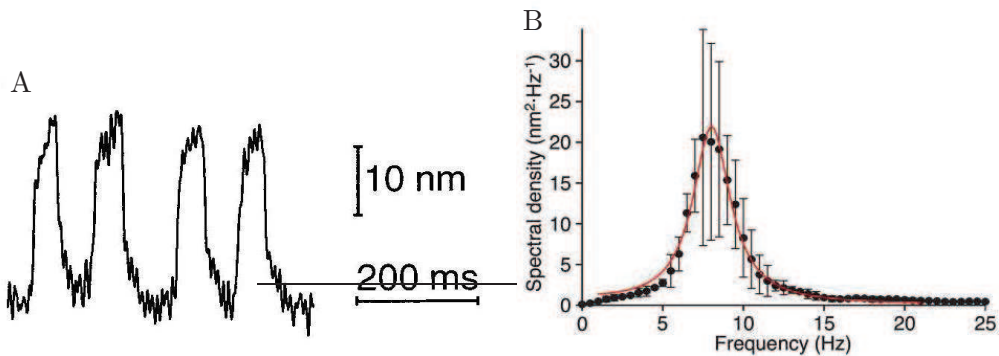


Figure 1.9: Spontaneous oscillations observed *in vitro* using the two-compartment technique. A, noisy oscillations of an individual hair cell. B, spectral density of noisy oscillations. This particular hair-bundle displayed spontaneous oscillations of a characteristic frequency around 8 Hz. Taken from [81].

The first *in vitro* experiments using the hair cells from the bullfrog's sacculus, a vestibular organ which is involved in the detection of ground-borne seismic waves and of the detection of low-frequency sound waves [62, 110], were done using a standard saline solution to bathe the hair cells. In these experiments, spontaneous oscillations were seldom observed, although the adaptation motors in this environment were active and restored the tension in the gating-springs (see for example [43]).

This situation is changed when the *in vivo* environment is approximately restored, including a different solution for the apical and the basal aspects of the hair cell. Using this two-compartment technique, a large portion of the experimentally observed bundles displayed spontaneous oscillations [78].

The fluctuation-dissipation theorem asserts that the autocorrelation function and the linear response function of a system at thermal equilibrium are related. By measuring both the linear response function of the hair-bundle and its autocorrelation function, it has been shown that the movements which can be seen in fig. 1.9 are not due to thermal fluctuations [81]. Activity must therefore be present in this hair-bundle.

These active oscillations are noisy and they clearly show a bimodal distribution

of bundle positions: the bundle spends most of its time in the extreme positions. Using the two-compartment preparation, hair-bundles of the bullfrog's sacculus have been reported to oscillate at frequencies varying from ~ 5 to ~ 40 Hz [79]. This particular bundle had a characteristic frequency of around 8 Hz, as can be seen from the power-spectrum in fig. 1.9.

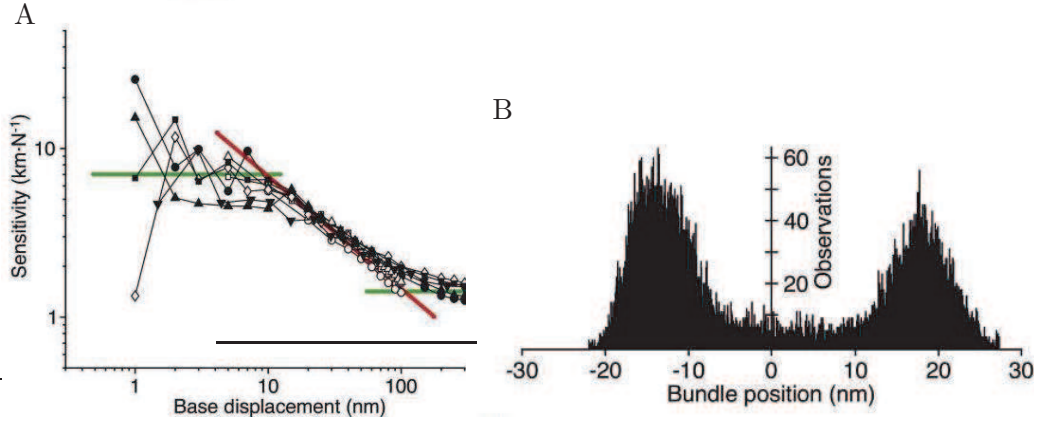


Figure 1.10: A, Compressive nonlinearity of a hair-bundle stimulated close to its characteristic frequency. The red line corresponds to a slope of $-2/3$, which is the slope expected from a system close to a Hopf bifurcation. Plotted is the sensitivity x_1/f_1 of the hair-bundle for sinusoidal stimulations of the tip of the hair-bundle via a flexible fiber attached to the tip of the hair-bundle, as a function of the base-displacement amplitude of the fiber. 1 nm of base-displacement corresponds to a force-amplitude of 0.25 pN. Taken from [80]. B, distribution of the hair-bundle's position during spontaneous motion. This motion shows a clear bimodal distribution. Taken from [81].

This bundle displays all of the four essential characteristics of the cochlear amplifier. It amplifies weak stimuli in a frequency-dependent manner, being most sensitive close to its characteristic frequency of oscillations. It shows compressive nonlinearity for varying stimulus-amplitudes. It even reproduces the characteristic slope $|\hat{X}|/|\hat{F}| \propto \hat{F}^{-2/3}$ for approximately one order of magnitude, see fig. 1.10. It also displays the analog of oto-acoustic emissions, the spontaneous oscillations.

Chapter 2

Physical description of hair-bundles

In this chapter, we are going to present a physical description of the dynamics of the hair-bundle. First, we will describe the geometry of the hair-bundle in greater detail, especially focusing on the geometry of those found in the bullfrog's sacculus, on which many experiments have been performed. We will then discuss the dynamical variables used in the rest of this work. The role of the gating-springs and the Ion-channels is explained, and a model for the dynamics of the adaptation-motors is introduced. In particular, a simple description of the role of the calcium-concentration as a regulator of motor activity is presented.

2.1 Geometry and displacement variables

A hair-bundle of the bullfrog's sacculus consists of ~ 50 -70 stereocilia and one kinocilium [54], see fig. 2.1. Before describing the interactions between individual stereocilia, we will first introduce the important quantities of a single stereocilium. As explained in the introduction, stereocilia behave essentially like stiff rods, due to the cross-linked actin-filaments at their core. In the following, stereocilia are only regarded as stiff cylinders, whose only degrees of freedom consist in a pivoting movement around their insertion point in the cuticular plate.

One stereocilium is characterized by its height, h , and its radius, r , see fig. 2.2. The typical height of the stereocilia inside a bundle ranges from ~ 3 -8 μm , their diameter is about 450 nm [54]. At the insertion point in the cuticular plate, the stereocilia taper to a diameter of about 100 nm, and the number of actin-filaments decreases from about 600 in the bulk of the stereocilia to about 30 at its insertion point. The smaller number of actin filaments in the rootlet makes them more flexible than the bulk of the stereocilia, allowing the stereocilium to pivot around its base, and leading to an angular stiffness.

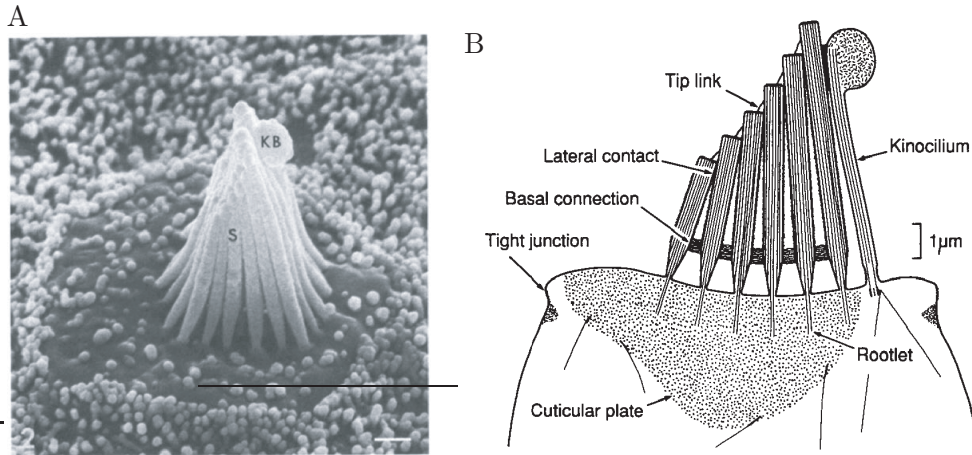


Figure 2.1: The hair-bundle of the sacculus of the bullfrog. A, scanning electron micrograph of a hair cell in a bullfrog's saccular epithelium from which the otolithic membrane has been dissected. S, stereocilium; KB, kinociliary bulb; calibration bar, 1μ m. Taken from [46]. B, schematic drawing of the constituents of a representative hair-bundle. Each stereocilium is filled with cross-linked actin-filaments, a few of which extend as rootlets into the cuticular plate. Three types of filaments connect the stereocilia, the basal connections, lateral links (denoted as Lateral contact), and the tip-links. Taken from [92]

The position of one stereocilium is therefore characterized by the angle Φ which it forms with the apical epithelial surface. Due to the polarity of the hair-bundle, the excitatory direction is the one of interest for us, and Φ defines the inclination of the stereocilia with respect to this direction. Alternatively, we can characterize the angle of inclination by the projection of the tip of the hair-bundle on the apical epithelial surface¹, X . Furthermore, due to the hollow shape of the cuticular plate, a single stereocilium is also characterized by its elevation Q above the ground level of the cuticular plate.

As explained in section 1.5, the tip-links are supposed to be connected to Ion-channels, most probably situated at both ends of the gating-springs [22]. They are thought to be an essential component of the gating-springs. The tension of the gating-spring influences the open probability of the Ion-channels it is connected to: the higher the tension, the higher the probability of a given channel to be in an open state. To first order, we describe the elasticity of a gating-spring as a hookean spring of stiffness k_{GS} . Due to the elastic nature of the tip-link, the gating springs can only bear forces in the form of stress. If both ends of

¹In the equations derived below, we will use a certain convention concerning the use of capital and small letters. Two different reference frames are of importance in the hair-bundle. The direction parallel to the apical epithelial surface is the reference frame in which motion of the bundles is observed, and experimental data is acquired. Quantities measured with respect to this reference frame are denoted with capital letters. A different reference frame is the one parallel to the axis of the stereocilia. Motor-displacements take place relative to that reference frame. Quantities described in the stereocilium-reference frame are denoted with small letters.

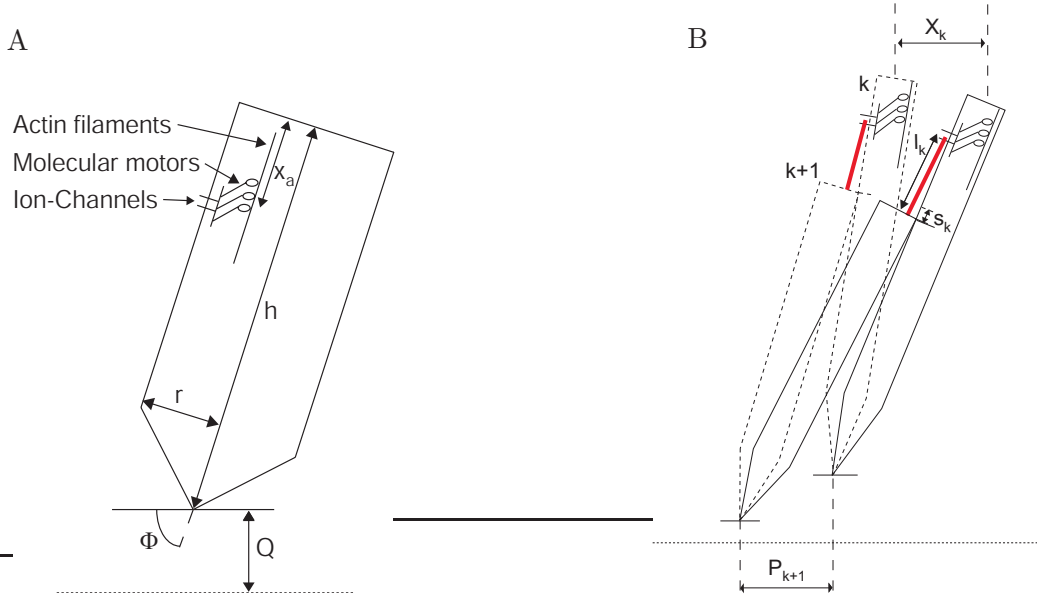


Figure 2.2: Idealized geometry of stereocilia, not to scale. A, the important components of a single stereocilium. These are its height, h , its radius, r , its elevation above the ground level of the cuticular plate, Q , its inclination angle with respect to the apical epithelial surface, Φ , and the position of the molecular motors on the actin-filaments, x_a . B, schematic drawing of two adjacent stereocilia, not to scale. The tip-link is indicated (thick red line), and its extension, l ; the distance from one stereocilium to its larger neighbor, P ; the projection of the tip of a stereocilium on the apical epithelial surface, X ; the shear s when the stereocilium moves from the dashed-line position to the solid-line position.

the tip-link are brought into closely adjacent positions, the tip-link slackens, see [60]. However, several independent measurements indicate that this “slackened” regime only occurs for very large displacements of the bundle’s tip in the inhibitory direction [49]. but they do not transmit compressive forces. Instead, if the bundle’s tip is deflected for less than 100 nm in this direction, the gating-spring seems to be under tension. Spontaneous oscillations displayed by hair-bundles do not have that large amplitudes, and none of the phenomena discussed in the rest of this work rely on displacements exceeding 100 nm. Therefore, we have not included this behavior in the model discussed in the following.

The position of the motor-channel complex with respect to the actin-filaments, introduced in section 1.5, is denoted with x_a . The extension of the tip-links due to the position of the motors and the position of the stereocilia is denoted with l .

Due to the numerous lateral links connecting individual stereocilia, the hair-bundle behaves as a unit [46]: deflection of the kinocilium or of a stereocilium leads to a rocking movement of the whole bundle. This phenomenon might be reinforced by the curvature of the cuticular plate, which is concave in the direction of bilateral symmetry (see fig. 1.6): it forces stereocilia together along this axis [46]. The

various lateral links and the angular stiffness of the rootlets (stereociliary pivots) lead to a combined stiffness of the hair-bundle, the stereociliary pivot stiffness, which we will describe as a hookean spring of stiffness K_{SP} .

The observation that the bundle behaves essentially as a unit also leads to the consequence that the gating-springs must be treated as parallel springs: a force applied to the tip of the hair-bundle is instantaneously applied to all of the gating-springs.

It is useful to number the ranks of stereocilia, every rank corresponding to the stereocilia of equal height perpendicular to the line of bilateral symmetry, see section 1.4. The largest stereocilium is labeled 1, its direct smaller neighbor is number 2 and so forth, see fig. 2.2. A typical bundle contains 16 ranks of stereocilia, every rank being shorter than the preceding one by approximately 325 nm [54].

Upon stimulation, the stereocilia are forced to slide on the back of their direct neighbors, leading to a shear which changes the extension of the tip-links. For a given pair of stereocilia in adjacent ranks, for example k and $k + 1$ in fig. 2.2, the shear s of a stereocilium in rank k is defined as the distance which the top of its smaller neighbor, $k + 1$, slides down on the side of stereocilium n upon deflection of the hair-bundle. Given the geometry described above and depicted in fig. 2.2, we can calculate the angle of a smaller stereocilium Φ_{k+1} if we know the angle of its larger neighbor, Φ_k [54]:

$$\Phi_{k+1} = \Phi_k - \frac{\pi}{2} + \arctan \frac{r_{k+1}}{h_{k+1}} + \arccos \frac{P_{k+1} \sin \Phi_k + (Q_{k+1} - Q_k) \cos \Phi_k - r_{k+1}}{\sqrt{h_{k+1}^2 + r_{k+1}^2}} \quad , \quad (2.1)$$

where P_{k+1} is the distance between the shorter stereocilia $k + 1$ and its larger neighbor. Given a set of $\{P_k, h_k, r_k, Q_k\}$, we can then calculate all the angles Φ_k as a function of $\Phi \equiv \Phi_1$, the angle of the rightmost, largest stereocilium. We can therefore describe the shear s_k as a function of the angle Φ . Because we can measure X experimentally, we are interested in the evolution of the s_k as a function of X . We can expand the s_k as a function of the difference $\delta X = X - X_r$, the displacement of the bundle's tip from its resting position X_r :

$$s_k = \gamma_k \delta X + O(|\delta X|^2) \quad . \quad (2.2)$$

When the bundle is at the position X_r , $s_k = 0$ by definition. In the following, we will only keep the first order term, ignoring nonlinearities in this relation². The factor γ_k is called a projection-factor, relating the experimentally observable motion to a change of extension of the tip-link.

²Here and in the following, we will mostly keep only the linear terms in the expansions. This may be justified by the fact that physiological responses of the bundle saturate at displacements of $\sim \pm 100$ nm [44]. Spontaneous oscillations do not exceed these values. Measurements of the stiffness of the hair-bundle show a linear behavior for displacements of up to $\sim \pm 100$ nm [82].

To linear order and for small angle approximation³, we can find a simple expression for the projection-factors:

$$\gamma_k = \frac{P_{k+1}}{h} \quad , \quad (2.3)$$

with h the height of the longest stereocilium.

For an experimentally determined set of parameters describing the hair-bundle, the γ_k have been calculated and it has been found that their values are sufficiently close over the range of physiological displacements to describe them by a single projection factor [54]:

$$\gamma_k = \gamma \quad . \quad (2.4)$$

In the following, we will derive general expressions for the open probability of the ion-channels as a function of the position X and the motor-positions x_a for a given stereocilium. In later chapters, we will simplify the equations using the approximation $\gamma = \gamma_k$. For a given position X , all the s_k are equal, and the gating-springs function then operate as parallel springs.

2.2 Ion-channel gating

In order to understand quantitatively how the hair-bundle works as a signal transducer, it is important to know the dependence of the open probability of the Ion-channels in dependence of the different dynamic variables which characterize the hair-bundle. The idea which will be presented here can be found for example in [15, 44, 49, 76].

If the position of the hair-bundle is fixed, the open probability of a given channel can be calculated using equilibrium statistical mechanics.

If, however, the hair-bundle displays spontaneous oscillations or is deflected by a stimulus probe, this approach can only be justified if the relevant timescales of the bundle movement are much slower than the transition rates of the channel from open to closed state, characterized by the channels' dwell times in either state. Recent single channel measurements indicate that the channels' characteristic timescale is of the order of one millisecond [88], whereas adaptation timescales of the hair-bundle are of the order of tens of milliseconds [43], and spontaneous oscillations of the hair-bundle of the bullfrog's sacculus are of the order of tens of Hz [78]. It seems therefore reasonable to apply equilibrium statistical mechanics also to moving hair-bundles of the bullfrog's sacculus.

In the simplest case, a mechanosensitive channel can have two states, open or closed. Both states of the channel are energetically different, the open state being separated from the closed one by an intrinsic free-energy difference $E_o - E_c =$

³and some additional approximations: $|Q_{k+1} - Q_k| \ll h_k, P_k^2 \ll h_k^2, r_k^2 \ll h_k^2, |r_k \Phi_k| \ll P_k$, which are all reasonably small for the hair-bundle

$\Delta G > 0$. In the following, we will calculate the open probability of a given channel in dependence of the position X of the hair-bundle's tip in the framework of this two-state model of gating in hair cells [76]. We will furthermore assume that there is only one gating-spring associated to each of the N stereocilia of a hair-bundle.

The energy of the hair-bundle is then:

$$E(X, \{x_{a,n}\}, \{\sigma_n\}) = \sum_{n=1}^N E_n(X, x_{a,n}, \sigma_n) + \frac{1}{2} K_{SP} (X - X_{SP})^2 \quad , \quad (2.5)$$

where X_{SP} is the rest-length of the spring associated with the stereociliary pivot elements, i. e. the position to which the bundle would relax if the gating-springs were absent. E_n is the mechanical energy of the n -th channel-gating-spring complex⁴. This energy depends on the state of the channel ($\sigma_n = 1$ for a channel in open state, $\sigma_n = 0$ for a channel in closed state), and on the energy stored in the elastic elements connected with the channel complex, the gating-spring and the extent spring, characterized by the stiffness k_E . The energy of the gating-spring is given by its stiffness k_{GS} and its extension l_n , which is influenced both by the shearing movement between adjacent stereocilia, and the displacement of the molecular motors. In linear approximation, the change of the length δl_n under the influence of a displacement of the molecular motors $\delta x_{a,n}$ and a displacement of the bundle's tip δX is therefore:

$$\delta l_n = \gamma_n \delta X - \delta x_{a,n} \quad . \quad (2.6)$$

This equation uses the approximation that the gating-springs are quasi-parallel with respect to the axis of the stereocilia, which has been found experimentally, see for example [60]⁵.

As described in section 1.5, the gating-spring model of hair-bundle transduction stipulates the gating-swing of magnitude d , by which the extension of the gating-spring is shortened upon opening of the channels. Therefore, the energy of the n -th channel-gating-spring complex can be written as:

$$E_n(X, x_{a,n}, \sigma_n) = \frac{1}{2} k_{GS} (\gamma_n X - x_{a,n} - x_{GS,n} - \sigma_n d)^2 + \sigma_n \Delta G + \frac{1}{2} k_E (x_{a,n} - x_{E,n})^2 \quad . \quad (2.7)$$

In this equation, k_E is the stiffness of the extent spring introduced in section 1.5, and $x_{GS,n}$ and $x_{E,n}$ are the rest-lengths of the corresponding springs. The partition function of the hair-bundle reads

$$Z(X, \{x_{a,n}\}) = \sum_{\{\sigma_n\}} e^{-\frac{E(X, \{x_{a,n}\}, \{\sigma_n\})}{k_B T}} \quad , \quad (2.8)$$

⁴The subscript $n = 1 \dots N$ is now used to address every individual stereocilium n and its channel-gating-spring complex. Therefore, γ_n is to be understood as the γ_k associated with the rank k in which the n -th stereocilium is found.

⁵A more correct equation would be $\delta l_n = (\gamma_n \delta X - \delta x_{a,n}) / \cos \psi$, where ψ is the angle between the axis of the stereocilium's actin filaments and the orientation of the tip-link l_k . If $\psi \ll 1$, eq. 2.6 is a reasonable approximation.

which can be rewritten as

$$Z(X, \{x_{a,n}\}) = e^{-\frac{K_{SP}(X-X_{SP})^2}{2k_B T}} \prod_n z_n \quad (2.9)$$

under the assumption that all channel-gating-spring complexes are independent of each other, with the individual partition function

$$z_n = e^{-E_n(x_{a,n},1)/k_B T} + e^{-E_n(x_{a,n},0)/k_B T} \quad (2.10)$$

$$= \exp \left[-\frac{k_{GS}(\gamma_n X - x_{a,n} - x_{GS,n})^2 + k_E(x_{a,n} - x_{E,n})^2}{2k_B T} \right] z_n^\sigma, \quad (2.11)$$

where

$$z_n^\sigma = 1 + \exp \left[\frac{k_{GS}d(\gamma_n X - x_{a,n} - x_{GS,n}) - \Delta G - \frac{1}{2}k_{GS}d^2}{k_B T} \right]. \quad (2.12)$$

The open probability $P_{o,n}$ of an individual channel in thermal equilibrium is determined by the Boltzmann relation:

$$\begin{aligned} P_{o,n}(X, x_{a,n}) &= \frac{e^{-E_n(X, x_{a,n}, 1)/k_B T}}{z_n} \\ &= \frac{1}{1 + \exp \left[-\frac{k_{GS}d(\gamma_n X - x_{a,n} - x_{GS,n}) - \Delta G - \frac{1}{2}k_{GS}d^2}{k_B T} \right]} \end{aligned} \quad (2.13)$$

The mean open probability of the hair-bundle is then

$$P_o(X, \{x_{a,n}\}) = \sum_{n=1}^N P_{o,n}(X, x_{a,n}) / N \quad (2.14)$$

As already discussed above, this calculation corresponds to the simplest case, attributing one channel to every gating-spring, which can have one open and one closed state. The result is the sigmoidal shape of the $P_{o,n}$ with respect to X displayed by 2.13. This sigmoidal shape has been found repeatedly in experimental displacement-open probability curves [42, 43, 44].

However, these curves do not always display this symmetric shape [15, 42]. Under the assumption that there are two channels per stereocilium, one at each end of the tip-link, or if there were two closed states and one open state, the shape of the $P_{o,n}$ is changed and loses its symmetry. Nonetheless, the situation does not change fundamentally. In these more complicated cases, the $P_{o,n}$ have still the same qualitative features: The largest slope is situated around $P_o = 0.5$ and this slope increases with d and k_{GS} . For simplicity, we will only use the two-state model of channel gating in our model of the hair-bundle.

The force acting on the position of the tip of the hair-bundle X is given by :

$$F = \sum_n F_n - K_{SP}(X - X_{SP}) \quad (2.15)$$

with

$$F_n = k_B T \frac{\partial \ln z_n}{\partial X} = -\gamma_n k_{GS} (\gamma_n X - x_{a,n} - x_{GS,n} - dP_{o,n}) \quad , \quad (2.16)$$

whereas the force acting on the insertional plaque $x_{a,n}$ is given by

$$f_{\text{mot},n} = k_B T \frac{\partial \ln z_n}{\partial x_{a,n}} = k_{GS} (\gamma_n X - x_{a,n} - x_{GS,n} - dP_{o,n}) - k_E (x_{a,n} - x_{E,n}) \quad . \quad (2.17)$$

Several of the constants appearing in the equations can be eliminated by choosing appropriate origins for the $x_{a,n}$ - and the X - axes. We define the origin of the axes by the position of the hair-bundle and the motors at the point where a hair-bundle with vanishing extent-spring stiffness $k_E = 0$ is at rest, and the motors do not exert forces on the insertional plaque (i. e. this position corresponds to the hypothetical position of the hair-bundle, if the molecular motors are not active). This point corresponds to $F = 0$ and $f_{\text{mot},n} = 0$. As the energy which is necessary to open an individual channel is very high, $\Delta G \sim 10k_B T$ [49], all channels are closed at this point: $P_{o,n} \sim 0$. Therefore, $x_{GS,n} = 0$ and $X_{SP} = 0$. We then express the open probability of an individual channel in these new coordinates as:

$$P_{o,n}(X, x_{a,n}) = \frac{1}{1 + A e^{-\frac{k_{GS}d(X\gamma_n - x_{a,n})}{k_B T}}} \quad (2.18)$$

$$A = e^{\frac{\Delta G + \frac{1}{2}k_{GS}d^2}{k_B T}} \quad . \quad (2.19)$$

2.3 Adaptation motors and calcium-feedback

We have described the passive part of hair-bundle mechanics. We will now introduce specific equations describing the dynamics of the molecular motors. The adaptation motors are able to restore the tension in the tip-links by moving actively on the actin-filaments of the stereocilia in the direction of the tip of the stereocilium, i. e. in the negative direction of the x_a -axis. Here, we assume that the ensemble of motors on one stereocilium can be described by a simple linear force-velocity relation for the N_s motors in one stereocilium under the influence of the external load f_l :

$$f_l = \xi_a \dot{x}_a + f_0 \quad . \quad (2.20)$$

Fig. 2.3 B schematically depicts this relation. The coefficient ξ_a can be seen as the friction coefficient of the motor complex on the actin filament of the stereocilium. In the absence of an external force $f_l = 0$, the motors are moving at constant

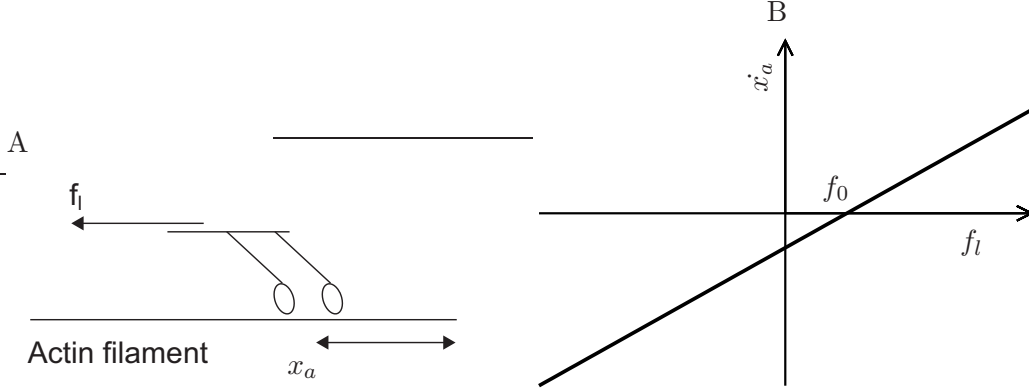


Figure 2.3: Molecular motors and the force-velocity curve. A, schematic view of a motor complex x_a under the influence of an external force f_l and linear force-velocity curve. In the absence of the external force f_l , the motors are running towards the top of the stereocilium, which is found on the right hand side of the figure. Increasing the external force f_l slows down the motors. At $f_l = f_0$, the motors do not move anymore. For forces $f_l > f_0$, the motors are forced to slide down the stereocilium, to the left hand side of the figure. B, linear force-velocity curve. The motors are at stall if $f_e = f_0$, and the motors are running with velocity $-f_0/\xi_a$ in the absence of an external force.

speed $-f_0/\xi_a$, while the slope of the force-velocity relationship is characterized by $\xi_a > 0$. The average force generated by the motors at stall, i.e. when they do not move, is $f_0 = N_s f p$, where f is the average force of an individual motor attached to the filament, N_s is the number of molecular motors in one stereocilium, and p the probability that a given motor is bound to the filament. The external force f_l acting on the motors of one stereocilium has been calculated before (eq. 2.17):

$$f_{\text{mot},n} = \xi_a \dot{x}_{a,n} + N_s f p \quad . \quad (2.21)$$

The external calcium-concentration is known to influence the activity of the motors [37]; reviewed in [28]. The lower the concentration, the faster is the adaptation time constant, thus the motors increase their activity when $[\text{Ca}^{2+}]$ is lowered. This fact can be accounted for in a number of ways. A simple way is to assume that the probability of attachment p depends on the local $[\text{Ca}^{2+}]$ C at the motor site. We expand the attachment probability in terms of C :

$$p(C) = p_0 + p' C + O(p^2) \quad . \quad (2.22)$$

For the rest of this work, we will just consider the linear term of this expansion.

The calcium entering the stereocilium upon the opening of the channels rapidly diffuses inside the stereocilia. The plasma-membrane of the stereocilia also contains Ca^{2+} -pumps, which continuously extrude Ca^{2+} from the endolymphatic fluid of the stereocilium, maintaining $[\text{Ca}^{2+}]$ at a low level. In principle, the mechanisms governing $[\text{Ca}^{2+}]$ at a given point are complicated ([68]). For simplicity, a

single time-constant for the calcium-regulation τ is introduced, and the calcium-dynamics of the n -th stereocilium reads:

$$\tau \dot{C}_n = C_0 - C_n + C_M P_{o,n} \quad . \quad (2.23)$$

Here, C_0 is the $[\text{Ca}^{2+}]$ which the cell is maintaining with the help of the calcium-pumps at closed channels, and $C_M + C_0$ is the maximal $[\text{Ca}^{2+}]$ at the location of the adaptation motors. This value is proportional to $[\text{Ca}^{2+}]$ in the endolymph [78].

2.4 A simple model of the hair-bundle

As described in section 2.1, the values of the different γ_n are reasonably close to one another in the range of physiological displacements of the hair-bundle. We will therefore assume from now on that γ_n is the same for all stereocilia. For simplicity, we also assume $x_{E,n} = x_E$. This choice means that the extent-springs are the same for all stereocilia. This results in the fact that all N equations for the motor-positions are strictly the same, and all the $x_{a,n}$ can be described by the single dynamical variable $X_a = x_{a,n}/\gamma$, the motor displacement in the reference frame parallel to the apical epithelial surface. The mean open probability in this reference frame reads (cf. eq. 2.13 and 2.18):

$$P_o(X, X_a) = \frac{1}{1 + Ae^{-\frac{X-X_a}{\delta}}} \quad , \quad (2.24)$$

with

$$\delta = \frac{k_B T N}{K_{GS} D} \quad (2.25)$$

$$D = d/\gamma \quad (2.26)$$

$$K_{GS} = k_{GS} N \gamma^2 \quad (2.27)$$

In order to facilitate the discussion in the rest of this work, we will introduce some abbreviations which will help in the following. The force of the motors will be described by one parameter corresponding to the maximal total force of all motors, f_{\max} , and the feedback strength, characterized by the first derivative of the attachment probability p' , will be described by the dimensionless feedback-strength S :

$$f_{\max} = N_a f p_0 \quad (2.28)$$

$$S = -C_M \frac{p'}{p_0} \quad (2.29)$$

The equations defining the active dynamics of the hair-bundle read:

$$\lambda \dot{X} = -K_{GS}(X - X_a - DP_o) - K_{SP}X + F_{\text{ext}} \quad (2.30)$$

$$\lambda_a \dot{X}_a = K_{GS}(X - X_a - DP_o) - K_E(X_a - X_E) + \gamma f_{\text{max}} \left(S \frac{C}{C_M} - 1 \right) \quad (2.31)$$

$$\tau \dot{C} = C_0 - C + C_M P_o \quad , \quad (2.32)$$

where $N_a = N_s N$ is the total number of motors and

$$K_E = k_E N \gamma^2 \quad (2.33)$$

$$X_E = x_E / \gamma \quad (2.34)$$

$$\lambda_a = \xi_a N \gamma^2 \quad (2.35)$$

have been used for the projection into the reference frame where the measurements take place. Here, λ is the hydrodynamic friction of the hair-bundle, and inertial terms have been neglected.

2.4.1 Stationary solutions

We can write the stationary solutions of the simplified model eqs. 2.30 - 2.32 in the following form:

$$C - C_0 = \frac{C_M}{1 + A e^{-(R'C+R)/\delta}} \quad (2.36)$$

$$X - X_a = R'C + R \quad (2.37)$$

$$X_a = \frac{-\gamma N_a f p(C) + F_{\text{ext}} + K_E X_E - K_{SP}(X - X_a)}{K_{SP} + K_E} \quad , \quad (2.38)$$

with the abbreviations

$$R' = \frac{K_{SP}}{K_P} N_a f \gamma p' + \left(1 - \frac{K_E K_{SP}}{K_P} \right) \frac{D}{C_M} \quad (2.39)$$

$$R = \frac{K_E K_{SP}}{K_P} \left(-X_E + \frac{F_{\text{ext}}}{K_{SP}} + \frac{DC_0}{C_M} \right) + F_{\text{max}} \frac{K_{SP}}{K_P} - \frac{DC_0}{C_M} \quad (2.40)$$

$$K_P = K_{SP} K_{GS} + K_{SP} K_E + K_E K_{GS} \quad . \quad (2.41)$$

The abbreviation for the permutations of the stiffnesses, K_P , will be used frequently in the subsequent parts of this work.

A graphical solution to equation 2.36 is depicted in fig. 2.4.

The system has either one or three stationary solutions, in marginal cases it can have two solutions. Later on, we will see that the existence of three fixed points normally coincides with bistability, the extreme solutions being stable and the intermediate one being an unstable fixed point. Two general cases can be distinguished dependent on the sign of R' : First, $R' < 0$ only allows for the

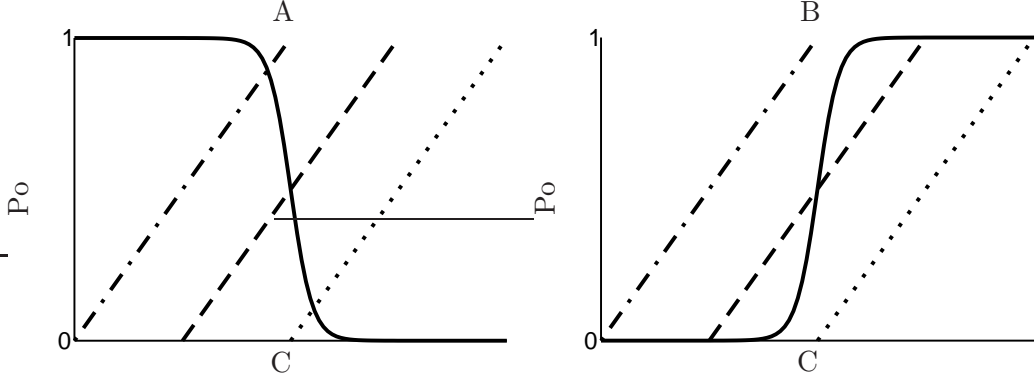


Figure 2.4: Graphical solution to the equation giving the stationary points of the simple model of hair-bundle dynamics, eqs. 2.30 - 2.32. Intersections of the lines indicate the solution, the ordinate indicates the stationary open probability, the abscissa the stationary calcium-concentration. Two cases arise in depending on the sign of R' : A, $R' < 0$, which allows for exactly one solution; B, $R' > 0$, which can result in either one, two (marginal case), or three solutions. The latter case can only occur if $\frac{C_M R'}{4\delta} > 1$.

existence of one solution, whereas $R' > 0$ allows for up to three solutions. A necessary condition for this to occur is $C_M R' / (4\delta) > 1$. For not too strong feedback and for $K_{GS}/K_E + K_{GS}/K_{SP} \ll 1$, the dominant term of this expression is $D/(4\delta) = K_{GS} D^2 / 4k_B T N$. This expression corresponds to the ratio between the energy of the gating-springs and thermal energy. Around the region of greatest slope $1/(4\delta)$ of the open probability P_o , it is sufficient to displace the bundle for the distance of 4δ in order to open or close the channels. Because the transition from the open to the closed state corresponds to the relaxation of the gating-spring by the distance D , the quantity $D/(4\delta)$ also quantifies the degree of nonlinearity in the system. Furthermore, with the help of eq. 2.39, we can see that strong feedback $\gamma f_{\max} S > D K_{GS} (1 + K_E / K_{SP})$ leads to only one stationary solution.

In the following, we will compare the stationary state of this system to some experiments.

2.4.2 Dependence of stationary states on the external calcium-concentration

It has been observed that the external calcium-concentration influences the opening probability of the mechanically unperturbed hair-bundle [15]. This experiment is done by stimulating several hundred of hair cells simultaneously, by moving a patch of the otolithic membrane which overlies the hair-bundles in the sacculus of the bullfrog, via a glass probe, see [15] for details. A displacement-current curve is recorded for different values of the external calcium-concentration in which the hair-bundles are immersed. As the inflowing current is proportional to the open probability of the bundle P_o , the displacement-current curve can be viewed as a

displacement-open probability curve. The displacement necessary for an opening-probability of 0.5 is recorded as a function of the external calcium-concentration, see fig. 2.5 .

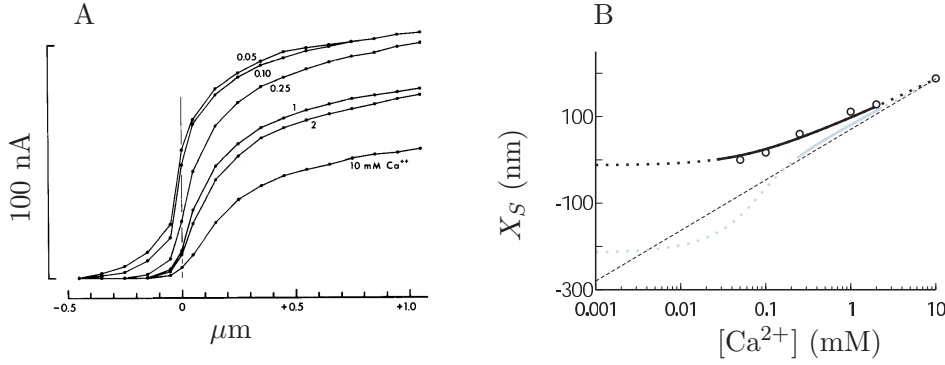


Figure 2.5: Shift of the current-displacement curve in dependence on the apical calcium-concentration, experiments from [15] and comparison to numerical simulations. A, Receptor current as function of the displacement of the hair-bundle. Note the decrease of maximum current at high calcium-concentrations. This reduction does not mean that the maximum calcium-concentration inside the hair-bundle decreases in the same way, see [69]. The curve both shifts to the right and has a smaller maximum slope for higher Calcium concentrations. Note the strongly non-symmetrical form of these curves. B, Plot of the shift X_S necessary to activate half the maximum current as a function of the Calcium concentration (hollow circles), reported from figure A. Two curves are indicated showing the value of X_S for our model eqs. 2.30 - 2.32. Black lines: stationary points with parameters from column B of table B.1 in appendix B, with f_{\max} chosen so that the maximum open probability is 0.6. Grey lines: same as before, but f_{\max} chosen so that the maximal open probability is 0.99, see column C of table B.1 in appendix B. The solid parts of the lines correspond to $0.075 < P_o < 0.53$, the range which is covered by the experimental points. This range of open probabilities corresponds to $3.24 < S < 0.045$ and $5.7 < S < 0.58$ for the maximal open probabilities 0.6 and 0.99, respectively. Both curves have been vertically aligned, so that $X_S = 0$ corresponds to $P_o = 0.53$, matching the values obtained by the experiment. Both curves have additionally been shifted horizontally. Note that a horizontal shift corresponds to a rescaling $C_M \rightarrow C_M/a$, $C \rightarrow C/a$, $p' \rightarrow p'a$. The dashed line corresponds to the slope $\frac{\delta(K_{GS}+K_{SP})}{K_{SP}}$, to which both lines are parallel for large C_M .

In this experiment, it has been observed that the displacement X_S required to activate half the maximum current depends logarithmically on the external calcium-concentration, $X_S \sim D_S \ln[Ca^{2+}]$, with a slope $D_S \sim 37$ nm. Additionally, the maximum slope of the displacement-current curve diminishes with increasing $[Ca^{2+}]$. Note also that the curves are strongly non-symmetrical. However, as several hundreds of cells have been measured simultaneously, with the excitatory directions not strictly parallel, this might be an artifact of the measurement.

The stationary motor-position X_a in our model corresponds to the shift X_S : a change of X_a in eq. 2.24 implies a change of the displacement X necessary

to obtain a given open probability. The value of the maximal motor force f_{\max} determines the maximal open probability of the channels. Because this maximal open probability cannot be deduced from the data in the experiments, two different values of f_{\max} have been used in fig. 2.5 to illustrate the different shapes of the curves relating the stationary value of X_a and the external calcium-concentration $[\text{Ca}^{2+}]$ which can be expected.

The experiment shows that reduced $[\text{Ca}^{2+}]$ leads to an increased open probability P_o . The displacement-current curves can be used to estimate the gating force $K_{GS}D$: using eq. 2.25 and eq. 2.24, the maximum slope of the curve corresponds to $1/(4\delta)$. Using $N = 50$, the gating force varies between 8 and 2 pN. With an estimate of $K_{GS} = 600\mu\text{Nm}^{-1}$ [82], the value of the gating-swing is $D \sim 3 - 13$ nm. This indicates of course, that the parameters K_{GS} or D , or both, depend on the apical calcium-concentration. Note that the decrease of the maximum slope of the displacement-current curve corresponds to decreasing K_{GS} and D with increasing $[\text{Ca}^{2+}]$. This phenomenon has not been included in the model so far. We will come to that point in chapter 6. For the moment, we discard the possibility of calcium-dependent K_{GS} and D .

Our model, eqs. 2.30-2.32, allows for the calculation of the stationary motor-position X_a in dependence on the maximum $[\text{Ca}^{2+}]$ at the location of the motors, C_M . There is a regime in which $X_a \propto \ln C_M$ holds. Under the assumption that $C_M \propto [\text{Ca}^{2+}]$, we do therefore have a regime in which our model recovers the behavior observed in the experiment, $X_s \propto \ln [\text{Ca}^{2+}]$.

Indeed, if C_M is large enough⁶, so that the terms in $1/C_M$ can be neglected in the expressions for R and R' , and $P_o \ll 1$, 2.36 becomes:

$$C = -\frac{\delta}{R'}(\ln C_M - \ln(C - C_0)) - \frac{R}{R'}. \quad (2.42)$$

For $|C| \ll |-\delta/R'|$, we see that $C \sim -(\delta/R') \ln C_M$. Note that $C \sim -(\delta/R') \ln C_M$ also implies that $R' < 0$ in order to reproduce the experimental observation that $P_o = (C - C_0)/C_M$ decreases with increasing C_M . This implies therefore $p' < 0$ (see eqn. 2.39): the binding-probability of the molecular motors increases when the calcium-concentration decreases. Therefore, active force generation increases when the calcium-concentration decreases, an observation which has also been made in other experiments [37].

In this case ($C \sim -(\delta/R') \ln C_M$), the stationary solution of the motor position becomes

$$X_a \simeq \delta \ln C_M \frac{(K_{GS} + K_{SP})}{K_{SP}} \quad (2.43)$$

This linear regime is only achieved for small opening probabilities, and under the assumption that $C_M \propto [\text{Ca}^{2+}]$. Therefore, our model will not yield $X_a \propto \ln C_M$ for $P_o \simeq 0.5$.

⁶ $C_M \gg \frac{DC_0K_{GS}(K_E+K_{SP})}{F_{\max}+K_{SP}+K_EK_{SP}(X_E+\frac{F_{\text{ext}}}{K_{SP}})}$ and $C_M \gg \frac{DC_0K_{GS}(K_E+K_{SP})}{K_{SP}F_{\max}p'/p_0}$

Note that $C \sim -(\delta/R') \ln C_M$ also implies that $R' < 0$ in order to reproduce the experimental observation that $P_o = (C - C_0)/C_M$ decreases with increasing C_M . This implies therefore $p' < 0$ (see eqn. 2.39): the binding-probability of the molecular motors increases when the calcium-concentration decreases. Therefore, active force generation increases when the calcium-concentration decreases, an observation which has also been made in other experiments [37].

As a comparison to the experiment, fig. 2.5 B shows both the dependence of the stationary motor-positions X_a calculated for our model, and the experimentally observed displacement X_S . Two different sets of curves have been plotted, differing only by the value of F_{\max} , which determines the maximum open probability of the stationary state of the hair-bundle: the higher f_{\max} , the higher the maximum open probability. The value of $D = 17$ nm has been chosen, in order to fit approximately the slope of the experimental points. The value of f_{\max} has been chosen to yield a maximum open probability of respectively 0.6 (black curves) and 0.99 (grey curves). The solid portions of the curves correspond to the opening probabilities observed in the experiment, $0.075 < P_o < 0.53$. The dashed line represents the slope $\delta(K_{GS} + K_{SP})/K_{SP}$, to which both lines are parallel for large C_M . Note that the range in X_a covered by the experimental data is much larger than the corresponding range given by the theory, for a given range of P_o . It is not possible to adjust both values with our simple model, equations 2.30-2.32, because with $C - C_0 = C_M P_o$, we have $\ln C \sim \ln P_o \delta/R'$ under the same condition $|C| \ll |\delta/R'|$, and therefore we can estimate $X_a \sim -\ln P_o \delta(K_{GS} + K_{SP})/K_{SP}$.

We have seen that our model provides a partial agreement with the experimentally observed effects of the variation of $[\text{Ca}^{2+}]$. It is clear that a dependency of K_{GS} and/or D on C has to be taken into account for better agreement. The experiments, however, have been performed simultaneously on several hundreds of cells, which were not perfectly aligned, and do therefore not perfectly reflect the properties of a single hair-bundle, which has been discussed theoretically.

2.4.3 The extent spring K_E

The observation of incomplete adaptation (see 1.5) has led to the introduction of the gating-spring K_E in the description of the hair-bundle presented in equations 2.30-2.32. The extent of adaptation has been measured for hair cells of the bullfrog's sacculus [99]. In these experiments, displacement-current curves of the hair-bundle are recorded to measure the shift of these curves as a function of the magnitude of static deflections of the hair-bundle. If a hair-bundle shows complete adaptation, the shift of the displacement-current curve is expected to have the same value as the static deflection of the hair-bundle: after adaptation, the bundle would have restored the same open probability as it had in its resting position. This is not the case, and the extent of adaptation can be seen in fig. 2.6. Note the nick in the slope, which can be interpreted as the maximum displacement of the motors towards the tip of the stereocilia. The stationary motor position X_a

in our model corresponds to the adaptive shift X_e in this measurement.

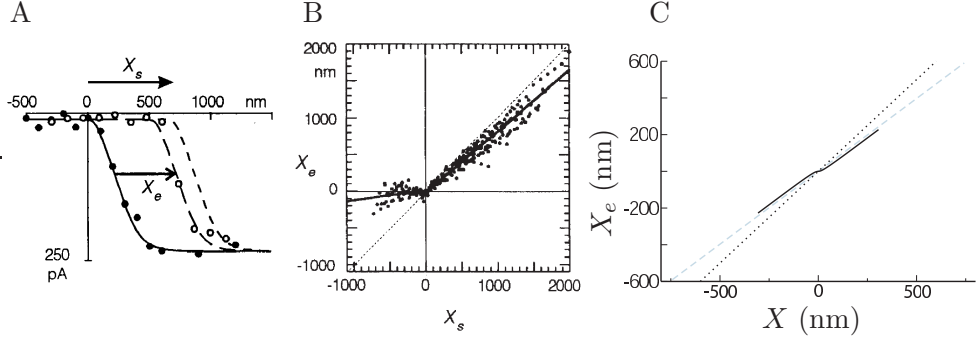


Figure 2.6: Shift of the displacement-current curve in dependence of a statically imposed deflection, experiments from [99] and comparison to numerical simulations. A, displacement-current curves before (solid circles, solid lines) and after a static deflection X_S (hollow circles, long dashes) as well as the displacement-current curve shifted by X_S (short dashes). The adaptive shift is denoted by X_e . B, superimposed results for 11 cells and 15 measurements. The nicks of the measurements have been aligned. These nicks correspond to a maximum motor position $-X_e$ beyond which the motors cannot climb. The slope of this curve is 0.8. The dotted line has a slope of 1, which the system would display if complete adaptation occurred. C, Stationary values yielded by equation 2.44. Two sets of parameter values have been used: Dashed line, weak nonlinearity, $D = 10$ nm, see column D of table B.1 in appendix B. Solid line, strong nonlinearity, $D = 40$ nm, see column E of the same table. As a comparison, the line corresponding to complete adaptation (slope 1) is indicated (dotted line). The curves have been aligned so that $P_o = 0.5$ corresponds to $X = X_e = 0$, and values for $0.001 < P_o < 0.999$ ($D = 40$ nm) respectively $0.1 < P_o < 0.9$ ($D = 7$ nm) have been plotted

These results thus suggest a roughly linear relation between the stationary positions of X_a and X , with $\Delta X_a / \Delta X \simeq 0.8$. Using equation 2.31, we can obtain the stationary value of X as a function of the stationary value of X_a without explicitly including the external force F_{ext} :

$$X = X_a \frac{K_{GS} + K_E}{K_{GS}} + DP_o \left(1 - \frac{\gamma f_{\text{max}} S}{K_{GS} D}\right) + \frac{\gamma f_{\text{max}} S}{K_{GS}} \frac{C_0}{C_M} + \frac{F_{\text{max}}}{K_{GS}} \quad (2.44)$$

$$\frac{\partial X}{\partial X_a} = 1 + \frac{K_E}{K_{GS} \left(1 - DP_o \left(\frac{\gamma f_{\text{max}} S}{K_{GS} D} - 1\right)\right)} \quad (2.45)$$

The latter expression is the derivative of eq. 2.44 with respect to X_a under variation of the external force F_{ext} , by fixing all other parameters.

Therefore, non-vanishing feedback $\gamma f_{\text{max}} S$ and gating-swing D lead to nonlinearities of the relation between X and X_a , localized around $P_o = 0.5$. However, this will not be noticeable if $D^2 \ll |(4k_B T N / K_{GS})(K_{GS} D) / (\gamma f_{\text{max}} S - K_{GS} D)|$. Note that this condition is similar to the condition of having the negative stiffness introduced in section 1.5 and described in 3.2.1, which occurs if $D^2 > (4k_B T N / K_{GS})(K_{GS} - K_{SP}) / K_{GS}$.

This experiment does not show a marked nonlinearity in the relation between the displacement X and X_a . However, this preparation was not done by using the two-compartment technique described in 1.6. The largest values of D have been observed in experiments using this special technique, see for example [82]. We can again estimate the gating-force $K_{GS}D$ for this experiment, as described in 2.4.2. The slope of the displacement-current curve yields $K_{GS}D \simeq 4$ pN, and with $K_{GS} = 600\mu\text{Nm}^{-1}$ we obtain $D \simeq 7$ nm. Therefore, without a value of $\gamma f_{\max}S/K_{GS}D \ll 1$, we cannot resolve this nonlinearity in the plot of fig. 2.6.

Fig. 2.6 C shows a typical plot of the relation between X and X_a for our model. The parameter values are chosen so that they are close to the values which can be inferred from this experiment. The resulting curve corresponds to the dashed line. As a comparison, another curve has been plotted, with a much larger value of D (solid line).

Chapter 3

Theory of hair-bundle oscillations

3.1 State Diagram

To explore the dynamic behaviors of the system described by eqs. 2.30-2.32 and eq. 2.24, we first ignore the effects of fluctuations and assume $F_{\text{ext}} = 0$. Linear stability analysis of these steady states reveals conditions for stability as well as for oscillating instabilities that lead to spontaneous oscillations via a Hopf bifurcation [104]. As the calcium-dynamics at the motor site is expected to be much faster than the hair-bundle oscillations observed in the bullfrog's sacculus [68], we determine the state diagram for $\tau = 0$ (fig. 3.1). The state diagram is a function of two parameters: the maximal force f_{max} produced by adaptation motors along their axis of movement, and the dimensionless feedback strength S of the Ca^{2+} -regulation. We assume that Ca^{2+} -feedback reduces active force generation by the motors ($S > 0$, see subsection 2.4.2).

The state diagram exhibits different regimes (fig. 3.1). If the force f_{max} is small, the motors are not strong enough to pull transduction channels open. In this case, the system is monostable with most of the channels closed. Increasing f_{max} leads to channel opening. For intermediate forces and weak Ca^{2+} -feedbacks, the system is bistable, i.e. open and closed channels coexist. For strong Ca^{2+} -feedbacks, however, the motors can't sustain the forces required to maintain the channels open. In this case, the system is again monostable with most channels closed. Spontaneous oscillations occur in a region of both intermediate forces and feedback strengths. The boundary between a stable state and an oscillatory state corresponds to a Hopf bifurcation. This bifurcation is subcritical near the bistable region (broken line in fig. 3.1) but becomes supercritical at larger motor forces (solid line in fig. 3.1). Note that there is no oscillation in the absence of Ca^{2+} -feedback, i.e. for $S = 0$. Close to the subcritical Hopf bifurcation, regions of coexistence between the oscillating and one or two stable states exist only in a very

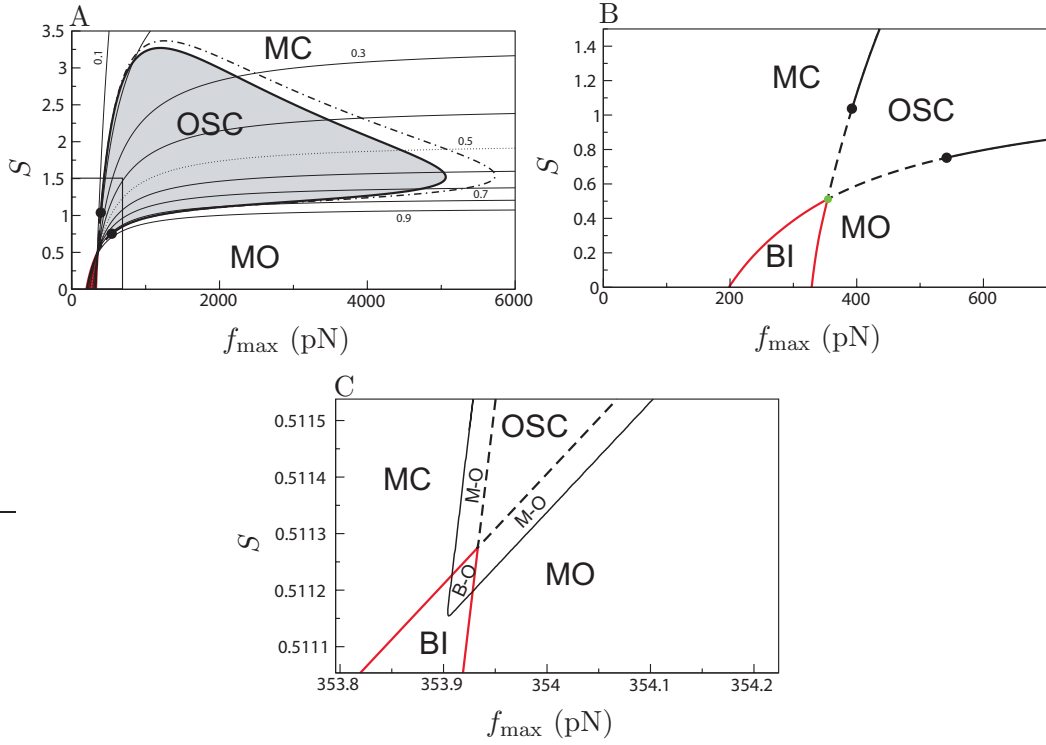


Figure 3.1: State diagram of the hair-bundle as a function of the maximal force f_{\max} of the motors along the axis of the stereocilium, and the dimensionless feedback strength S . Lines of constant opening probabilities are drawn in A, indicated by the numbers. They are drawn in steps of $P_o = 0.1$. All figures show the same state diagram. A, global view. B, blowup of the region indicated by the rectangle in A. C, blowup indicated by the green point in B. Three different states can be distinguished: a bistable state (BI, delimited by the red line), an oscillating state (OSC, shaded region in A), a monostable state (MO: open state, $P_o > 0.5$; MC: closed state, $P_o < 0.5$). In C, two coexistence regions between stable states and an oscillating state can be seen: B-O, coexistence between an oscillating state and two stable states; with two stable and one oscillating state. M-O, coexistence between a monostable and an oscillating state. Hopf bifurcations occur along the line separating oscillating from stable states. For small f_{\max} , the bifurcation is subcritical (broken line), whereas it becomes supercritical for larger forces (solid line). Parameter values are given in column F of table B.1 in appendix B. The dashed-dotted line in A corresponds to the Hopf bifurcation for the same parameters as before, but with $\tau = 0.1$ ms.

small region around the subcritical bifurcation (fig. 3.1 C). The dashed-dotted line in fig. 3.1 A corresponds to the Hopf bifurcation for a finite value of $\tau = 0.1$ ms.

This state diagram has been drawn under the assumption of a very fast calcium-relaxation time τ . The model described by eqs. 2.30-2.32 does exhibit regimes of spontaneous oscillations for a variety of parameter values. In the following, we will analyze some limiting cases and discuss the physical origin of the different mechanisms of spontaneous oscillations the bundle displays in each of them.

3.2 Physical mechanisms of oscillations

It is useful to use a simple two-dimensional system of linear differential equations to describe the essence of hair-bundle motion. On the one hand, it allows to understand the different states present in the state diagram, and helps to extract more clearly the mechanism which leads to the oscillating solution. On the other hand, it helps to explain other mechanisms of oscillations, which are presented in the following. This system can be written as follows [81]:

$$\lambda_{\text{eff}} \frac{dX(t)}{dt} = -kX(t) + F_A(t) + F_{\text{ext}}(t) \quad (3.1)$$

$$\beta \frac{dF_A(t)}{dt} = -\bar{k}X(t) - F_A(t) \quad , \quad (3.2)$$

where k denotes the stiffness of the hair-bundle, F_A is the force produced by active elements inside the hair-bundle, F_{ext} is the externally applied force, and λ_{eff} is an effective drag coefficient. The description of the active force with the help of the coefficient β reflects the observation that the speed of adaptation decays exponentially in hair-bundles subject to a constant force. \bar{k} is an approximation to linear order of the coupling between active elements and the movement of the hair-bundle.

The dynamical state of the fixed point of this system $X = 0$ and $F_A = 0$ at zero external force is determined by its eigenvalues :

$$s_1 = -\frac{Tr}{2} - \sqrt{\frac{Tr^2}{4} - \Delta} \quad (3.3)$$

$$s_2 = -\frac{Tr}{2} + \sqrt{\frac{Tr^2}{4} - \Delta} \quad , \quad (3.4)$$

where $Tr = 1/\beta + k/\lambda_{\text{eff}}$ denotes the trace of the matrix determining the system 3.1-3.2, and $\Delta = (k + \bar{k})/(\lambda_{\text{eff}}\beta)$ denotes its determinant.

If $Tr < 0$ and $\Delta > 0$, the real part of the eigenvalues is negative and the system is quiescent. If, however, one of the eigenvalues has a positive real part ($Tr > 0$ or $\Delta < 0$), the system is linearly unstable. It undergoes a Hopf bifurcation at the critical point $Tr = 0$ with the characteristic angular frequency $\omega = \sqrt{\Delta}$ if $\Delta > 0$ at the critical point. If nonlinearities restrict the values of X and F_A , the system undergoes limit-cycle oscillations around the fixed point if $1/\beta < -k/\lambda_{\text{eff}}$ in the vicinity of this critical point.

In the following, we will discuss several physical mechanisms of oscillation for the system presented in 2 by analyzing several limiting cases. We will apply the resulting two-dimensional equations to the simple description 3.1-3.2 in order to have a general description for the different cases.

Useful shortcuts in the following discussion are the following quantities:

$$K_{GP} = K_{GS}(1 - DP'_o) \quad (3.5)$$

$$P'_o = \frac{dP_o}{dX} = \frac{P_o(1 - P_o)}{\delta} \quad (3.6)$$

$$K_{PP} = K_{SP}K_{GP} + K_{SP}K_E + K_{GP}K_E \quad . \quad (3.7)$$

With these notations, we see that a fixed point verifying $C_MR'P'_o > 1$ implies that this is an intermediate fixed point. In this case, two other solutions with different P_o coexist with this intermediate solution.

In all cases analyzed below, the condition $\Delta < 0$ is identical with the condition for the existence of an intermediate fixed point, $C_MR'P'_o > 1$ (see subsection 2.4.1). This implies that the Hopf bifurcation can occur in regions with only one fixed point, and in regions with three fixed point. In the latter case, the bifurcation can only occur on solutions situated on either the left or the right branch of the three solutions which are depicted in fig. 2.4 B. Although the unstable solution of the intermediate fixed point can possess a stable limit cycle¹, a coexistence of such a solution with another stable solution would result in the possibility of the system being attracted to the stable fixed point. Therefore, the condition $\Delta < 0$, although corresponding to an unstable solution, does not necessarily represent an oscillating solution. On the other hand, an oscillating solution exists if there is only one fixed point, or if all three fixed points are unstable. Therefore, for all the cases discussed below, an oscillating solution is found for the two conditions $Tr > 0$ and $\Delta > 0$, because this corresponds to unstable solutions in a region with one fixed point. In order to explore the system's ability to display oscillations, we will therefore test if the system allows for solutions with $Tr > 0$ and $\Delta > 0$.

3.2.1 Fast calcium-feedback

The state diagram fig. 3.1 corresponds to this limit. The oscillation mechanism discussed here concerns the dynamics of the bundle if the time constant determining the dynamics of the calcium-concentration, τ , is very small. This limit may be justified by the observation that calcium-dynamics takes place on a sub-millisecond scale, as proposed by different authors [68], whereas typical oscillations take place at a timescale of tens of milliseconds. This mechanism of oscillation is powered by the adaptation motors, which constantly push the bundle into an unstable position, as explained below.

In the limit $\tau \rightarrow 0$, we can rewrite the linearized system (eqs. 2.30 - 2.32) in

¹The intermediate fixed point ($\Delta < 0$) is a saddle point. As a consequence of the index theorem [104] a hypothetical limit cycle in a system including two stable states and a saddle point would have to enclose all three fixed points.

the form of the simplified system (eqs. 3.1 - 3.2) with

$$F_a = K_{GP}X_a \quad (3.8)$$

$$k = K_{GP} + K_{SP} \quad (3.9)$$

$$\bar{k} = -K_{GP} \frac{K_{GP} + P'_o \gamma f_{\max} S}{K_{GP} + P'_o \gamma f_{\max} S + K_E} \quad (3.10)$$

$$\beta = \frac{\lambda_a}{K_{GP} + P'_o \gamma f_{\max} S + K_E} \quad (3.11)$$

$$\lambda_{\text{eff}} = \lambda \quad (3.12)$$

Note that there is no Hopf bifurcation without calcium-feedback in this limit ($S = 0$)².

We can see that $Tr = -k/\lambda - K_{GP}/\lambda_a - K_E/\lambda_a - \gamma f_{\max} S P'_o/\lambda_a$, and $\Delta = K_{PP}/\lambda_a \lambda + K_{SP} \gamma f_{\max} S P'_o/\lambda_a \lambda_{\text{eff}}$. Note that $k < 0$ is a sufficient condition for $K_{PP} < 0$. At the bifurcation, we find

$$\omega_c = \frac{\sqrt{\frac{K_{GP} K_E \lambda}{\lambda_a} - K_{SP} k}}{\lambda} \sim \frac{\sqrt{-K_{SP} k}}{\lambda}, \quad (3.13)$$

the latter expression becoming exact for $K_E/\lambda_a \ll K_{SP}/\lambda$. The frequency at the bifurcation is therefore dominated by the relaxation rate associated with the negative stiffness and the relaxation rate associated with the stereociliary pivot elements.

Unstable solutions in regions with one fixed point, with $Tr > 0$ and $\Delta > 0$, are found for $k < (\lambda/\lambda_a)(K_{GP} K_E/K_{SP})$. Therefore, k has to be reasonably small. In the limit $K_E \rightarrow 0$, or if $K_{GP} < 0$, we see that $k < 0$ is a necessary condition for the existence of an unstable solution. This kind of oscillation is therefore created by the existence of a negative stiffness, $k < 0$ ³. Negative stiffness has been observed experimentally [82]. This mechanism of oscillation has already been studied, see for example [78, 82]. However, the model used in these studies was more complicated, and these studies did not include the influence of noise.

In order to explain this mechanism, we can plot the free energy of the hair-bundle, $-k_B T \ln Z$, as a function of the position X , as well as the displacement-force relation at given motor position, eq. 2.15, for fixed motor-position X_a . The fig. 3.2 shows this situation for three different positions of the motors X_a . Minima of the energy curves in the top row correspond to stable states of the system.

The left column corresponds to a high value of X_a , which is achieved for example if f_{\max} is low. The tension of the tip-links is low, and the channels are

² $Tr = 0$ implies either $k < 0$ or $K_{GP} + K_E < 0$, which implies that $K_{PP} < 0$, so that $\Delta < 0$

³if $K_{GP} > 0$, we see that $K_{SP} < (\lambda/\lambda_a)K_E$ in order to allow for the unstable solution $Tr > 0$ and $\Delta > 0$. Estimates of the friction constants indicate however that $\lambda \ll \lambda_a$ [23, 44, 37]. The stiffnesses K_{SP} and K_E are of the same order of magnitude [43, 99, 82]. Therefore, this case is unlikely to occur in the hair-bundle.

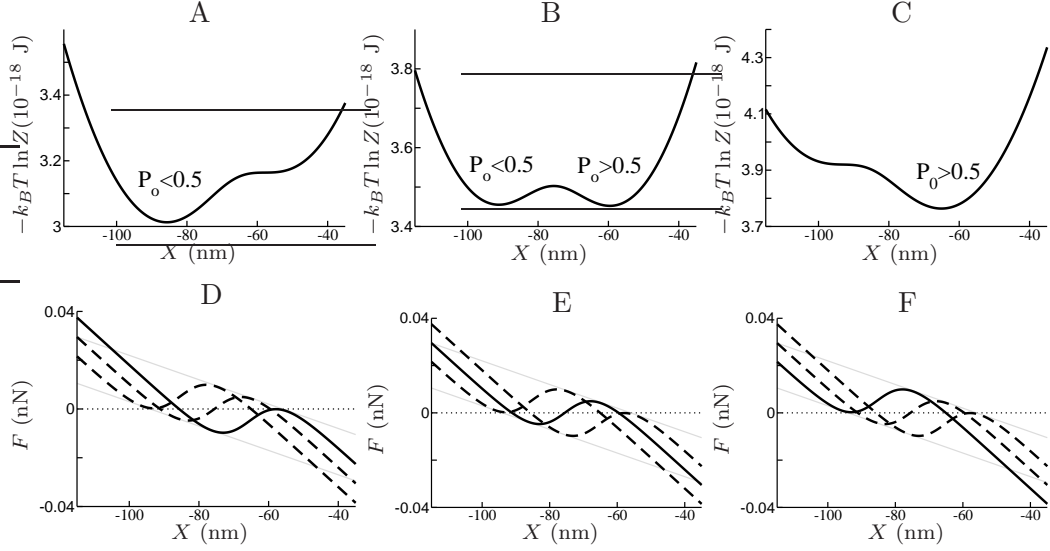


Figure 3.2: Free energy landscape of the hair-bundle and associated force F , eq. 2.15, for different motor-positions X_a . Minima of the energy-curves correspond to stable states. From left to right: decreasing motor-position X_a , corresponding to increasing motor force f_{\max} . Left column: high motor-position X_a , i. e. the motors are found far from the tip, cf. fig. 2.2. The tension in the tip-links is low, and the system exhibits one stable state with low P_o . This corresponds to a low value of f_{\max} . Middle column: intermediate values of X_a and f_{\max} result in a bistable state, with an unstable intermediate position. Right column: low values of X_a corresponding to high f_{\max} increase the tension in the tip-links and force the channels to open, resulting in a high value of P_o . Bottom row: displacement-force relation F . The solid line corresponds to the energy depicted above every figure, the two dashed lines to the other values. Intersections with the zero-line (dotted line) with negative slope correspond to stable states, whereas positive slopes represent unstable states. Varying the motor-position X_a results in a shift of the displacement-force curves characterized by the slope $-K_{SP}$ (grey lines).

closed. The middle column is drawn for intermediate values of X_a and f_{\max} . This results in an unstable fixed point and two stable fixed points, cf. fig. 2.4 B. The last column, finally, corresponds to a high value of f_{\max} and a low value of X_a . The tension of the tip-links is high and the channels tend to be open. The bottom row of the figure depicts the displacement force curves for the three values of X_a . The solid line corresponds to the value of the X_a which has been used in the figure just above it, while the dashed curves correspond to the other two values of X_a .

Oscillations become possible when the position of the motors is no longer fixed, but becomes a dynamic variable according to eq. 2.31. If the position of the motors corresponds to the situation depicted in the left column, the negative feedback will increase their activity due to the low open probability and consequently low internal calcium-concentration. The motors will begin to climb up the stereocilium, thereby decreasing the value of X_a , pushing the system in the direction of the state depicted in the middle column.

If the position of the motors corresponds to the situation depicted in the right

column, the negative feedback will decrease their activity due to the high open probability and consequently high internal calcium-concentration. The weak motors will not be able to stand the high tension of the tip-links and slide down the stereocilium, pushing the system in the direction of the state depicted in the middle column.

The negative calcium-feedback has therefore the effect to shift the system's open probability closer to the open probability $P_o = 0.5$.

If the feedback is strong enough, the movement of the motors will shift the systems state from the situation depicted in the left column directly to the one depicted in the right column, with the bundle's position being given by the left hand side minimum. When the left hand side minimum of the energy curve becomes unstable (right column), the bundle's tip will rapidly assume the position given by the right hand side minimum, thereby displaying a rapid movement in the positive direction.

Once the bundle has assumed the right hand side minimum depicted in the right column, the cycle restarts in the opposite direction.

We can also follow the movement of the bundle with the help of the displacement-force curves, drawn in the bottom row of the figure. Stable positions correspond to $F = 0$, with F having a negative slope at this point. It is furthermore quite easy to see that the open probability is larger than 0.5 for one half of the cycle, and smaller than 0.5 for the other half. Only the jumps from the left hand side stable point to the right hand side stable point and vice versa change the value of the sign of $P_o - 0.5$, because $P_o = 0.5$ corresponds to the point of maximal slope in the displacement-force curves.

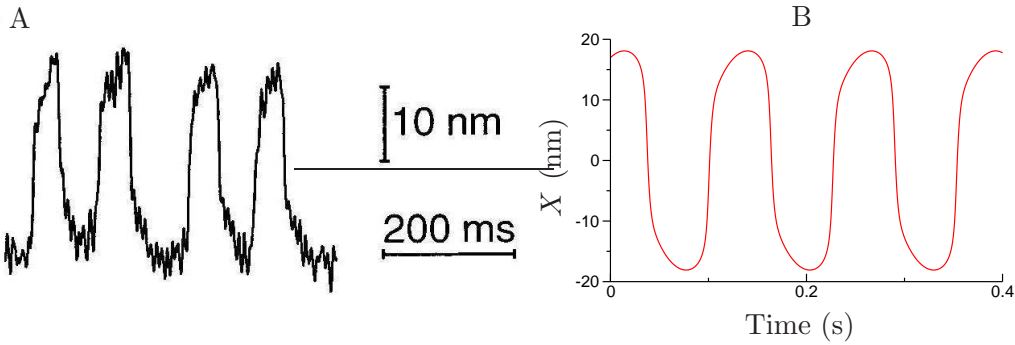


Figure 3.3: Spontaneous oscillations of a hair bundle, experiment and numerical simulation. A, spontaneous oscillations of the tip of a hair-bundle of the bullfrog's sacculus. Taken from [81]. B, numerical simulations for our system eqs. 2.30-2.32 under the assumption of fast calcium-relaxation. Note the similar shape of the oscillations. Parameters are given in column G of table B.1 in appendix B.

The shape of the oscillations, which can be seen in fig. 3.3 B, is similar to the shape of oscillations of hair-bundles from the sacculus of the bullfrog [80], see

fig. 3.3 A. The bundle displays swift strokes followed by longer periods in which it shows a more erratic movement. Note that the bundle's slow phase of motion includes the maxima of displacement; the rapid phase of the movement does not begin when the bundle is situated in one of its extremal positions. This feature is faithfully reproduced by our simulations, fig. 3.3 B.

This peculiar shape of oscillations is generic for the limit of small calcium-relaxation times. A change of the motor-position changes the expression for the displacement-force relationship eq. 2.15. The displacement force relation is anti-symmetric with respect to X in the following way:

$$F(X - X_{off}) - F(X_{off}) = -F(-X + X_{off}) - F(X_{off}) \quad (3.14)$$

with X_{off} given by

$$X_{off} = \frac{N\Delta G}{K_{GSD}} + X_a + D/2 \quad (3.15)$$

for the simple model presented in section 2.4. For the displacement $X = X_{off}$, the system displays the open probability $P_o = 0.5$. In response to a change of the motor position $X_a \rightarrow X_a + \Delta X_a$, the displacement-force relationship will change its position by

$$\Delta X_{off} = \Delta X_a \quad (3.16)$$

$$\Delta F(X_{off}) = -K_{SP}\Delta X_a \quad (3.17)$$

Therefore, changing the value of X_a shifts the displacement-force relationship on a slope given by $-K_{SP}$, which is indicated by the grey lines in the bottom row of fig. 3.2. In the case of a spontaneously oscillating hair-bundle, the external force is zero. We assume a rapid relaxation of the hair-bundle's tip to the stable position given by $F = 0$. Following the trajectory of the position $F = 0$ during the shift of the displacement-force relation allows us to predict the direction of movement: as long as the slope of F at the position $F = 0$ has a larger magnitude than the slope $-K_{SP}$, the displacement of the bundle's tip has the same direction as the shift of X_{off} . If, however, the slope of F at this position has a smaller magnitude than the slope $-K_{SP}$, the direction of movement of the hair-bundle has the opposite sign of the direction of movement of X_{off} .

We can therefore predict the shape of hair-bundle oscillations using fig. 3.2. Consider the situation depicted in part D of the figure. The position of the bundle is given by the position $F = 0$ on the left hand side of the figure. The motors will now begin to climb up the stereocilia, shifting the displacement-force relation along the slope indicated by the grey lines. This slow movement will continue until the motors reach the position which is depicted in part F of the figure, where the slope of F at the position given by $F = 0$ is zero. Therefore, the bundle's

tip is first displaced parallel to the movement of X_{off} , because the slope of F has a larger magnitude than $-K_{SP}$ at the onset of this phase of the movement. However, as soon as the slope of F has a smaller magnitude than $-K_{SP}$, the direction of movement of the bundle is inverted, corresponding to the extremal positions of X which can be seen in fig. 3.3.

Therefore, the shape of hair-bundle oscillations for fast calcium-relaxation is given by swift strokes connected by arc-like movements of slower phases of displacement, which contain the extremal displacements, similar to the shape of oscillations which has been observed in experiments.

3.2.2 Fixed motor position

Another useful limit is the case where $\lambda_a \rightarrow \infty$, i. e. the motors are considered to be immobile [107]. This limit may be justified by the observation that the dynamics of the adaptation motors $\lambda_a/(K_{GP} + K_E)$, is very slow with respect to the other time-constants in the system, see B. The authors of [107] use nearly the same equations as the ones presented here, eqs. 2.30-2.32. There are two differences between their treatment of the problem and the discussion presented in this subsection. First, the probability used by the authors is governed by a three-state channel dynamics, one open and two closed states; this difference, however, is of no particular importance, the model showing similar behavior for a two-state channel dynamics. The second difference is more substantial: the authors introduce a calcium-dependent open probability function P_o , based on the experimentally observed shift of the displacement-current curve described in subsection 2.4.2. The shift of the open probability curve P_o introduced by them is identical with a calcium-dependent free energy difference $\Delta G(C) \propto \ln C$. As shown in subsection 2.4.2, we do not necessarily need a dependence of ΔG on C to observe a shift of this curve which is qualitatively similar to the experiment. However, the basic model, eqs. 2.30-2.32 does not allow for a Hopf bifurcation in the limit of fixed X_a , $\lambda_a \rightarrow 0$, whereas such a bifurcation can occur under the assumption of a calcium-dependent $\Delta G(C)$.

By using the first term of the development of a calcium-dependent free energy change $\Delta G(C) = \Delta G_0 + \Delta G' C$, the parameters of the simplified system (eqs. 3.1 - 3.2) read:

$$F_a = -K_{GS} D \mu C / C_M \quad (3.18)$$

$$k = K_{GP} + K_{SP} \quad (3.19)$$

$$\bar{k} = \frac{K_{GS} D P_o' \mu}{1 + \mu} \quad (3.20)$$

$$\beta = \frac{\tau}{1 + \mu} \quad (3.21)$$

$$\lambda_{\text{eff}} = \lambda \quad (3.22)$$

with $\mu = -C_M \frac{\partial P_o}{\partial C} = C_M P_o' \delta \Delta G' / k_B T$ a dimensionless parameter measuring the

feedback-strength. Note that the stationary solutions still have the same form 2.36 - 2.38, with $R' \rightarrow R' - \delta\Delta G'/k_B T$. This leads to $Tr = -k/\lambda - (1 + \mu)/\tau$ and $\Delta = (k/\lambda\tau)(1 + \mu) + K_{GS}DP'_o\mu/(\lambda\tau)$. Again, we can see that there is no Hopf bifurcation for the case without calcium-feedback, in this case mediated by the dependence of ΔG on calcium⁴.

Unstable solutions for the case without feedback are only possible for $\Delta < 0$, so that these solutions only exist for the intermediate fixed point. Therefore, it is unlikely that an oscillating solution for this case exists: regions with one fixed point are always stable, and regions with 3 fixed points have 2 stable fixed points coexisting with the unstable intermediate one. However, if $\Delta G' \neq 0$, the situation is changed, and we can see that $\Delta = -(k/\lambda)^2 - K_{GS}DP'_o(1/\tau + k/\lambda)/\lambda$ at the Hopf bifurcation. We see that $\Delta > 0$ is possible, if $k < -\lambda/\tau - k^2/(K_{GS}DP'_o)$. Therefore, a necessary condition for a Hopf bifurcation is again the negative stiffness, $k < 0$. Rewriting $\Delta = -(k/\lambda)^2 + K_{GS}DP'_o\mu/(\lambda\tau)$ at the bifurcation allows for the conclusion that $\mu > 0$ and therefore $\Delta G' > 0$ is necessary to allow $\Delta > 0$ at the bifurcation. The frequency at the bifurcation,

$$\omega_c = -\frac{k}{\lambda} \sqrt{-1 - \frac{K_{GS}}{k} DP'_o \left(1 + \frac{\lambda}{k\tau}\right)} \quad , \quad (3.23)$$

is dominated by the relaxation rate associated with the negative stiffness.

Unstable solutions in regions with one fixed point, with $Tr > 0$ and $\Delta > 0$, are found for $-k\tau/\lambda > DP'_o K_{GS}/(K_{GS} + K_{SP})$, showing that the ratio of chemical to mechanical time constants, $-k\tau/\lambda$, has to be larger than a certain value, thereby forbidding too fast chemical relaxation rates.

Both this mechanism and the previous one exhibit oscillations due to strong nonlinear effects, which lead to a region of negative stiffness, $k < 0$. If the timescales of the passive component, $-\lambda/k$, and the active component, β , are sufficiently separated, the system exhibits relaxation oscillations. In both cases, the time-constant associated with the negative stiffness, $-\lambda/k$, has to be smaller than the time-constant associated with the active component, β , in order to permit $Tr > 0$.

Both systems exploit the regions of negative stiffness. The difference is the way in which they reach these regions. In the first case, the calcium-dependent motor-activity shifts the motor-position X_a in such a way that the stiffness of the hair-bundle becomes negative. In the second case, at fixed motor-position, the calcium directly influences the shape of the energy landscape describing the passive mechanics of the hair-bundle, and so forces the system periodically into regions of negative stiffness.

The discussion of the oscillating mechanism using fig. 3.2 can be done in exact analogy to 3.2.1. However, the displacement-force relation depends no more on X_a , but on ΔG . Therefore, the slope of the migration of the displacement-force

⁴For $\Delta G' = 0$, we have $k/\lambda = -1/\tau$ if $Tr = 0$, and therefore $\Delta = -1/\tau^2 < 0$

relation of fig. 3.2 is no more given by $-K_{SP}$, but by the value $-(K_{GS} + K_{SP})$. This means that the shape of oscillations has changed with respect to the situation discussed in 3.2.1. Now, the swift strokes begin at the extremal positions of hair-bundle displacements, unlike the situation observed experimentally (fig. 3.4).

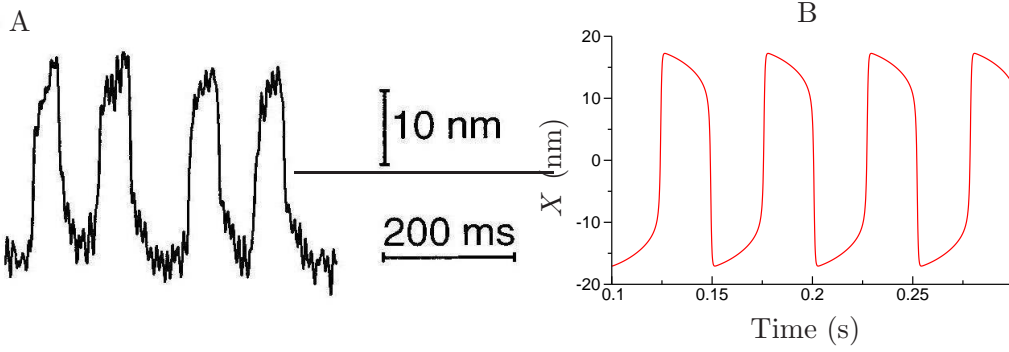


Figure 3.4: Spontaneous oscillations of a hair bundle, experiment and numerical simulation. A, spontaneous oscillations of the tip of a hair-bundle of the bullfrog’s sacculus. Taken from [81]. B, numerical simulations for our system eqs. 2.30-2.32 under the assumption of fixed motor position and calcium-dependent ΔG . Note the dissimilar shape of the oscillations. Parameters are given in column H of table B.1 in appendix B.

Note that this is only one possibility for a calcium-induced oscillation in this limit. If the gating-swing distance, D , is calcium-dependent, the system can also undergo a Hopf bifurcation. Another modification, which will be used in the next subsection, leads also to oscillations: a calcium-dependence of the rest-length of the gating-swing x_{GS} . The slope of the migration of the displacement-force relation for this case is given by $-K_{SP}$ (see section 6.4), exactly the same value as in the case discussed in subsection 3.2.1. The shape of the oscillations for this case is therefore similar to the one found in subsection 3.2.1, see fig. 3.5.

Given the typical relaxation time of molecular motors, $\sim 30\text{ms}$, this oscillation mechanism cannot be applied to oscillation frequencies below $\sim 30\text{Hz}$. Additionally, the slow phase of oscillation is dominated by the timescale of the calcium-dynamics. Therefore, in order to achieve low frequency oscillations ($\sim 10\text{Hz}$), a value of $\tau \gg 1\text{ms}$ has to be chosen. Experimental observations indicate calcium-relaxation times of 1 ms or below. It seems therefore unlikely that this mechanism of oscillation is of importance for the low-frequency oscillations of hair-bundles from the bullfrog’s sacculus. This oscillation mechanism might nonetheless be of importance for hair-bundles which are sensitive to higher frequencies.

3.2.3 Fast mechanical relaxation

In this subsection, we analyze the situation which occurs if the hair-bundle shows a very fast mechanical relaxation, $\lambda \rightarrow 0$. This mechanism might be important for a bundle with a mechanical relaxation rate $\sim \lambda/(K_{GS} + K_{SP})$ which is shorter

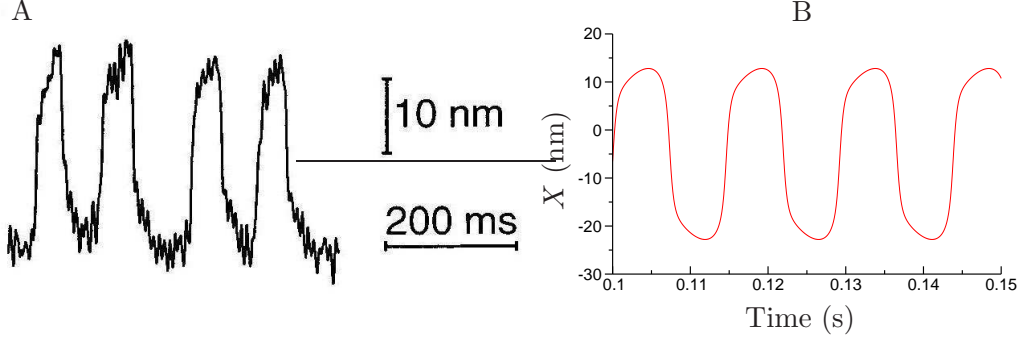


Figure 3.5: Spontaneous oscillations of a hair bundle, experiment and numerical simulation. A, spontaneous oscillations of the tip of a hair-bundle of the bullfrog's sacculus. Taken from [81]. B, numerical simulations for our system eqs. 2.30-2.32 under the assumption of fixed motor position and calcium-dependent x_{GS} . Note the similar shape of the oscillations. Parameters are given in column I of table B.1 in appendix B.

than the other typical time-scales, τ and $\lambda_a/(K_{GS} + K_{SP})$. This might occur in short bundles with many stereocilia. Because both K_{GS} and K_{SP} scale as $1/L^2$, short hair-bundles exhibit a much shorter relaxation time⁵. We will therefore analyze the system consisting of eqs. 2.31 and 2.32, under the assumption that the position of the hair-bundle is slaved with respect to X_a and C . Eq. 2.30 therefore implicitly defines the dependence of X on the dynamical variables X_a and C :

$$-K_{GS}(X - X_a - DP_o) - K_{SP}X + F_{\text{ext}} = 0 \quad . \quad (3.24)$$

Note that this limit is only well defined if eq. 2.30 is linearly stable:

$$K_{GP} + K_{SP} > 0 \quad . \quad (3.25)$$

If this were not the case, the basic assumption of the fast relaxation of X to the value given by 3.24 would not be true. At the very first glance, we can suspect that this system will not show a Hopf bifurcation if we restrict ourselves to the basic system 2.30-2.32: the system does not show negative stiffness due to the condition 3.25, and the calcium-equation is always linearly stable, with the relaxation time τ . Indeed, the calculation results in $Tr = -K_P/((K_{GS} + K_{SP})\alpha) - 1/\tau$. As in the case of fixed motor position, we can recalculate the trace with the help of a calcium-dependent ΔG . The result is

$$Tr = -\frac{K_P}{(K_{GS} + K_{SP})\alpha} - \frac{1}{\tau} \left(1 + C_M P'_o \frac{\delta}{k_B T} \Delta G' \left(1 + \frac{P'_o K_{GS} D}{K_{GP} + K_{GS}} \right) \right). \quad (3.26)$$

As the calcium-feedback, S , has no influence on the value of the trace, we will ignore its contribution and set $S = 0$ in the following. We see that $Tr > 0$

⁵The stereociliary pivot stiffness K_{SP} is thought to be linked to the angular stiffness of the bundle. Therefore, the stiffness measured at the top of the bundle scales as $1/L^2$. The stiffness of the gating-springs K_{GS} scales with γ^2 , and therefore also with $1/L^2$.

can only be brought along by $\Delta G' < 0$. However, it can be shown that $Tr > 0$ implies $R'P_o'C_M > 1$ (if $S = 0$), the condition for the intermediate fixed point. Therefore, a possible Hopf bifurcation always takes place on the intermediate fixed point. It is impossible to find a single fixed point undergoing a Hopf bifurcation. It is thus unlikely to find an oscillating regime for this limit, with $S = 0$.

However, the situation changes if we consider another calcium-dependent element. For example, if the rest-length extension of the gating-swing depends on calcium, we can have a Hopf bifurcation in the one fixed point region. There is no proof that such a dependence exists. Still, the large value of D , which has to be assumed in order to explain recent experiments showing negative stiffness [82], might result from an additional relaxation of elements connected to the channel-complex under the influence of calcium, see for example [78]. Starting from the simple model 2.4, we assume that the rest-lengths $x_{GS,n} = 0$ at the stationary position. Because all equations describing the state of the motor-positions are identical, we write $x_{GS} = x_{GS,n}$ for all gating-spring stiffnesses. In first order, $x_{GS} = x'_{GS}C$, which becomes $X_{GS} = X'_{GS}C$ for the simple model in the reference frame parallel to the apical epithelium, with $X_{GS} = x_{GS,n}/\gamma$. We rewrite eq. 2.30 and the equation for the open probability, 2.24:

$$\lambda \dot{X} = -K_{GS}(X - X_a - X'_{GS}C - DP_o) - K_{SP}X + F_{\text{ext}} \quad (3.27)$$

$$P_o(X, X_a, C) = \frac{1}{1 + Ae^{-\frac{x-x_a-x'_{GS}C}{\delta}}} \quad (3.28)$$

With these modifications of our basic model, the system can show spontaneous oscillations. The parameters of the simplified system (eqs. 3.1 - 3.2) read:

$$F_a = -\frac{(K_{GP} + K_{SP})(\lambda_a - K_E\tau)}{C_M P'_o(\lambda_a + K_{GP}\tau/\mu)} C \quad (3.29)$$

$$k = \frac{K_{SP}(K_{GP} + K_{SP})(\lambda + \frac{K_{PP}}{K_{SP}}\tau/\mu)}{K_{GP}(\lambda_a + K_{GP}\tau/\mu)} \quad (3.30)$$

$$\bar{k} = -\frac{K_{SP}(K_{GP} + K_{SP})(\lambda_a - K_E\tau)}{K_{GP}(\lambda_a + K_{GP}\tau/\mu)} \quad (3.31)$$

$$\beta = \tau \quad (3.32)$$

$$\lambda_{\text{eff}} = \frac{(K_{GP} + K_{SP})^2\tau/\mu}{K_{GP}(\lambda_a + K_{GP}\tau/\mu)} \lambda_a \quad (3.33)$$

The last line corresponds to the fact that the hair-bundle position now has to be calculated via the implicit definition 3.24, and $\mu = C_M P'_o X'_{GS}$, a dimensionless parameter measuring the feedback strength. The external force now couples to both the position of the hair-bundle and to the internal force F_A :

$$\lambda_{\text{eff}} \frac{dX(t)}{dt} = -kX(t) + F_A(t) + f(t) \quad (3.34)$$

$$\beta \frac{dF_A(t)}{dt} = -\bar{k}X(t) - F_A(t) - \frac{\lambda_a - K_E\tau}{\lambda_a + K_{GP}\tau/\mu} f(t) \quad . \quad (3.35)$$

We can see that $\Delta > 0$ corresponds to $\mu < -K_{PP}/(K_{SP}K_E)$. Therefore, Hopf bifurcations only occur for $X'_{GS} < 0$. In this case, increasing calcium reduces the rest-length of the gating spring, increasing the tension in the tip-links. The frequency at the bifurcation,

$$\omega_c = \sqrt{\frac{K_{GP}K_{SP}}{(K_{GP} + K_{SP})\tau\lambda_a} - \frac{K_E K_{PP}}{(K_{GP} + K_{SP})\lambda_a^2}} \sim \sqrt{\frac{K_{GP}K_{SP}}{(K_{GP} + K_{SP})\tau\lambda_a}} \quad ,$$

the latter expression becoming exact if $\lambda_a/K_E \gg \tau$, is a combination of the chemical relaxation rate $1/\tau$ and a mechanical one, $\lambda_a(K_{GP} + K_{SP})/(K_{GP}K_{SP})$.

Unstable solutions in regions with one fixed point, with $Tr > 0$ and $\Delta > 0$, are found for $K_{PP}K_E\tau/(K_{GS}K_{SP}\lambda_a) < 1 - DP'_o$, showing that there is no lower limit for the value of the chemical time constant, τ , whereas a mechanical time constant, $K_{GS}K_{SP}\lambda_a/(K_{PP}K_E)$, should not be too small.

This oscillation mechanism is driven by an instability of the calcium-dynamics⁶,

$$\frac{\partial \dot{C}}{\partial C} = -\frac{1}{\tau} \left(1 + \frac{\mu K_{SP}}{K_{GP} + K_{SP}} \right) > 0 \quad . \quad (3.36)$$

The molecular motors drive the system periodically into regions in which the system is linearly unstable. In contrast to the mechanism consisting of negative stiffness and a calcium-dependent motor-activity driving the system to regions of negative stiffness of the hair-bundle, as described in section 3.2.1, the motor activity need not be calcium-dependent.

A cycle of oscillation (see fig. 3.6) begins with a state of low open probability, low tension of the tip-links, low $[Ca^{2+}]$, and therefore high rest-length ($X'_{GS} < 0$). In this state, the tension of the tip-links is low, and therefore the molecular motors move up the stereocilia, increasing the tension of the tip-links and increasing the open probability. This slow phase of the oscillation is accompanied by the bundle moving the negative direction, because of the growing tension in the tip-links. The increasing tension of the tip-links leads to a higher open probability, and in turn to an increase of $[Ca^{2+}]$, which shortens the rest-length of the tip-links, leading to a greater tension in the tip-links and opening the channels. As the $[Ca^{2+}]$ -dynamics

⁶This is true if $K_E = 0$: in this case, the condition $\Delta > 0$ assures that $K_{PP} > 0$. Because $\partial \dot{X}/\partial X = -K_{PP}/((K_{GP} + K_{SP})\lambda_a) < 0$, the condition $Tr > 0$ can only be achieved if $\partial \dot{C}/\partial C > 0$. For $K_E \neq 0$, there are parameter ranges for which an oscillatory regime exists with $K_{PP} < 0$ and $K_{GP} + K_{SP} > 0$; because the condition for this regime are quite restrictive ($0 < K_{GP} < -K_{SP}$ is a necessary condition), we will not discuss this case.

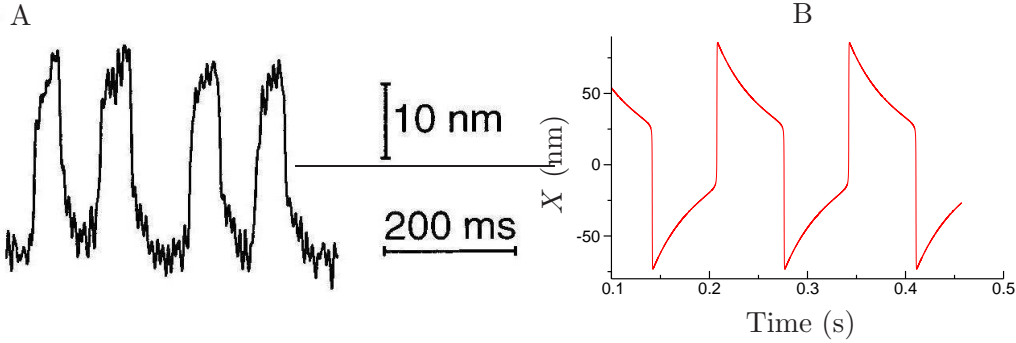


Figure 3.6: Spontaneous oscillations of a hair bundle, experiment and numerical simulation. A, spontaneous oscillations of the tip of a hair-bundle of the bullfrog’s sacculus. Taken from [81]. B, numerical simulations for our system eqs. 2.30-2.32 under the assumption of fixed motor position and calcium-dependent x_{GS} . Note the dissimilar shape of the oscillations. Parameters are given in column J of table B.1 in appendix B.

is faster than the motor-dynamics, the opening of the channels via the shortening of the rest-length happens rapidly, exploiting the linear unstable state, without changing the motor-position. This rapid part of the oscillation is accompanied by a rapid movement of the bundle in the negative direction and the opening of the channels. After this rapid movement, the situation is characterized by high tension in the gating-springs, high $[Ca^{2+}]$, high open probability and low rest-length of the gating-springs. Now, the tension of the gating-springs will be strong enough to pull the motors back and down the stereocilium. This movement continues, until the tension relaxes to moderate values, so that the channels begin to close again, reducing the $[Ca^{2+}]$, and increasing the rest-length of the tip-links. This slow phase is accompanied by the bundle moving in the positive direction, because of the reduced tension in the tip links. When the system once again encounters the region of linear instability of the calcium-equation, the rest-length grows rapidly, which reduces the tension and is accompanied by a rapid movement of the bundle in the positive direction. After this rapid phase of the oscillation, the cycle starts again.

Note that this mechanism is not an analog of the oscillations mediated by calcium-induced channel reclosure, as proposed by [14], in which an increase of $[Ca^{2+}]$ directly leads to a closure of the channels, thereby pulling the bundle in the negative direction and reducing the open probability. Here, the increase in $[Ca^{2+}]$ mediates an increase of tension in the tip-links, pulling the bundle in the negative direction while opening the channels. As explained in chapter 6, this kind of behavior is not the one observed in most experiments using step-displacements: the jump of the bundle in the negative direction is accompanied by the closure of channels, not their opening.

3.2.4 Collective motor oscillations

All the mechanisms of oscillation discussed above are based on a linear force-velocity curve, eq. 2.20, in combination with a calcium-feedback which modifies the motor activity or other parameters. This approach is of course just a first approximation to the complex system represented by the approximately 3000 motors distributed on 50 insertional plaques in the hair-bundle.

Nonlinearities in the force-velocity relations of myosin motors have been observed experimentally [91]. The two-state model of molecular motors [57] is an example of a theory of molecular motors resulting in nonlinear force-velocity curves.

This theory assumes that the periodicity of the filaments or microtubules, on which the motors are running, is translated into a periodical energy-landscape. It is furthermore assumed, that motors can be in either one of two states: attached to the filament, and therefore under the influence of this potential, or detached from the filament, a state with constant energy. Transitions from one state to another are possible, and transition rates are a function which displays the same periodicity which show the filaments. When observing an infinite number of motors, strictly coupled to each other, it can be shown that the force-velocity relation of the motor-complex exhibits nonlinearities and even can display a region of negative slope, allowing motors to show bidirectionality: for a given external force, the collection of motors can assume either of two velocities of different signs [57].

Fig. 3.7 shows a schematic plot of such a nonlinear force-velocity relation, and numerical simulations with a nonlinear force-velocity curve explained below. Both the upper and lower branch of velocities correspond to stable fixed points, whereas the portion of the curve with negative slope corresponds to unstable fixed points. The curve need not be symmetrical. Bidirectional motion of microtubules interacting with mutants of Ncd, a kinesin-related molecular motor of *Drosophila*, has been observed experimentally [39]:

If the collection of molecular motors are coupled to an elastic element, the ensemble of motors can undergo spontaneous oscillations [55, 12, 4]. An oscillation cycle of the motors corresponds to an excursion around the negative slope of the force-velocity curve depicted in fig. 3.7 on the stable branches, if these branches correspond to velocities with opposite sign.

In order to use a nonlinear force-velocity relation for the molecular motors in our model, we can start with eq. 2.20, but this time using an additional third-order term, so that we can provide the region of negative friction which can be seen in fig. 3.7.

This leads to

$$f_l = \xi_a \dot{x}_a + \xi_{a,3} \dot{x}_a^3 + f_0 \quad , \quad (3.37)$$

with a linear friction coefficient ξ_a which can now become negative and a stabilizing positive cubic coefficient $\xi_{a,3}$. While 2.20 presented a bijective map between the

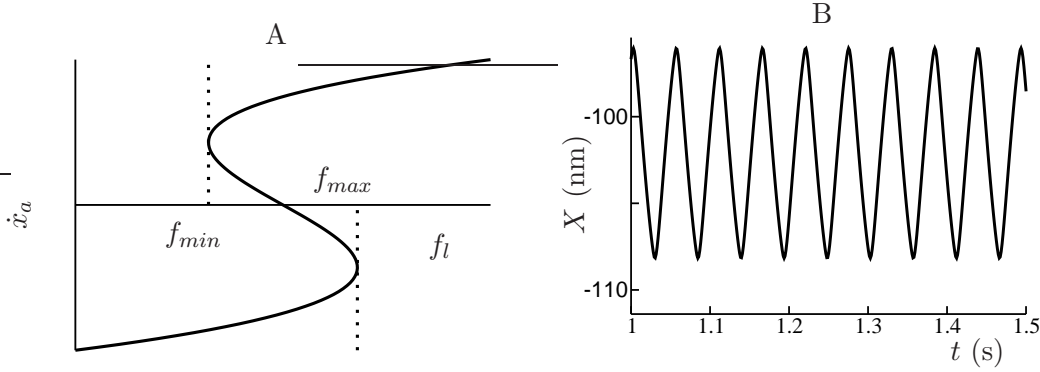


Figure 3.7: Nonlinear force-velocity curve and numerical simulations for the model of the hair-bundle. A, schematic view of a nonlinear force-velocity curve. For a given force (dotted line) three different velocities are possible, but only the extremal positions are stable. Oscillations for a collection of collective motors coupled to a spring can be seen as follows: We start at $f_l < f_{min}$, on the bottom branch. $\dot{x}_a < 0$, the system increases the tension of the spring while moving in the negative direction. Therefore, we are moving up the bottom branch, until we reach $f_l > f_{max}$. Now, the only stable solution is situated on the top branch, and the motors change the sign of the velocity, moving in the opposite direction now, reducing the tension of the spring. We are therefore moving down the top branch, until we reach $f_l < f_{min}$. Now, the only solution is situated on the bottom branch, and the cycle begins once again. This leads to a sawtooth-like movement of the molecular motors. B, numerical simulations for the model eqs. 2.30 -2.32, but with a nonlinear force-velocity curve as explained in the text. Numerical simulations are done with the parameters listed in column K of table B.1 in appendix B.

velocity and the external force, we could ignore inertial terms in the formulation of eq. 2.31, assuming that the velocity of the motors relaxes very rapidly to the value given by the force-velocity curve. As we are now in the presence of a surjective map, with two values for the velocity for a given external force, the simplest approach is to add the inertial term to the formulation of the model. We still assume that the velocity relaxes very rapidly towards the corresponding stable branch, and therefore the value of the inertial term Γ is not important in the framework of this model. It assures only the relaxation of the velocity towards a stable branch upon change of the external force.

Reformulation of 2.31 therefore leads to:

$$\Gamma \ddot{X} = -\lambda_a V_a - \lambda_{a,3} V_a^3 + K_{GS}(X - X_a - DP_o) - K_E(X_a - X_E) - F_{max} + \frac{\gamma f_{max} S}{C_M} C \quad (3.38)$$

$$\dot{X}_a = V_a \quad . \quad (3.39)$$

with $\lambda_{a,3} = \xi_{a,3} \gamma^4 N$. This additional equation, does not change the equation for the stationary states.

In the limit of $\lambda \rightarrow 0$ and $\tau \rightarrow 0$, we can now write the simplified system (eqs. 3.1 - 3.2) as:

$$F_A = \frac{K_{GP}\lambda_a}{K_{GP} + K_{SP}}V_a \quad (3.40)$$

$$k = 0 \quad (3.41)$$

$$\bar{k} = \frac{K_{PP} + K_{SP}\gamma f_{\max}SP'_o}{K_{GP} + K_{SP}} \quad (3.42)$$

$$\beta = \frac{\Gamma}{\lambda_a} \quad (3.43)$$

$$\lambda_{\text{eff}} = \lambda_a \quad (3.44)$$

$$\lambda_{\text{eff}} \frac{dX(t)}{dt} = -kX(t) + F_A(t) \quad (3.45)$$

$$\beta \frac{dF_A(t)}{dt} = -\bar{k}X(t) - F_A(t) + \frac{K_{GP}\lambda_a(K_{GP} + \gamma f_{\max}SP'_o)}{(K_{GP} + K_{SP})^2\lambda_a\tau} f(t) \quad (3.46)$$

Note that the definition of the the friction constant $\lambda_{\text{eff}} \rightarrow \lambda_a$ is an arbitrary choice, because no external force is coupling to X . Note also that \dot{X} does not couple directly to itself, but only via the interaction with F_A .

The stability of the system is given by the sign of λ_a ; negative values correspond to an oscillating regime with

$$\omega_c = \sqrt{\frac{K_{PP} + K_{SP}\gamma f_{\max}SP'_o}{(K_{GP} + K_{SP})\Gamma}} \quad (3.47)$$

The frequency of the spontaneous oscillation depicted in fig. 3.7 B, which is far away from the Hopf bifurcation, is determined by the speed of the molecular motor on the stable branches of the system. Note the difference of the shape of the oscillations in comparison with fig. 1.9. This mechanism of oscillation, due to its very different shape of oscillation, cannot be suspected to play a role in the experimentally observed low-frequency oscillations of the bullfrog's sacculus. However, for hair-bundles sensitive to higher frequencies, this mechanism might be of importance [12].

3.2.5 Conclusion

We have presented several mechanisms of oscillations, some of which showing very similar shapes of oscillations as compared to experimentally observed oscillations. In particular, the oscillating mechanism exploiting a regime of negative stiffness of the displacement-force yields both amplitudes and frequencies close to the experimentally observed oscillations of hair-bundles from the bullfrog's sacculus. This oscillation mechanism relies on a calcium-dependent motor activity, which periodically shifts the bundle into regions of negative stiffness. From all the analyzed

oscillation mechanisms, this was the only one to present low-frequency oscillations similar to experimentally observed ones, for parameter values close to the ones which can be obtained from experiments.

Another oscillation mechanism, which also depends on regions of negative stiffness, yields similar shapes of oscillations, too. This mechanism depends on a calcium-dependent rest-length of the gating spring, and on a fixed motor-position (see subsection 3.2.2, $x_{GS}(C)$). Although the shape of the oscillations is similar to the experimentally observed ones, parameter values have to be chosen which do not agree with experimental observations in order to achieve frequencies of the order of 10 Hz, as observed in experiments ($\tau \gg 1\text{ms}$). However, it might be of some importance for hair-bundles sensitive to higher frequencies.

Two other mechanisms of oscillation have been analyzed, one depending on a nonlinear force-velocity curve characterizing the molecular motors, the other one on a linear instability in the calcium-equation. These oscillations do not display the same features as those observed in experiments. However, for hair-bundles sensitive to higher frequencies than the one observed in the sacculus of the bullfrog, they might be of importance.

Chapter 4

Generic properties of critical oscillators

As discussed in the introduction, many of the nonlinear properties of the hair-bundle are displayed by a system close to a Hopf bifurcation. In this chapter, we will study the generic properties of a system close to a Hopf bifurcation. We will especially focus on the linear and nonlinear responses of such a system to sinusoidal stimuli. At the end of the chapter, we will discuss the behavior of the system in the presence of noise.

4.1 Hopf bifurcation

In general, we are interested in the real response $X(t)$ of a nonlinear system in response to a real, periodic stimulus force $F(t)$. If there is only one frequency ω_f present in the system, we can write these variables using the Fourier expansions [13]:

$$F(t) = \sum_{n=-\infty}^{n=\infty} F_n e^{-in\omega_f t} \quad (4.1)$$

$$X(t) = \sum_{n=-\infty}^{n=\infty} X_n e^{-in\omega_f t} \quad . \quad (4.2)$$

Using this expansion means that we ignore all transient phenomena, focusing only on the limit cycle solution. We can express the Fourier amplitudes F_n as a systematic expansion of the Fourier amplitudes X_n [13]:

$$F_i = A_i^{(1)} X_i + A_{ij}^{(2)} X_{i+j} X_{-j} + A_{ikl}^{(3)} X_{i+k+l} X_{-k} X_{-l} + O(X^4) \quad . \quad (4.3)$$

Consider this system in the absence of an external force, $F_i = 0$. Inspection of

eq. 4.3 for $i = 2$ reveals that $X_2 \propto X_1^2$, if we consider the expansion up to third order. This allows us to write [13]:

$$0 = A(\omega_f, \theta)\widehat{X} + B\left|\widehat{X}\right|^2\widehat{X} + O\left(\left|\widehat{X}\right|^5\right) \quad (4.4)$$

where $\widehat{X} = X_1$, see also eq. 1.2. In general, the complex coefficients A and B depend both on the frequency ω_f and a control parameter which we denote by θ . A Hopf bifurcation occurs if the linear coefficient vanishes, $A(\omega_c, \theta_c) = 0$. Indeed, spontaneous oscillations exist, if \widehat{X} satisfies $\left|\widehat{X}\right|^2 = -A/B$. At the bifurcation point, $A/B = 0$, and the amplitude of spontaneous oscillations vanishes. For A/B real and negative, spontaneous oscillations of finite amplitude exist [13]. In the vicinity of the bifurcation, we propose to develop the coefficient A to linear order [13]:

$$A(\omega_f, \theta) = a(\omega_f - \omega_c) + b(\theta - \theta_c) \quad . \quad (4.5)$$

In the presence of a sinusoidal stimulus $F(t) = \widehat{F}e^{-i\omega_f t} + \widehat{F}^*e^{i\omega_f t}$, eq. 4.4 becomes eq. 1.2, and we can now discuss the connection between the latter equation and eq. 1.1. The complex variable Z is in general a nonlinear function of the displacement X . Close to the bifurcation,

$$Z \simeq \widehat{X}e^{-i\omega t} \quad . \quad (4.6)$$

If we focus on the limit cycle solutions, neglecting transient relaxation phenomena, $\frac{d}{dt}Z \simeq -i\omega_f\widehat{X}e^{-i\omega_f t}$. Inserting eq. 4.5 and eq. 4.6 into eq. 1.2 and comparison to the normal form eq. 1.1 with an additional external stimulus term $f(t)$, which reads:

$$\frac{d}{dt}Z = -(r + i\omega_0)Z - (u + iu_i)|Z|^2Z + f(t) \quad , \quad (4.7)$$

can be used to obtain the relations

$$r = \Im\left(\frac{b}{a}\right)(\theta - \theta_c) \quad (4.8)$$

$$\omega_0 = \omega_c - \Re\left(\frac{b}{a}\right)(\theta - \theta_c) \quad (4.9)$$

$$f = -\frac{i}{a}\widehat{F}e^{-i\omega_f t} \quad (4.10)$$

$$u + iu_i = i\frac{B}{a} \quad , \quad (4.11)$$

where $\Im(z)$ and $\Re(z)$ denote the imaginary and the real part of a complex value z , respectively. In the following, we will discuss the response of a system

close to the Hopf bifurcation, eq. 1.2, under the influence of a periodic stimulus force. We define the sensitivity of the system at the stimulus frequency as:

$$\tilde{\chi}(\omega = \omega_f) = \frac{\widehat{X}}{\widehat{F}} \quad . \quad (4.12)$$

For small forces F , the linear term $A(\omega_f, \theta)\widehat{X}$ of eq. 1.2 dominates and the sensitivity becomes the linear response function: $\chi_0 = \lim_{F \rightarrow 0} \chi$. In the linear regime, the sensitivity χ does not depend on the external force and the displacement $X(t)$ can be written as

$$X(t) \simeq \int_{-\infty}^t \chi_0(t-t')F(t')dt' \quad . \quad (4.13)$$

In general, we will have to distinguish if the system is in an oscillating state, $r < 0$, or in a quiescent state, $r > 0$. We will see that both cases lead to fundamentally different response functions.

4.2 Response of stable states

On the quiescent side of the bifurcation, all eigenvalues have negative real parts. The only frequency present in the system therefore is the driving frequency ω of the external stimulus and higher harmonics. We can therefore use eq. 1.2 in order to deduce the linear response function in the vicinity of ω_c and θ_c on the quiescent side of the bifurcation. Because $\widehat{F} = F_1$ and $\widehat{X} = X_1$ correspond to the Fourier amplitudes of frequency ω , eq. 1.2 in connection with 4.5 describes the linear response function at the frequency ω in the vicinity of the characteristic frequency ω_c :

$$\tilde{\chi}_0^{-1}(\omega) \simeq a(\omega - \omega_c) + b(\theta - \theta_c) \quad . \quad (4.14)$$

For a system displaying the characteristic frequency ω_c , the Fourier components around both ω_c and $-\omega_c$ are of interest. By taking the complex conjugate of eq. 1.2, we determine the linear response function for frequencies close to $-\omega_c$:

$$F_{-1} \simeq A^*(\omega, \theta)X_{-1} \quad . \quad (4.15)$$

Here, we have used the fact that both $F(t)$ and $X(t)$ are real, which implies that $F_{-1} = \widehat{F}^*$ and $X_{-1} = \widehat{X}^*$. Eq. 4.15 therefore determines the response function $\tilde{\chi}_0$ for the frequency $-\omega$:

$$\tilde{\chi}_0^{-1}(-\omega) \simeq a^*(\omega - \omega_c) + b^*(\theta - \theta_c) \quad . \quad (4.16)$$

The linear response function concerning the force $F(t) = \widehat{F}e^{-i\omega t} + \widehat{F}^*e^{i\omega t}$ is given by the linear superposition of the two expressions 4.14 and 4.16:

$$\tilde{\chi}_0(\omega) \simeq \frac{1}{a(\omega - \omega_c) + b(\theta - \theta_c)} + \frac{1}{a^*(-\omega - \omega_c) + b^*(\theta - \theta_c)} \quad . \quad (4.17)$$

This expression now satisfies $\tilde{\chi}_0(\omega) = \tilde{\chi}_0^*(-\omega)$, as is mandatory for the real function $\chi_0(t)$, and in the vicinity of the characteristic frequencies $\pm\omega_c$ its value is close to the expressions given in in eqs. 4.14 and 4.16.

We rewrite this expression as

$$\tilde{\chi}_0(\omega) \simeq \frac{1}{2} \left(\frac{e^{-i\alpha}}{i\Lambda(\omega_0 - \omega) + K} + \frac{e^{+i\alpha}}{-i\Lambda(\omega_0 + \omega) + K} \right), \quad (4.18)$$

where ω_0 is given by eq. 4.9, $\Lambda = |a|/2$, $K = \Lambda \Im(b/a)(\theta - \theta_c)$ and $e^{i\alpha} = ia/|a|$. Note that this expression also describes the linear response function of the linear system eqs. 3.1 - 3.2 [81]¹. The phase α describes the phase lag of the velocity of displacement with respect to the stimulus, see eq. 4.7 and eq. 4.10. Fig. 5.1 shows such a response function for an experiment conducted on a hair-bundle of the sacculus of the bullfrog. The experimental data could well be fitted with eq. 4.18 (red line).

The phase factor α also determines the shape of the response-function. For example, $\alpha = 0$ results in $\tilde{\chi}_0(\omega)$ having a positive real part for all frequencies, whereas the imaginary part is negative for $\omega < \sqrt{\omega_0^2 - K^2/\Lambda^2}$, and positive otherwise. The parameters Λ and K can be viewed as effective friction and stiffness coefficients, respectively.

Nonlinear response As long as $A \neq 0$, i. e. as long as the system is not exactly at the bifurcation point, there is always a regime of linear response for small enough stimuli, the linear term of eq. 1.2 being dominant for $|\hat{F}|^2 \ll |A|^3/|B|$. For larger stimuli, $|\hat{F}|^2 \gg |A|^3/|B|$, the nonlinear term is dominant, leading to the compressive nonlinearity described by $|\hat{X}| = |B|^{-1/3}|\hat{F}|^{1/3}$, see eq. 1.3. Therefore, the sensitivity $\tilde{\chi}$ scales as

$$\tilde{\chi}(\omega) \propto |\hat{F}|^{-2/3} \quad (4.19)$$

in the nonlinear regime.

Exactly at the bifurcation point, the linear term vanishes $A = 0$, and the nonlinear behavior eq. 4.19 is true even for vanishing stimuli amplitudes $|\hat{F}| \rightarrow 0$. The shape of the response function in the nonlinear regime is no more determined by the linear expression eq. 4.18, but by a combination of the parameters A , B and higher order terms.

¹Close to the Hopf bifurcation, the eigenvalues $\mu_{1,2}$ of this system are complex conjugated and can be written as $\mu_1 = -r - i\omega_0$, where $r = (k/\lambda_{eff} + 1/\beta)/2$ and $\omega_0 = \sqrt{(\bar{k}/(\lambda_{eff}\beta) - (k/\lambda_{eff} - 1/\beta)^2/4)}$. The parameters are $\Lambda = \lambda_{eff}/(1 + ((k/\lambda_{eff} - 1/\beta)/(2\omega_0))^2)$, $K = \Lambda r$ and α is the phase of the expression $\Lambda e^{i\alpha} = (1 - i(k/\lambda_{eff} - 1/\beta)/(2\omega_0))^{-1}$.

4.3 Response of oscillating states

In the case of a spontaneously oscillating state, the response function can also be defined. In the absence of a stimulus force, the oscillatory state exhibits spontaneous periodic motion with angular frequency ω_s :

$$X(t) = \sum_{n=-\infty}^{n=\infty} X_n e^{-in\omega_s t} \quad . \quad (4.20)$$

In the presence of the stimulus of angular frequency ω_f , the displacement contains both the Fourier components of the stimulus and the Fourier components of the spontaneous oscillations:

$$X(t) = \sum_{nm} X_{nm} e^{-i(n\omega_f t + m\omega_s t)} \quad . \quad (4.21)$$

The response at the frequency of stimulation is characterized by the amplitude $\widehat{X}_f = X_{10}$, whereas the amplitude of spontaneous oscillations is dominated by $\widehat{X}_s = X_{01}$. The sensitivity of this system for $\omega_f \neq \omega_s$ can be defined as

$$\widetilde{\chi}(\omega = \omega_f) = \frac{\widehat{X}_f}{\widehat{F}} \quad . \quad (4.22)$$

We calculated this sensitivity in the linear regime for our model eqs. 2.30-2.32. The system displayed spontaneous oscillations of angular frequency $\omega_s/(2\pi) = 7.92$ Hz (see fig. 4.1 A). When stimulated with a sinusoidal stimulus close to this frequency, the linear response diverged and showed the behavior:

$$|\widetilde{\chi}(\omega)| \sim \frac{1}{|\omega - \omega_0|} \quad , \quad (4.23)$$

as can be seen in the log-log plot depicted in fig. 4.1 B. The red line corresponds to a slope -1.

We can attempt to explain this behavior in the following way. By analogy with eq. 4.3 and eq. 1.2, we can write:

$$\widehat{F} = A(\omega_f)\widehat{X}_f + B(\omega_f)\left|\widehat{X}_f\right|^2\widehat{X}_f + \overline{B}(\omega_s, \omega_f)\left|\widehat{X}_s\right|^2\widehat{X}_f \quad (4.24)$$

$$0 = A(\omega_s)\widehat{X}_s + B(\omega_s)\left|\widehat{X}_s\right|^2\widehat{X}_s + \overline{B}(\omega_f, \omega_s)\left|\widehat{X}_f\right|^2\widehat{X}_s \quad . \quad (4.25)$$

Using eq. 4.25, we find:

$$\left|\widehat{X}_s\right|^2 = -\frac{A(\omega_s) + \overline{B}(\omega_f, \omega_s)\left|\widehat{X}_f\right|^2}{B(\omega_s)} \quad (4.26)$$

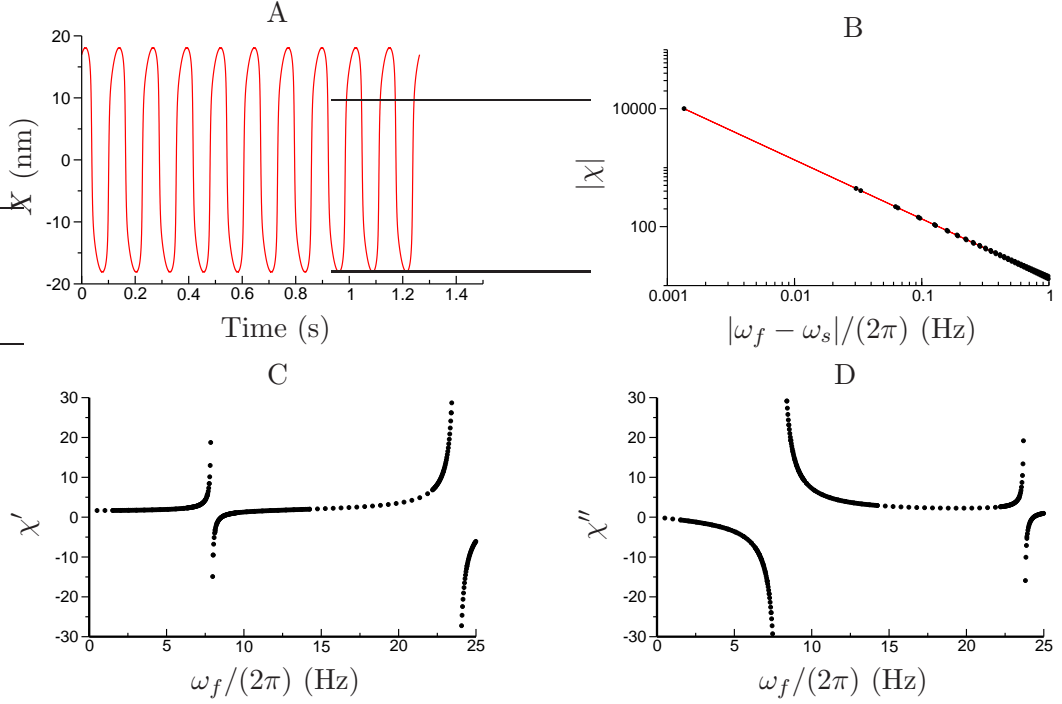


Figure 4.1: Numerical simulation showing spontaneous oscillations of a hair bundle and its linear response function. A, spontaneous oscillations are displayed at $\omega_s/(2\pi) = 7.92\text{Hz}$. B, log-log plot of the modulus of the linear response function $\tilde{\chi}_0$ in dependence of the modulus of the frequency mismatch between stimulus frequency ω_f and frequency of spontaneous oscillations, $\omega_s/(2\pi)$. C, real part of the linear response function. D, imaginary part of the linear response function. The model is defined by eqs. 2.30 - 2.32. Parameters used are those given in column L of table B.2 in appendix B.

Inserting this expression in eq. 4.24 allows us to calculate the effective linear coefficient $\hat{F} \simeq A_{eff}(\omega_s, \omega_f) \hat{X}_f$ as:

$$A_{eff}(\omega_s, \omega_f) = A(\omega_f) - \frac{\overline{B}(\omega_s, \omega_f) A(\omega_s)}{B(\omega_s)} . \quad (4.27)$$

Assuming that $\overline{B}/B = 1$ for $\omega_f \rightarrow \omega_s$, A_{eff} vanishes for $\omega_f = \omega_s$, and we recover the behavior which has been found in the numerical simulations. In the vicinity of $\omega_f \simeq \omega_s$, we can then write A_{eff} in terms of a systematic expansion in powers of $\omega_f - \omega_s$. For values of ω_f close enough to ω_s , the linear term is dominant and the linear response function diverges according to eq. 4.23.

The linear response function $\tilde{\chi}_0(\omega) = \tilde{\chi}'_0(\omega) + i\tilde{\chi}''_0(\omega)$, where $\tilde{\chi}'_0$ and $\tilde{\chi}''_0$ denote the real and imaginary part respectively, exhibits a sharply localized, singular behavior at the oscillation frequency (Fig. 4.1 C and D). Such a response function differs qualitatively from those measured experimentally in the bullfrog's sacculus [81], see fig. 5.1. There, the linear response remains finite and is of significant magnitude over a relatively large range of frequencies.

4.4 Response of noisy oscillators

A complex physical system consists of a large number of degrees of freedom. The effect of a large number of rapidly changing degrees of freedom can sometimes be captured by introducing fluctuation terms and the use of Langevin equations [61].

In the case of the Hopf bifurcation, a simple way to introduce fluctuations is to write the normal form eq. 4.7 with an additional noise term:

$$\frac{d}{dt}Z = -(r + i\omega_0)Z - (u + iu_i)|Z|^2Z + f(t) + \xi(t) \quad , \quad (4.28)$$

where $\xi(t)$ denotes a stochastic process. As the normal form is characterized by the condition of phase invariance, the noise term $\xi(t)$ must also satisfy phase invariance. A simple choice is given by:

$$\langle \xi \rangle = 0 \quad (4.29)$$

$$\langle \xi(t)\xi(t') \rangle = 0 \quad (4.30)$$

$$\langle \xi(t)\xi^*(t') \rangle = 4I\delta(t - t') \quad , \quad (4.31)$$

where I describes the intensity of the noise.

We are interested in the displacement variable $X(t)$, which can be viewed as proportional to the real part of Z in first approximation. For an oscillating system, the Fourier spectrum is of special interest in order to characterize the system's response and the spontaneous oscillations. In a noisy system, interesting quantities are the autocorrelation function $C_0(t' - t) = \langle X(t)X(t') \rangle$ and the spectral density $\tilde{C}_0(\omega) = |\tilde{X}(\omega)|^2$ (see ref. [103]).

The noiseless system's spectral decomposition is characterized by a set of Fourier amplitudes at discrete frequencies $n\omega_s$, with $n \in \mathbb{Z}$. The effect of the noise leads to a loss in phase coherence of these oscillations, "smearing" out the formerly discrete peaks. Fig. 4.2 shows the discrete peaks of the Fourier spectrum of a spontaneously oscillating system, and the spectral density of the same system with the addition of a noise term. The peak at $\omega = \omega_s$ widens, and its position shifts to a higher frequency while the peaks representing higher harmonics completely disappear.

In the presence of noise, the critical point characterized by the appearance of discrete peaks in the Fourier spectrum no longer exists. The system's spontaneous movements can be characterized by $C_0(0) = \langle |X|^2 \rangle$. In contrast to the noiseless system, this quantity never becomes zero, but shows a continuous variation with the control parameter, while the Hopf bifurcation of the noiseless system is characterized by a discontinuity in the relation between \hat{X} and the control parameter, see fig.4.3.

Fig. 4.3 A shows the order parameter \hat{X} for numerical simulations of a noiseless system, fig. 4.3 B shows the autocorrelation $\langle |X|^2 \rangle$ for the same system under

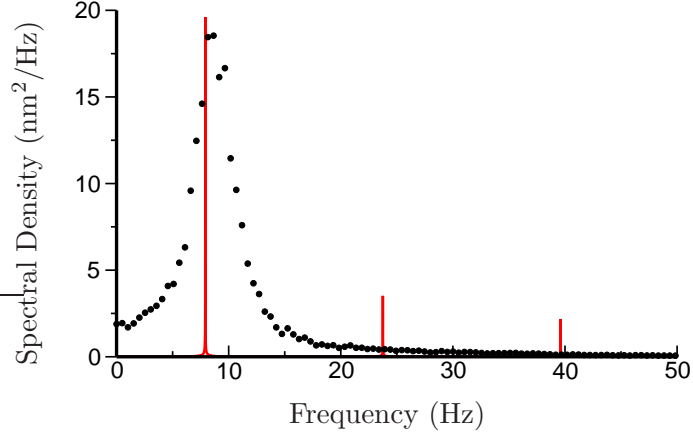


Figure 4.2: Spectral decomposition of a system with and without noise. The black dots correspond to the spectral density $\hat{C}_0(\omega)$ of a numerical simulation using eqs. 5.1-5.3. The red line is proportional to the modulus of the Fourier transform of the corresponding noiseless system. Parameter values are given in column L of table B.2 in appendix B. The description of the noise terms can be found in chapter 5.

the influence of noise. The discontinuity has disappeared, $\langle |X|^2 \rangle$ is varying continuously with the control parameter (in fig. 4.3, we used f_{\max} as the control parameter).

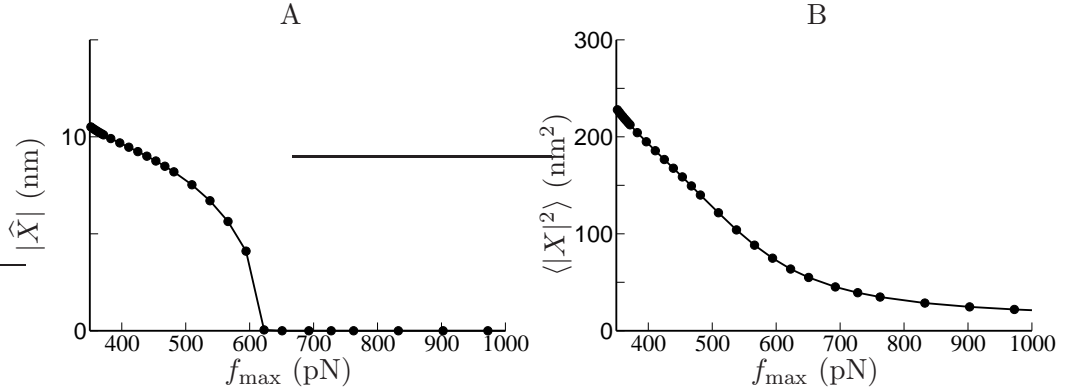


Figure 4.3: Numerical simulations showing a system undergoing a Hopf bifurcation, with and without noise. A, a noiseless system defined by eqs. 2.30-2.32. B, a noisy system using the same parameters, but with noise terms according to eqs. 5.1-5.3. All the points correspond to different points along the line $P_o = 0.5$ which can be found in the state diagram 5.2. Parameters are given in column M of table B.2 in appendix B. Noise terms have been added as explained in chapter 5.

Under the influence of a sinusoidal force $F = \hat{F}e^{-i\omega_f t} + \hat{F}^*e^{i\omega_f t}$, the spectral density will show additional discrete peaks at the frequency of stimulation and

higher harmonics:

$$\tilde{C}(\omega) = \tilde{C}_0(\omega) + 2\pi \sum_{n=-\infty}^{\infty} |X_n|^2 \delta(\omega - n\omega_f) \quad . \quad (4.32)$$

The sensitivity of the noisy system can be defined in the same way as before:

$$\tilde{\chi}(\omega) = \frac{\hat{X}}{\hat{F}} \quad , \quad (4.33)$$

where $\hat{X} = X_1$ is the Fourier amplitude of the fundamental mode.

The absence of the critical point and the absence of coherent spontaneous oscillations implies that the linear response of this system $\chi_0 = \lim_{F \rightarrow 0} \chi$ behaves effectively as the response function of stable states, discussed in section 4.2. The expression 4.18 can therefore be used to characterize the linear response of a noisy system both in regions where the noiseless system would be quiescent and in regions where the noiseless system would display spontaneous oscillations. However, the response of the noisy system will not be characterized by the same parameters in eq. 4.18. The noise renormalizes these parameters [58].

Finally, the spectral density of the system can be approximated by the generic equation [81]:

$$\tilde{C}_0(\omega) = \frac{I}{K^2 + \Lambda^2(\omega - \omega_0)^2} + \frac{I}{K^2 + \Lambda^2(\omega + \omega_0)^2} \quad . \quad (4.34)$$

The parameters in this equation are to be understood as effective parameters. For simple cases, in the vicinity of the Hopf bifurcation of the noiseless system, these parameters can be estimated from the parameters given in eq. 4.28 [58].

Chapter 5

Spontaneous movements and response of hair-bundles in the presence of fluctuations

5.1 Experimental observations: linear and nonlinear response

In the experiments conducted to calculate the response of the bundle to external sinusoidal stimuli, a flexible fiber is attached to the tip of the bundle. As the fiber adheres firmly to the bundle, this kind of measurement creates a new system: a combination of hair-bundle and attached fiber. When measuring the spontaneous oscillations of the system, it is not the hair-bundle alone which shows the oscillations, but this combined system consisting of bundle and attached fiber, with its base fixed.

Experimentally, the linear response function $\tilde{\chi}_0(\omega)$ and the sensitivity $\tilde{\chi}(\omega)$ of this combined system in response to external stimuli $F(t)$ have been studied. Fig. 1.10 shows some results for a spontaneously oscillating hair-bundle, with a typical frequency of ~ 8 Hz. The sensitivity $|\tilde{\chi}(\omega)|$ is plotted as a function of the stimulus amplitude Δ , which is the amplitude of displacements of the base of the flexible fiber. In the linear regime, the bundle's response function has also been determined. The generic response function 4.18 and spectral density 4.34 fit well the experimental data with the values $K \simeq 100\mu\text{N/m}$, $\Lambda \simeq 6.5\mu\text{Ns/m}$, $I \simeq 0.14\text{pN}^2\text{s}$ and $\alpha \simeq 0$, see fig 5.1 and 1.10.

The shape of the function, with its real part strictly positive and the imaginary part changing its sign, is determined by the phase factor $\alpha \simeq 0$. Negative values for the imaginary part also indicate negative dissipation in linear response theory [65], and therefore indicate activity. Furthermore, $\alpha = 0$ is equivalent to the diagonal entries of the matrix describing the linearized system eqs. 3.1-3.2 being equal.

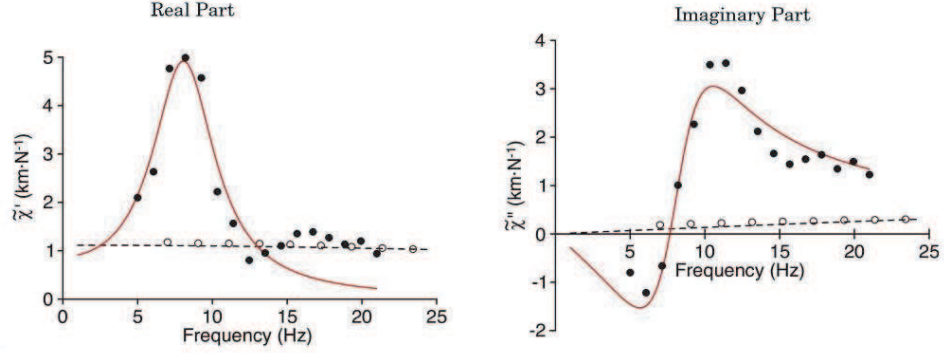


Figure 5.1: Experimentally determined linear response function $\tilde{\chi}_0(\omega)$ for 2 different hair-bundles. Full circles correspond to a hair-bundle which displayed oscillations at ~ 8 Hz, empty circles correspond to a hair-bundle which did not show spontaneous oscillations. Fits of the generic response-function 4.18 are indicated. Resulting parameter values for the oscillating bundle: $\alpha \approx 0$, $\Lambda = 6.5 \mu\text{Ns/m}$, $K = 104 \mu\text{N/m}$, $f_0 = 8\text{Hz}$, $\alpha = 0$. These values indicate similar relaxation times for active and passive elements of the hair-bundle. Taken from [81].

The diagonal entries in the matrix can be considered as time constants describing passive elements (k/λ), and active elements ($1/\beta$), respectively. The conclusion is that $\alpha = 0$ indicates a similar relaxation time for active and passive elements in the hair-bundle. Additionally, by measuring the power-density $\tilde{C}_0(\omega)$ of the spontaneous oscillations, it has been shown that this spontaneously oscillating system violates the fluctuation-dissipation theorem $\tilde{C}_0(\omega) = 2k_B T \frac{\tilde{C}_0''(\omega)}{\omega}$ [81]. The hair-bundle is therefore not in thermal equilibrium and energy can be subtracted. This system can therefore be classified as active.

We will now come to the nonlinear response of this spontaneously oscillating hair-bundle. As already explained in the introduction, its sensitivity $\tilde{\chi}$ shows three different regimes as a function of the amplitude of the external force 1.10. Two approximately linear regimes, for either large or small forces, are joined by a nonlinear regime. The slope expected for the nonlinear regime for a system close to a Hopf bifurcation, $\tilde{\chi} \propto \hat{F}^{-2/3}$ is indicated as a red line in the plot. The third-order term B of eq. 1.2 has been found to verify $|B| \simeq 1.5 \cdot 10^{12} \text{N/m}^3$ for this particular hair-bundle.

5.2 Noise sources in the hair-bundle

Spontaneous hair-bundle oscillations are noisy [81]. As shown in section 4.3, the model presented in 2.4 cannot explain the qualitative features of the experimentally observed response function. We have therefore performed numerical simulations using the model presented in 2.4, but with additional noise terms:

$$\lambda \dot{X} = -K_{GS}(X - X_a - DP_o) - K_{SP}X + F_{\text{ext}} + \eta \quad (5.1)$$

$$\lambda_a \dot{X}_a = K_{GS}(X - X_a - DP_o) - K_E(X_a - X_E) + \gamma f_{\text{max}}(-1 + S \frac{C}{C_M}) + \eta_a \quad (5.2)$$

$$\tau \dot{C} = C_0 - C + C_M P_o + \delta c \quad , \quad (5.3)$$

Noise terms η , η_a and δc in eqs. 5.1-5.3 formally take into account the effects of various sources of fluctuations that destroy the phase coherence of hair-bundle movements. The stochastic forces η and η_a act respectively on X and X_a . The consequences of these forces have been analyzed for non-oscillating hair-bundles [30]. The fluctuations δc of the Ca^{2+} concentration in the stereocilia result from stochastic transitions between open and closed states of the transduction channels [84]. Noise terms are zero on average. Their strengths are characterized by autocorrelation functions $\langle \eta(t)\eta(0) \rangle$, $\langle \eta_a(t)\eta_a(0) \rangle$ and $\langle \delta c(t)\delta c(0) \rangle$ respectively. We assume that different noise sources are uncorrelated and that noise is Gaussian.

Assuming that the motors are deactivated ($f = 0$), we first discuss thermal contributions to the noise. The noise term η in eq. 5.1 then results from Brownian motion of fluid molecules which collide with the hair-bundle and from thermal transitions between open and closed states of the transduction channels. By changing the gating-spring extension, this channel clatter generates fluctuating forces on the stereocilia. The fluctuation-dissipation theorem implies that

$$\langle \eta(t)\eta(0) \rangle = 2k_B T \lambda \delta(t) \quad . \quad (5.4)$$

The friction coefficient $\lambda = \lambda_h + \lambda_c$ results from the two contributions already mentioned: $\lambda_h \simeq 1.3 \cdot 10^{-7} \text{Ns/m}$ accounts for hydrodynamic friction, which depends on bundle geometry and fluid viscosity [23, 44], whereas λ_c results from channel clatter. The contribution λ_c can be estimated from the autocorrelation function of the force η_c that results from stochastic opening and closing of N transduction channels

$$\langle \eta_c(t)\eta_c(0) \rangle \simeq \frac{D^2 K_{\text{gs}}^2 P_o (1 - P_o)}{N} e^{-|t|/\tau_c} \quad (5.5)$$

$$\simeq \frac{D^2 K_{\text{gs}}^2 P_o (1 - P_o)}{N} 2\tau_c \delta(t) \quad . \quad (5.6)$$

This expression shows that noise is correlated in time with a correlation time given here by the characteristic dwell time τ_c of the transduction channels' open and closed states. However, channel clatter is fast compared to hair-bundle oscillations and we can focus on the low-frequency limit of friction. With

$$\langle \eta_c(t)\eta_c(0) \rangle \simeq 2k_B T \lambda_c \delta(t) \quad , \quad (5.7)$$

eq. 5.5 yields

$$\lambda_c \simeq \frac{K_{\text{gs}}^2 D^2 P_o (1 - P_o) \tau_c}{N k_B T} \quad . \quad (5.8)$$

Recent single-channel recordings indicate that $\tau_c \simeq 1\text{ms}$ [88]. Using parameter values listed in column L of table B.1 in appendix B, and $P_o = 0.5$, we find that channel clatter dominates friction and $\lambda \simeq 3 \cdot 10^{-6}\text{Ns/m}$.

The noise term η_a in eq. 5.2 describes fluctuating forces acting on the motors. In the case of deactivated motors ($f = 0$), thermal binding and unbinding of molecular motors respectively to and from actin filaments generates friction with a coefficient $\lambda_0 \simeq \gamma^2 N_a p k \tau_1$ [66]. Here, $p = \tau_1 / (\tau_1 + \tau_2)$ is the probability for a motor to be attached to an actin filament, where τ_1 and τ_2 denote the lifetimes of the attached and detached states respectively, and k is the stiffness of a single motor. Using $p \simeq 0.05$, $k \simeq 500\mu\text{N/m}$ and $\tau_1 \simeq 10\text{ms}$, we estimate $\lambda_0 \simeq 1.5 \cdot 10^{-5}\text{Ns/m}$. The strength of the thermal contribution η_0 to η_a is

$$\langle \eta_0(t) \eta_0(0) \rangle \simeq 2k_B T \lambda_0 \delta(t) \quad . \quad (5.9)$$

We now turn to the more interesting situation of active motors ($f \neq 0$). Measurements of the initial adaptation rate as a function of the magnitude of step stimuli [37] imply that $\lambda_a \simeq 1.3 \cdot 10^{-5}\text{Ns/m}$, in agreement with the value of the friction coefficient λ_0 estimated above for deactivated motors. We thus neglect the effect of motor activity on motor friction. However, the stochastic activity of motors generates an active contribution η_m to η_a with

$$\langle \eta_m(t) \eta_m(0) \rangle \simeq \gamma^2 N_a p (1-p) f^2 e^{-|t|/\tau_a} \quad (5.10)$$

$$\simeq \gamma^2 N_a p (1-p) f^2 2\tau_a \delta(t) \quad . \quad (5.11)$$

Here we have assumed that motors fluctuate independently and that relevant timescales for a hair-bundle oscillation are longer than τ_a , where $\tau_a \simeq (\tau_1^{-1} \tau_2^{-1})^{-1} \simeq \tau_1$ is the characteristic time of force production by the motors. This noise strength can be described by introducing an effective temperature T_m defined by

$$\langle \eta_m(t) \eta_m(0) \rangle \simeq 2k_B T_m \lambda_a \delta(t) \quad . \quad (5.12)$$

With $f \simeq 1\text{pN}$, $\tau_a \simeq 10\text{ms}$ and $p \simeq 0.05$, we find

$$\begin{aligned} T_m/T &\simeq \frac{N_a \gamma^2 p (1-p) f^2 \tau_a}{k_B T \lambda_a} \\ &\simeq 0.5 \quad . \end{aligned} \quad (5.13)$$

Writing

$$\langle \eta_a(t) \eta_a(0) \rangle = 2k_B T_a \lambda_a \delta(t) \quad , \quad (5.14)$$

we thus get $T_a \simeq 1.5T$.

Assuming that channel dynamics equilibrates rapidly enough, we neglect the effect of motor activity on channels' statistics. In this case, the fluctuations in eq. 5.1 remain thermal and satisfy a fluctuation-dissipation relation.

The calcium-dynamics is also subjected to fluctuations that are described by the noise term δc in eq. 5.3. In analogy to eq. 5.10, the autocorrelation function of δc is approximated by

$$\langle \delta c(t) \delta c(0) \rangle \simeq C_M^2 N^{-1} P_o (1 - P_o) e^{-|t|/\tau_c} \quad . \quad (5.15)$$

We can assess the significance of these fluctuations in the limit where C relaxes instantaneously. The system is in turn reduced to eqs. 5.1 and 5.2, with

$$C = C_0 + C_M P_o + \delta c \quad . \quad (5.16)$$

The fluctuations of the calcium-concentration can then be written as

$$\langle \delta C(t) \delta C(0) \rangle \simeq \langle \delta c(t) \delta c(0) \rangle \quad . \quad (5.17)$$

As the probability p of motor binding to actin filaments depends on the calcium-concentration, fluctuations of C result in the generation of fluctuating forces η_c by the motors. We estimate this random force as:

$$\eta_c \simeq \gamma N_a f p' \delta C \quad . \quad (5.18)$$

For times large compared to τ_c , we find:

$$\langle \eta_c(t) \eta_c(0) \rangle \simeq 2(\gamma N_a f p' C_M)^2 N^{-1} P_o (1 - P_o) \tau_c \delta(t) \quad . \quad (5.19)$$

Introducing an effective temperature T_c , with

$$\langle \eta_c(t) \eta_c(0) \rangle = 2k_B T_c \lambda_a \delta(t) \quad , \quad (5.20)$$

we find

$$\begin{aligned} T_c/T &\simeq \frac{(\gamma f_{\max} S)^2 P_o (1 - P_o) \tau_c}{N k_B T \lambda_a} \\ &\simeq 0.13 \end{aligned} \quad (5.21)$$

for $P_o = 0.5$ and parameter values from column L of table B.1 in appendix B. This suggests that fluctuations of the motor force evoked by calcium-fluctuations are below the unavoidable thermal fluctuations.

In our simulations of eqs. 5.1-5.3, we used the noise strengths

$$\langle \eta(t) \eta(0) \rangle = 2k_B T \lambda \delta(t) \quad (5.22)$$

$$\langle \eta_a(t) \eta_a(0) \rangle = 2k_B T_a \lambda_a \delta(t) \quad (5.23)$$

$$\langle \delta c(t) \delta c(0) \rangle = 2C_M^2 N^{-1} P_o (1 - P_o) \tau_c \delta(t) \quad , \quad (5.24)$$

with parameter values listed in column L of table B.1 in appendix B. Note that it is not necessary to know the value of C_M if S and f_{\max} are given.

5.3 Numerical results

We have performed numerical simulations on the system presented in eqs. 5.1-5.3 [83]. Due to the fluctuation-dissipation theorem, the friction coefficient λ is assumed to be much larger than the hydrodynamic estimates. This difference in the friction coefficient is the main difference between the state diagram fig. 3.1 and the state diagram 5.2. The state diagram, drawn with parameters which can be found in column M of table B.1 in appendix B, now presents a significantly smaller oscillating state than the one found in fig. 3.1: using the approximation for fast calcium-relaxation described in 3.2.1, stable solutions corresponding to $Tr = -k/\lambda - K_{GP}/\lambda_a - K_E/\lambda_a - \gamma f_{\max} SP'_o/\lambda_a < 0$ can now be found only for significantly lower values of S .

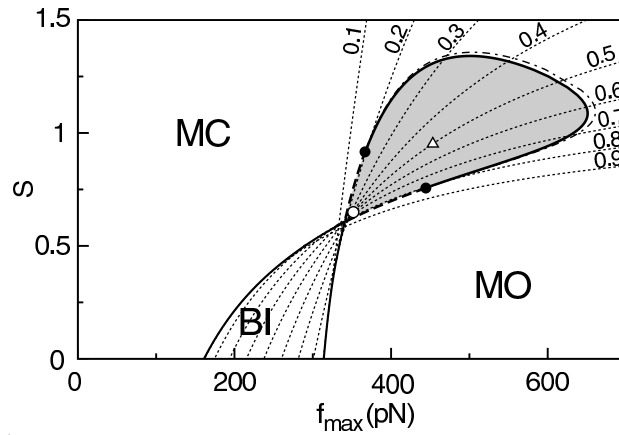


Figure 5.2: State diagram of a hair-bundle as a function of the maximal force f_{\max} and of the strength of calcium-feedback S . BI, bistable region; MO, monostable region with channels mostly open; MC, monostable region with channels mostly closed. The oscillating region is shaded. Hopf bifurcations take place along the line separating monostable states from oscillating ones. The broken line indicates subcritical Hopf bifurcations. This diagram is drawn assuming that the Calcium dynamics is very fast, $\tau = 0$. For the numerical simulations, a value of $\tau = 0.1\text{ms}$ has been used; in this case, the oscillatory region expands towards regions of larger motor forces. For $f_{\max} = 352\text{pN}$ and $S = 0.65$ with $P_o = 0.5$ (\circ), the system closely matches the behavior of a hair-bundle studied experimentally. For $f_{\max} = 439\text{pN}$ and $P_o = 0.5$ (Δ), the system displays a global maximum of sensitivity. Parameters used are listed in column M of table B.1 in appendix B.

We have performed numerical calculations on a number of points with parameter values given by column M of table B.2 in appendix B, only changing the feedback strength S and the maximal motor force f_{\max} , the rest of the parameters being fixed in the range given by experimental observations. In endolymph containing Ca^{2+} at a concentration of $250\mu\text{M}$, the open probability for which the adaptation motors reach steady state is between 0.25 and 0.5 [37, 15].

Along a line of constant open probability $P_o = 0.5$ in the state diagram (fig. 5.2), we determined the parameters in eq. 4.18 as a function of f_{\max} in the presence

of noise. For $P_o = 0.5$, the characteristic frequency of spontaneous oscillations varied between a few Hertz and about 50Hz in the range $f_{\max} = 330\text{--}800\text{pN}$ within which a peak was detected in the spectral density of spontaneous movements (fig. 5.3).

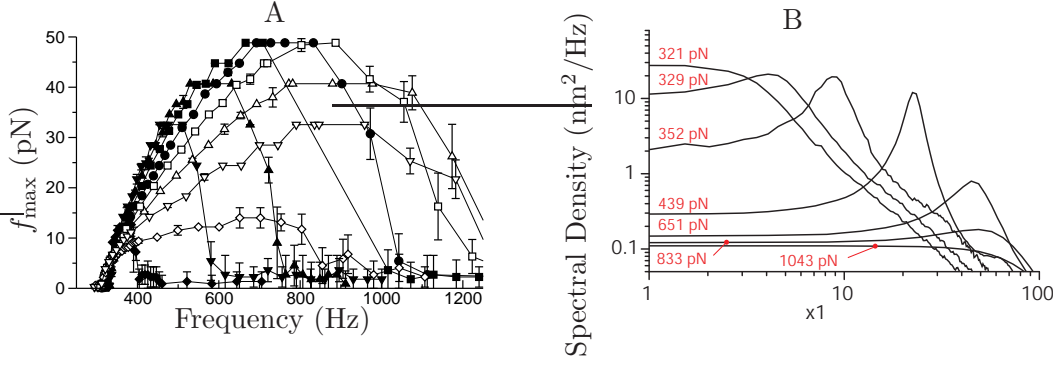


Figure 5.3: Spontaneous movements as a function of the hair-bundle's operating point. A, frequency of spontaneous oscillations for $P_o = 0.1$ (\blacklozenge), 0.2 (\blacktriangledown), 0.3 (\blacktriangle), 0.4 (\blacksquare), 0.5 (\bullet), 0.6 (\square), 0.7 (\triangle), 0.8 (∇) and 0.9 (\diamond). B, Spectral densities of spontaneous movements along the line $P_o = 0.5$ for the different values of f_{\max} indicated in red. Here and in the subsequent figures, error bars correspond to the standard deviation obtained for ten successive realizations of the simulation.

As $\alpha \simeq 0$ ensures that the linear response function has the same shape as that observed experimentally [81], we elected the value of the motor force $f_{\max} \simeq 352\text{pN}$ at which this condition was satisfied for $P_o = 0.5$ (fig. 5.2). At this operating point, the system displayed noisy spontaneous oscillations $X(t)$ that were strikingly similar to the hair-bundle oscillations observed in the bullfrog's sacculus (fig. 5.4 A, see fig. 1.9).

Their spectral density was peaked at a characteristic frequency $\nu_0 = \omega_0/2\pi = 8.7$ Hz and had a width at half the maximal value of $\delta\nu = 3.7$ Hz, corresponding to a quality factor $Q = \nu_0/\delta\nu = 2.4$ (fig. 5.4 B, see also fig.1.9). The observation that the power density goes to zero for small frequencies in fig. 1.9 is an artifact of the measurement: because the whole experimental setup shifted slowly in time, a baseline-subtraction has been applied, subtracting the mean corresponding to 0.5 seconds of measurement.

We calculated the linear response function $\tilde{\chi}_0$ as a function of frequency (fig. 5.5 A and B) and found that it agreed quantitatively with the experimental observations [81]. At the characteristic frequency of the spontaneous oscillations, the sensitivity $|\tilde{\chi}|$ of the system to mechanical stimulation exhibited the three regimes observed experimentally [80] as a function of the stimulus amplitude $|\hat{F}|$ (fig. 5.5 C): a linear regime of maximal sensitivity $|\tilde{\chi}_0| = 8.5\text{km/N}$ at $\omega = \omega_0$ for small stimuli, a compressive nonlinearity for intermediate stimuli and a linear behavior of low sensitivity for large stimuli.

The maximal sensitivity as well as the breadth of the nonlinear region were also in quantitative agreement with experiments. An important parameter that

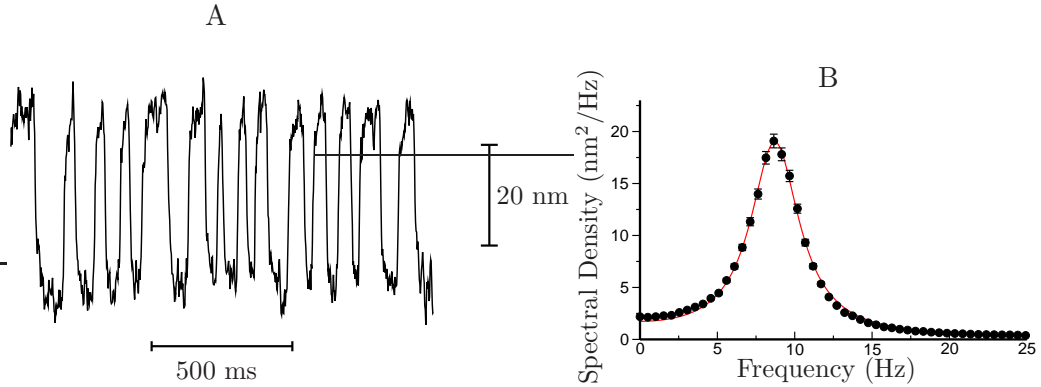


Figure 5.4: Spontaneous noisy oscillations for parameters corresponding to the operating point (\circ) in fig. 5.2. *A*, Spontaneous hair-bundle movements $X(t)$ as a function of time. This oscillation has a root-mean-squared magnitude of 15 nm. *B*, Spectral density of the movements depicted in *A*. The spectrum has been fitted (red line) by eq. 4.34 with $I = 0.105$ pN 2 s, $K = 74$ μ N/m, $\Lambda = 6.3$ μ Ns/m and $\nu_0 = 2\pi\omega_0 = 8.7$ Hz. The hair-bundle oscillation measured in [81] is strikingly similar to that simulated here, see fig. 1.9. Parameters can be found in column L of table B.1 in appendix B.

influenced the system's maximal sensitivity was the stiffness of the load to which the hair-bundle is coupled. For $f_{\max} \simeq 352$ pN, power spectra of spontaneous oscillations and response functions were not significantly affected by varying P_o in the range 0.2-0.8. Thus, agreement between simulations and experiments did not qualify a particular value of P_o .

As has been shown in *in vitro* experiments, the stiffness of the load to which the hair-bundle is coupled influences the bundle's spontaneous oscillations [78]. In these experiments, this stiffness is that of an attached glass fiber, whereas in the ear it is given by the stiffness of an ancillary structure like the otolithic membrane for the sacculus. When in our simulations the stiffness of the load was increased, the oscillation got faster and of smaller magnitude (fig. 5.6), in agreement with previous experimental observations. The spontaneous movements also became noisier, as revealed by a 70% reduction of the quality factor Q when the combined stiffness of the load and the stereociliary pivots was raised from 600 μ N/s to 1800 μ N/s. As a result, the sensitivity to small stimuli was significantly reduced, when the combined stiffness of the load and the stereociliary pivots was increased (here by 90% ,see fig. 5.6 B). The load thus impeded the ability of an oscillatory hair-bundle to amplify mechanical stimuli. Significant amplification by a single hair-bundle was achieved only when the stiffness of the load remained smaller than the maximum negative stiffness that an oscillatory hair-bundle manifests in its displacement-force relation.

Is the hair bundle's operating point optimal? To address this issue, we determined, for different open probabilities of the transduction channels, how the sensitivity to small stimuli at resonance $|\tilde{\chi}_0|$ varied with the maximal force f_{\max}

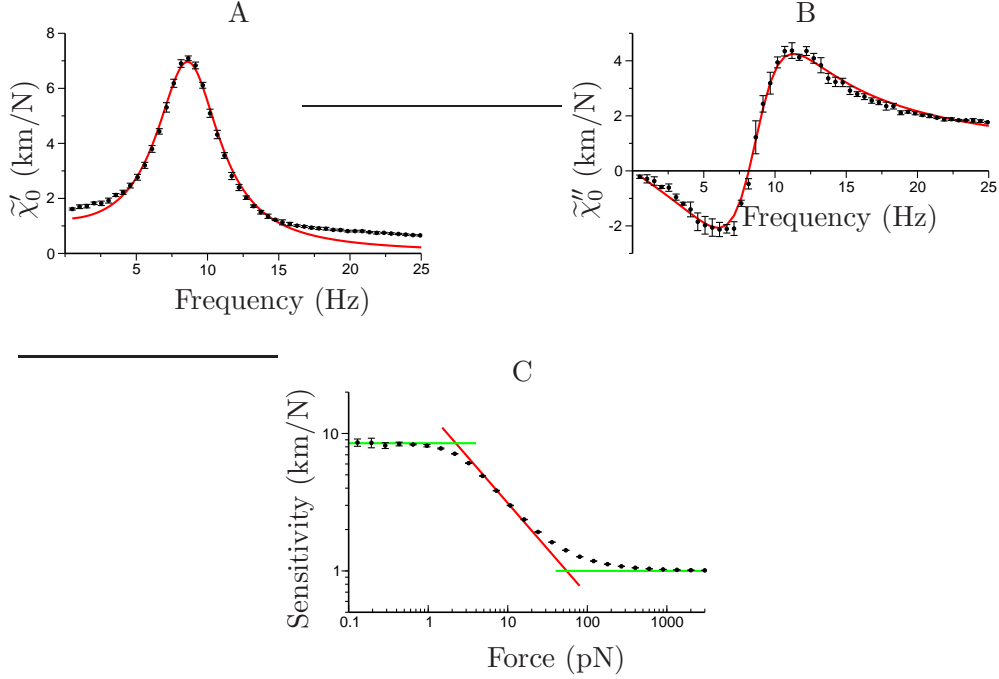


Figure 5.5: Responsiveness to sinusoidal stimulation. A, The real part $\tilde{\chi}'_0$ of the linear response function $\tilde{\chi}_0$ displays a peak near the bundle's frequency of spontaneous oscillation, and is positive everywhere. B, The imaginary part $\tilde{\chi}''_0$ changes sign at a frequency near that of the bundle's spontaneous oscillation. The external sinusoidal force has had an amplitude of 2pN. Taken from the fit (red lines) of the response function $\tilde{\chi}_0$ by eq. 4.18, we have found $\alpha \simeq 0$, $K = 74\mu\text{N/m}$, $\Lambda = 4.3\mu\text{Ns/m}$ and $\nu_0 = 2\pi\omega_0 = 8.6$ Hz, in quantitative agreement with the response function measured for an oscillatory hair bundle [81]. C, The sensitivity $|\tilde{\chi}|$ displays a nonlinear compression in a regime of intermediate forces 3 – 30pN when the magnitude of an external sinusoidal force is increased at the frequency of the spontaneous oscillations. This nonlinearity is consistent with a power law with an exponent of -2/3 (red line). A fit to the relation $\tilde{\chi}^{-1} \simeq \tilde{\chi}_0^{-1} + B|\tilde{X}|^2$ yielded the nonlinear coefficient $|B| \simeq 1.2 \cdot 10^{12}\text{N/m}^3$. For stimuli smaller than $\simeq 1\text{pN}$, the sensitivity saturates at $|\tilde{\chi}_0| \simeq 8.5\text{km/N}$ (green line). For stimuli larger than $\simeq 300\text{pN}$, the sensitivity approaches a constant, minimal value of 1km/N (green line). The parameters used in the simulation are the same as in fig.5.4.

that the motors produce (fig. 5.7). We found that this sensitivity was at the global maximum $|\tilde{\chi}_0| = 11.3\text{km/N}$ for $P_o \simeq 0.5$ and $f_{\max} \simeq 439$ pN, near the center of the oscillatory region in the state diagram (fig 5.2). At this point, the spontaneous oscillation displayed a characteristic frequency of $\nu_0 = 24.7$ Hz and a quality factor $Q = 5.4$ that was also near the global maximum (fig. 5.3 B). This point was clearly distinct from the operating point of the hair bundle (fig. 5.2). There, the hair bundle was characterized by a sensitivity to small stimuli that was 25% lower than that at the optimum.

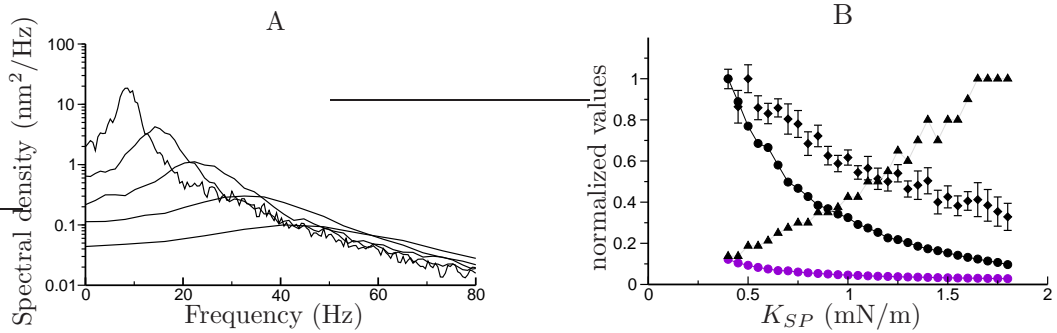


Figure 5.6: Effect of mechanical load on hair-bundle oscillations. A, Spectral density of spontaneous movements as a function of frequency for five values of the combined stiffness K_{SP} of the combined stereociliary pivots and external load. When K_{SP} has been raised from $600\mu\text{N/m}$ to $1800\mu\text{N/m}$, the peak has shifted toward regions of higher frequencies and widened. B, Some measured quantities as a function of K_{SP} . Sensitivity $|\tilde{\chi}|$ in response to strong (●) and to weak (●) stimuli, both scaled from 13.367km/N , frequency of spontaneous oscillations (\blacktriangle), scaled from 40.7Hz , and quality factor Q (\blacklozenge), scaled from 2.7 . Maximal sensitivities occur in response to weak stimuli, whereas intense stimuli result in minimal sensitivities. The frequency of spontaneous oscillations increases with the load, whereas the quality factor Q decreases. With parameter values listed in column L of table B.1 in appendix B, the bundle was characterized by a maximum negative stiffness of $-1180\mu\text{N/m}$ in its displacement-force relationship.

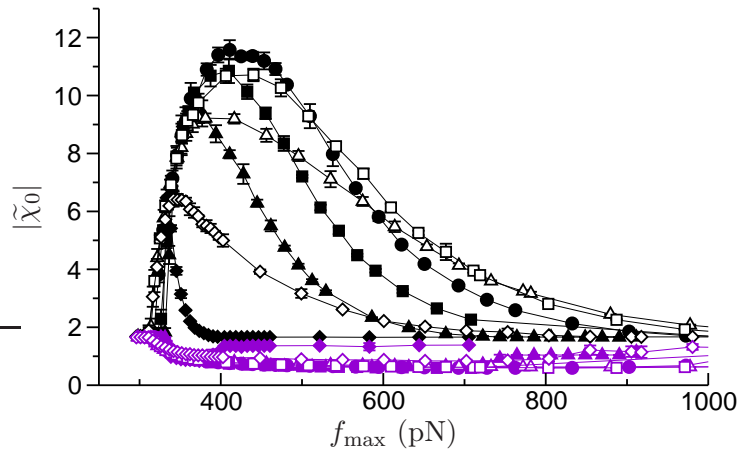


Figure 5.7: Sensitivity as a function of the hair-bundle's operating point. Maximal (black symbols) and minimal (purple symbols) sensitivity $|\tilde{\chi}|$ as a function of the maximal motor force f_{max} for $P_0 = 0.1$ (\blacklozenge), 0.3 (\blacktriangle), 0.4 (\blacksquare), 0.5 (\bullet), 0.6 (\square), 0.7 (\triangle) and 0.9 (\diamond). The sensitivity displays a global maximum for $P_0 = 0.5$ and $f_{\text{max}} \simeq 439$ pN. Responses of maximal sensitivity $\tilde{\chi}_0$ are obtained in response to small sinusoidal stimuli at the characteristic frequency of spontaneous bundle oscillations, whereas the minimal sensitivity is obtained for intense stimuli. The ratio of maximal to minimal sensitivities determines the gain of the amplificatory mechanism. Parameters can be found in column M of table B.1 in appendix B.

Chapter 6

Mechanical response to step-displacements

When bathed in an extracellular fluid containing a high external calcium-concentration ($[Ca^{2+}] \simeq 4mM$), hair-bundles rarely display spontaneous oscillations [43]. The mechanical properties of these quiescent hair-bundles have been investigated with the help of a flexible fiber, as explained in chapter 5. In this chapter, we will focus on a kind of stimulus in which the base of the fiber is moved using a step-displacement.

In this kind of experiments, the bundle's tip shows a rapid movement in the negative direction - the twitch - in response to a step-displacement in the positive direction. Two typical responses of the hair-bundle's tip are shown in fig. 6.1. This fast movement in the negative direction coincides with the reclosure of the transduction channels, which is reflected by the significant decrease of receptor current in an experimental setup which clamps the membrane potential (fig. 6.1). As explained in the introduction, the re-establishing of an open probability close to the initial one is called adaptation, because it restores the physiological properties of the bundle in its initial position. After this period of fast adaptation, the bundle relaxes more slowly (tens of milliseconds), before reaching its stationary position under the influence of the step displacement. When the bundle is deflected in the negative direction, however, no twitch is observed, and the bundle displays only slow adaptation.

Whereas the model presented in section 3.2.1 and section 5.3 has quantitatively reproduced the properties of a spontaneously oscillating hair-bundle, which have been observed consistently at low values of $[Ca^{2+}] \simeq 250\mu M$, it fails to display the features of the twitch, as will be shown below. An extension of this simple model is therefore necessary.

Experimentally, the external calcium-concentration has been shown to have an effect on several of the properties of the bundle. It affects relaxation times of adaptation [89, 37], the open probability of channels [37], the stiffness of the bundle [77], the form of the displacement-response curves [16, 15], and it might also affect

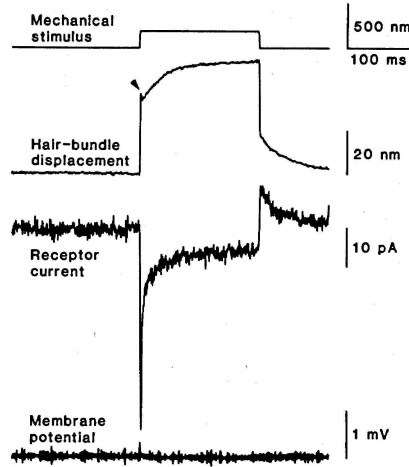


Figure 6.1: Example of the twitch. This figure displays the mechanical response of the bundle's tip under the influence of the step-like displacement of the base of a flexible fiber, which is attached to the tip of the hair-bundle. The experiment is conducted in the presence of standard saline solution, with 4 mM external $[Ca^{2+}]$. The arrow indicates a small twitch. Taken from [43].

the length of the gating swing [82] as well as the free energy difference between open and closed state of the channels (see subsection 2.4.3). Intracellular calcium-dynamics has been proposed to be at the origin of spontaneous oscillations of the hair-bundle by inducing the channels to close in the presence of high $[Ca^{2+}]$ [14].

For some of the parameters, experimental evidence indicates the quality of the calcium-dependence. Several experiments indicate that K_{GS} and D decrease in response to a higher internal calcium-concentration, while ΔG seems to increase with increasing $[Ca^{2+}]$, see for example subsection 2.4.2.

A completely different experiment supports the assumption that K_{GS} and D decrease with increasing $[Ca^{2+}]$: The spontaneous oscillations of hair-bundles from the bullfrog's sacculus decrease in amplitude and increase in frequency in the presence of increased calcium-concentration [78]. If these oscillations correspond to a trajectory around the negative stiffness in the displacement-force relation, the calcium-concentration has to influence the shape of this relation. The fact that the oscillations decrease in amplitude support the assumption that K_{GS} and D decrease in response to a higher calcium-concentration.

In this chapter, we will argue that the dependencies of some of the parameters on calcium are crucial in order to explain a phenomenon which has been observed in experiments conducted in the presence of a high external calcium-concentration.

We will begin by the analysis of the behavior of the system presented in section 3.2.1 in response to step-displacements. We will thereby introduce a method which can be applied in the investigation of the effects of step-displacements under the

assumption of calcium-dependent parameters. From all the parameters which might influence the properties of the hair-bundle, we propose to focus on the investigation of the effect of calcium-dependent D , K_{GS} , X_{GS} , and ΔG . We do not aim at a complete description of hair-bundle mechanics, explaining with one set of equations both the behavior of the bundle in an oscillating regime and in the quiescent regime in high calcium-concentrations. The dependence of a given parameter on the calcium-concentration over the range of $25\mu\text{M}$ to 4mM is probably quite complicated. In the following, we will restrict the analysis to the linear term. The value of a given parameter ζ is therefore assumed to evolve according to $\zeta(C) = \zeta' C + \zeta_0$.

To understand this phenomenon, we will first rewrite the model for the specific situation of a step experiment, where a flexible fiber of stiffness K_F undergoes a step-displacement of its base by a distance Δ . The flexible fiber, attached to the tip of the bundle, exerts on the bundle the external force

$$F_{\text{ext}} = K_F(\Delta - X) \quad . \quad (6.1)$$

Therefore, we can describe a step-displacement with a flexible fiber as the application of the constant force $K_F\Delta$ to a bundle with the combined effective stiffness $K_c = K_{SP} + K_F$. Under the influence of this external force, the system will have a new stationary value, to which it is evolving after having received the stimulus. Due to the adaptation, the open probability of this new state is close to the one before stimulation, but not exactly the same, see subsection 2.4.3. For simplicity, we ignore the difference between these two open probabilities by choosing $K_E = 0$. Using the external force eq. 6.1, eqs. 3.27 and 3.28 can be rewritten as:

$$\lambda \dot{X} = -K_{GS}(X - X_a - X_{GS} - DP_o) - K_c X + K_F \Delta \quad (6.2)$$

$$P_o = \frac{1}{1 + e^{-\frac{K_{GS}D}{Nk_B T}(X - X_{off})}} \quad , \quad (6.3)$$

where X_{off} is the offset of the displacement-force relation in the sense that $P_o = 0.5$ for $X = X_{off}$:

$$X_{off} = \frac{N\Delta G}{K_{GS}D} + X_a + X_{GS} + D/2 \quad . \quad (6.4)$$

Since the open probability in the stationary state is small, the friction coefficient λ is approximately given by the small hydrodynamic component λ_h , and the relaxation time of the hair-bundle's tip, $\sim \lambda/(K_{GS} + K_c)$, is assumed to be the fastest process in step-displacement experiments. From experiments [44], this timescale can be considered well below the millisecond. To facilitate the discussion, we introduce the displacement-force relation in the absence of an external force, see eq. 2.15:

$$F_D = -K_{GS}(X - X_a - X_{GS} - DP_o) - K_c X \quad , \quad (6.5)$$

and the short relaxation time of the hair-bundle's tip will force a rapid relaxation of the position X to the position given by $F_D = -K_F\Delta$.

The slowest timescale in the system is attributed to the motion of the molecular motors, $\sim \lambda_a/(K_{GS} + K_E)$, which is on the order of tens of milliseconds [37]. The third timescale present in the system is given by the regulation of the internal calcium-regulation, and corresponds to τ . In the following, we suppose that this relaxation time has a value of ~ 1 ms, placing it at an intermediate value between the fast relaxation of the hair-bundle's tip and the slow movements of the motors.

In this case, the rapid increase of the bundle's position X directly following the stimulation is dictated by the relaxation time of the hair-bundle's tip, which opens the Ion-channels and therefore changes the internal calcium-concentration C . The twitch might result from the displacement-force curve changing its shape or position due to the dependence of one of its parameters on this internal $[\text{Ca}^{2+}]$ [87], which would mean that the phenomenon of fast adaptation is linked to the timescale of the calcium-dynamics. Additionally, the nonlinear form of F_D can also influence the movement of the hair-bundle, as will be seen in the following. This nonlinearity is given by the strength of the gating-compliance, characterized by the term $K_{GS}DP'_o$. The displacement-force relation F_D can have a positive slope, if $K_{GS}DP'_o > K_{GS} + K_c$. Therefore, the stronger the value of $K_{GS}D/(k_B T N)$, the stronger is the gating compliance and the nonlinearity of F_D .

First, we can analyze the situation which arises when all these parameters are constants, the basic model described in 3.2.1. Note that this model displays the same shape of the oscillations as the one observed in experiments, see also subsection 3.2.2. The shift of the displacement force relation in response to a change of the motor-position X_a can be represented by the shift of the points X_{off} and $F_D(X_{off})$, given by:

$$\frac{\partial X_{off}}{\partial X_a} = 1 \quad (6.6)$$

$$\frac{\partial F_D(X_{off})}{\partial X_a} = -K_c \quad (6.7)$$

The displacement-force relation shifts therefore with a slope of $-K_c$, as has already been stated in 3.2.1. We can visualize the movement of the bundle using the displacement-force relation.

Fig. 6.2 shows the movement of the bundle in response to a step-displacement of the base of a flexible fiber. The figure represents the case of the simple model presented in 3.2.1. A numerical simulation is represented by the cyan points. Part A of the figure shows F_D calculated with a value for X_a corresponding to the stationary value of the motors before (black) and after (red) deflection. While the motors move, the curve shifts inside the corridor with the slope K_c , which is indicated by two grey lines. Intersections of these curves with the constant forces before (0) and after ($-K_F\Delta$) deflection are the stationary values of the bundle immediately before the movement of the fiber, and at the end of the deflection.

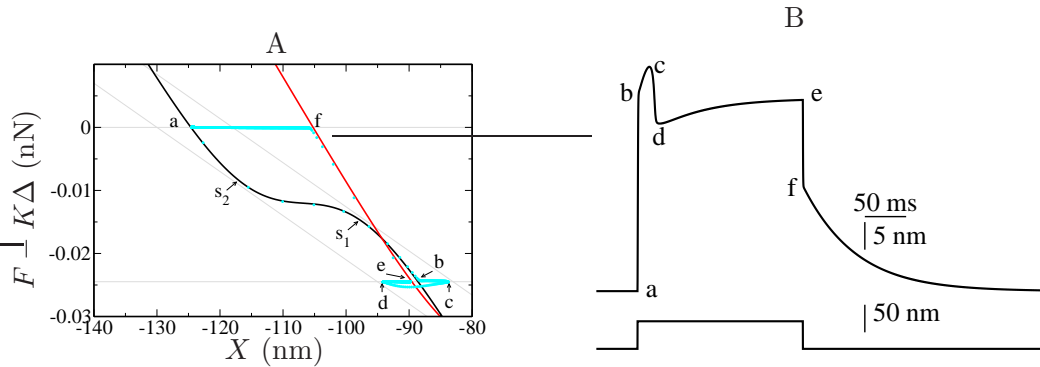


Figure 6.2: Numerical simulation for the displacement of the tip of the hair-bundle under the influence of a step displacement of the base of a flexible fiber (cyan points). Every point is separated by the same time constant, their density thereby indicating the speed of the bundle. The model used for this plot is the simple case, where the displacement-force relation does not depend on Calcium. A, displacement-force relation drawn for the motor position before the displacement (black line), and for the motor position assumed in steady state under the influence of the deflection (red line). The displacement-force relation shifts inside the corridor of grey lines, of slope $(-K_c)$, when the molecular motors change their position. The two horizontal grey lines correspond to the force applied before deflection (0-line), and after deflection $-K_F\Delta$. Intersections of the force-lines and the displacement-force relation correspond to stable stationary points, if the slope of the fore-displacement relation is negative. Initially, the bundle is found at point a, no force is applied. After the deflection of the base of the fiber, a new stable stationary point is found at position e. Before the bundle reaches this point, the direction of movement is inverted twice, one of which being a rapid movement in the negative direction (b-c), see the text for more explanations. B, the same numerical simulation, where the bundle-displacement is plotted as a function of time. The rapid part of the movement in the negative direction can resemble a twitch (c-d), but only after a certain time of slow relaxation in the positive direction (b-c). The step of the base of the fiber is indicated. Parameter values can be seen in column N of table B.2 in appendix B. Here and in the following figures of this chapter, the numerical simulations have been computed for a stimulus using a flexible fiber of $K_F = 0.34$ mN/m, with varying amplitudes of Δ , applied for 0.2 seconds.

As K_E has been chosen to be zero, the stationary opening probabilities before and after deflection are the same, corresponding to the same relative position on the displacement-force curves. The stationary open probability $P_o = 0.05$ has been chosen quite low, corresponding to experiments in high external calcium-concentration, cf 2.4.2, see also [15]. The movement of the bundle can be seen in part B of the figure, the bottom trace denotes the displacement of the base of the fiber.

As explained before, the first rapid part of the movement (a-b), corresponds to the fast relaxation of the hair-bundle's tip in close approximation to the line given by the initial displacement-force relation, because the molecular motors do not move during this rapid relaxation. After this rapid movement is concluded, the bundle is in a state of open channels and high tip-link tension. The motors slide down the stereocilium, and the position of the bundle follows the migrating movement of the shift of the displacement-force relation, at the intersection

of the constant force $-K_F\Delta$. This corresponds to a slow (because dominated by the motors) relaxation in the positive direction, as long as the slope of the displacement-force relation at the position of the bundle has a larger magnitude than the slope of the corridor, K_c .

Once the slope of F_D at the intersection with $-K_F\Delta$ gets equal to the slope of the corridor, at the turning point s_1 , the bundle inverts its direction (c) and begins to move in the negative direction. In this example, the slope of the curve due to the gating-compliance nearly vanishes, so that the speed of the bundle movement is more and more dominated by the relaxation time of the hair-bundle. Therefore, a rapid movement of the bundle in the negative direction occurs, closing the channels, until the turning point s_2 is reached (d).

The displacement-force curve has not yet reached its stationary position under the influence of the deflection, and so it continues to shift down the corridor. Therefore, the direction of the movement is inverted, and a phase of slow relaxation in the positive direction follows, until the stationary state e is reached, or until the base of the fiber is moved back.

When the base of the fiber is moved back to its original location, only the fast relaxation to point f and the slow relaxation to point a take place, because the slope of the displacement-force relation does always have a larger magnitude than $-K_c$ during this phase of the movement. No strong nonlinear effects or changes of the direction of motion take place.

Note that the twitch which can be seen in fig. 6.2 B (c-d) can only occur after a certain time of slow relaxation in the positive direction (b-c). If the bundle shows a region of negative stiffness, this backward movement occurs approximately with the time-constant of the hair-bundle, $\simeq \lambda/(K_c + K_{GS})$. If the maximum slope of the displacement-force relation is smaller than zero, the necessary shift of the curve due to the movement of the molecular motors slows down this movement.

Fig. 6.3 shows a series of steps with increasing amplitude Δ . Note the twitch which can be seen for base-displacements in the negative direction, just after the base of the fiber is moved back to its original position. This occurs due to precisely the same reasons as the twitch described so far: In the case of negative base displacement, the back-displacement to the original value can be seen as the beginning of a positive stimulus, covering the nonlinearities of the displacement-force curve. The amplitude of the twitch is nearly constant, corresponding to the distance between the two turning points s_1 and s_2 . Larger base-displacements result in a longer phase of slow positive movement before the onset of the twitch. The simple model of section 2.4 can therefore not explain the twitch which has been observed in experiments, as shown in fig. 6.12 A.

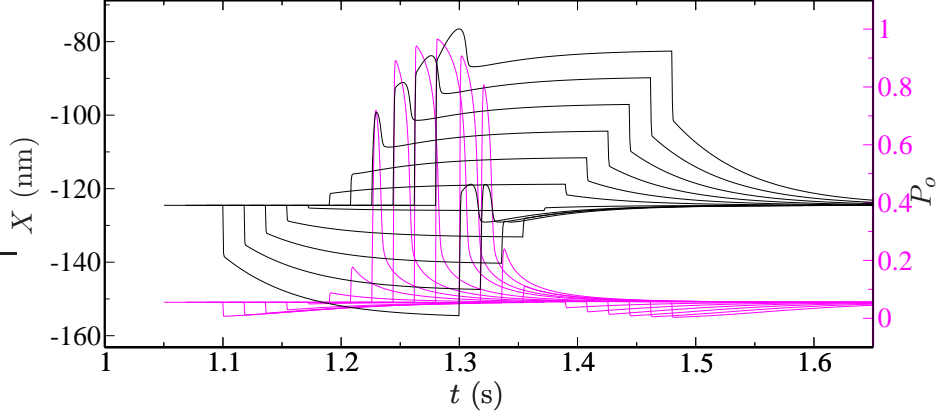


Figure 6.3: Numerical simulations for a series of base-displacements of varying amplitudes, system with a displacement-force relation which is independent of $[\text{Ca}^{2+}]$: bundle movement (black line) and open probability (magenta line). Note the twitch-like movement at the onset of the backward movement of the base for negative base displacements, which is just the mirror image of the twitch at the onset of the step displacement for positive base displacements. The step amplitude has been varied from -63 to 87 nm, in steps of 15 nm. For better readability, the onset of the displacement between successive steps has been delayed by 0.18 s. Parameters as in fig. 6.2.

6.1 Calcium-dependent free-energy change: $\Delta G(C)$

The assumption of a calcium-dependent value of the free-energy difference between the open and the closed state of the channels, $\Delta G(C)$, will still not change the form of the displacement-force relation, but merely change the offset X_{off} . This situation is nonetheless different from the one previously described, because of the calcium-dependence of the curve. Assuming relatively fast calcium-dynamics, we have now two effects influencing the displacement of the hair-bundle after the base-displacement: first, the external force will open the channels, and the bundle will relax to the position given by the intersection of the line given by the external force $K_F \Delta$ and the displacement-force relation F_D calculated with a value of X_a corresponding to the position of the molecular motors before the stimulus. Second, the increasing internal calcium-concentration will shift the displacement-force relation, which happens with the relatively short timescale of the calcium-relaxation time. But the direction of the shift will not have the same slope as the one given by a change of X_a ; this time, the shift of the displacement-force relation is given by:

$$\frac{\partial X_{off}}{\partial \Delta G} = \frac{N}{K_{GS} D} \quad (6.8)$$

$$\frac{\partial F_D(X_{off})}{\partial \Delta G} = \frac{(K_{GS} + K_c) N}{K_{GS} D} \quad , \quad (6.9)$$

resulting in a slope of $-(K_{GS} + K_c)$, which is the same as the slope of the displacement-force relation for large and small values of P_o . If the bundle is to display a negative twitch, the displacement-force relation for high calcium-concentrations should be placed in such a way that the same open probability corresponds to lower values of X as compared to the displacement-force relation for low calcium-concentrations. This can only occur if $\Delta G' > 0$. Note that this behavior (increasing ΔG with increasing $[\text{Ca}^{2+}]$) is indirectly supported by experiments, see for example subsection 2.4.2.

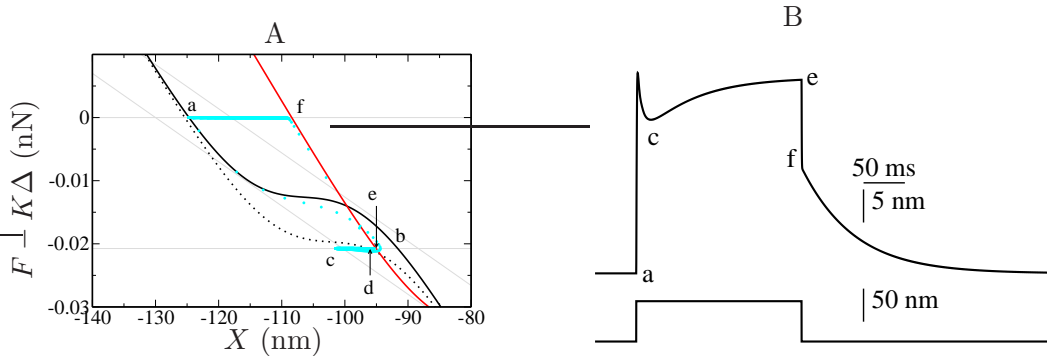


Figure 6.4: Numerical simulation for a displacement-force relation with calcium-dependent ΔG . Conventions as in figure 6.2. See text for an explanation of the situation. Parameter values can be seen in column O of table B.2 in appendix B.

Fig. 6.4 shows this situation. Now, three displacement-force relations are shown. As before, the black and the red curves show the displacement-force relations calculated using a value of X_a corresponding to the stationary value of the motors before (black) and after (red) deflection. The dotted curve demonstrates the influence of the calcium-dependence of this curve: it represents the displacement-force relation calculated with a value of X_a corresponding to the position before deflection, but with C having the value of the stationary point assumed by the system after deflection, while fixing the motor position X_a .

In other words, if X_a is fixed, and C is considered a dynamic parameter, the dotted curve corresponds to the stationary state after deflection. Therefore, if the timescales of the system were perfectly separated ($\lambda/(K_{GS} + K_c) \ll \tau \ll \lambda_a/(K_{GS})$), the system would first relax to the intersection of the force $K_F\Delta$ and the black line (b). Then, the slower calcium-dynamics would shift the curve from the black curve to the dotted one, until the system reaches d, the intersection of $-K_F\Delta$ with the dotted curve. Following this movement, the curve shifts down in the direction of the red curve, until it reaches e, the intersection of the red curve with the force $-K_F\Delta$. The return to the original position is analogous to the case described before: because everything takes place in low calcium-concentration, no important nonlinearities are encountered, and the calcium-dependent shift of the displacement-force relation is much smaller than the one observed following the

base-displacement in the positive direction.

However, the parameters of our simulation did not separate the timescales perfectly ($\lambda/(K_{GS} + K_c) = 0.18$ ms, $\tau = 1$ ms, $\lambda_a/K_{GS} = 30$ ms). That is the reason why the simulation does not entirely follow the black curve up to point b: the calcium-dependent shift begins to work, before b is reached. This is also the reason why the simulation actually shows values of X smaller than those corresponding to d: The motors begin to shift the curve down in the direction of the red curve, thereby descending the major part of the nonlinearity below the force $-K_F\Delta$, which increases the amplitude of the negatively directed movement, which finds its extremum at c. Therefore, we see that this twitch comes quite close to the ones observed in the hair-bundle.

This twitch is dependent on a moderate separation of timescales, its apparent amplitude additionally depends on an interplay between the applied force and the timescales: For large forces, the overshoot above point d cannot be observed, because the major part of the nonlinearity descends below the applied force $-K_F\Delta$ only after a phase of slow adaptation; and for a perfect separation of timescales it is equally absent. Its amplitude is also crucially dependent on the size of the gating-compliance, which can be seen as follows: a shift due to a change of ΔG shifts the displacement-force relation with a slope of $K_{GS} + K_c$. The vertical dimension of this corridor is $K_{GS}D$, its horizontal dimension is $DK_{GS}/(K_{GS} + K_c)$, the latter giving the maximum value of negative-directed movement due to a shift of the displacement-force relation because of calcium-dependent ΔG .

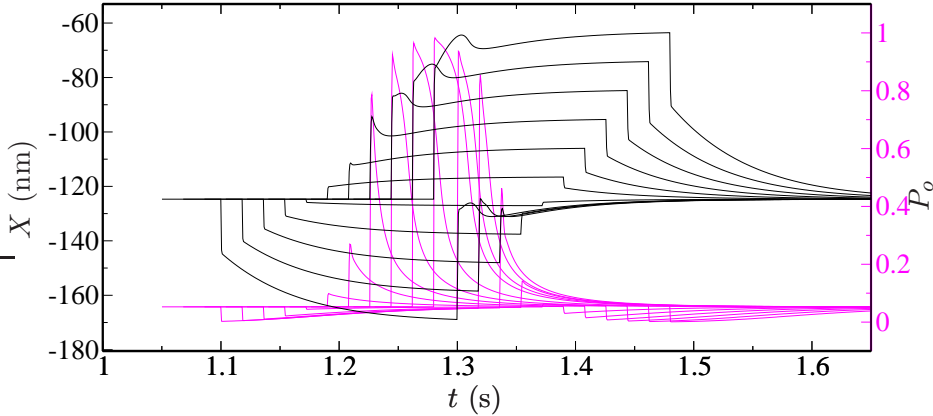


Figure 6.5: Numerical simulations for a series of base-displacements of varying amplitudes, system with $[\text{Ca}^{2+}]$ -dependent ΔG : bundle movement and open probability. Larger stimuli reduce the twitch amplitude, as described in the text. Conventions as in fig. 6.3. Stimulus amplitudes ranged from -93 to 127 nm, in steps of 21 nm. Parameters as in fig. 6.4.

Fig. 6.5 shows a series of steps-displacement. The decreasing twitch amplitude in response to larger stimuli is clearly visible. We can also see the negative-

directed movement after a phase of slow relaxation in the positive direction; this is the same phenomenon as described in the previous section, the gating-compliance resulting in the slope of the displacement-force relation being momentarily smaller in magnitude than the slope of the shift of the curve. This bump disappears with weaker gating-compliance. We conclude this section by stating that a calcium-dependent ΔG is able to show the mechanical features of the twitch, but its magnitude is varying strongly with the applied force, and for small gating compliance it is nearly absent. It is also apparent that the open probability in this case can only decrease in the limits given by the twitch-movement. Therefore, we do not see an abrupt closure of the extent to be seen in fig. 6.1.

6.2 Calcium-dependent gating-swing distance: $D(C)$

The shift of the displacement-force relation is given by:

$$\frac{\partial X_{off}}{\partial D} = -\left(\frac{N\Delta G}{K_{GS}D^2} - \frac{1}{2}\right) \quad (6.10)$$

$$\frac{\partial F_D(X_{off})}{\partial D} = (K_{GS} + K_c)\left(\frac{N\Delta G}{K_{GS}D^2} - \frac{1}{2}\right) + \frac{K_{GS}}{2} \quad , \quad (6.11)$$

resulting in the slope $-(K_{GS} + K_c) - K_{GS}/(2N\Delta G/(K_{GS}D^2) - 1)$, which now depends on the actual internal calcium-concentration, via the value of $D(C)$. The shape of the displacement-force relation now depends also on calcium: increasing D means decreasing δ and therefore a stronger gating compliance. The sign of the slope now depends on the parameters, especially on the magnitude comparing the intrinsic energy difference between open and closed states of the N channels $N\Delta G$ with that of the mechanical energy of the channels, $K_{GS}D^2$. In an environment with high $[Ca^{2+}]$, conservative estimates yield $\Delta G \simeq 10 k_B T$, $k_{GS} \simeq 0.5 \text{mN/m}$, $d \simeq 4 \text{nm}$, resulting in a negative sign for eq. 6.10 and a positive sign for eq. 6.11 (for $\gamma = 0.14$ and $N = 50$, $\frac{N\Delta G}{K_{GS}D^2} \simeq 5$). For environments with low $[Ca^{2+}]$, it might be possible that these signs become inverted, as d can become as large as 8 nm.

However, in the high calcium-concentrations we are interested in, we observe that the slope of the migration of the displacement-force relation is actually larger in magnitude than the slopes of the displacement-force relation for large and small P_o , which is $-(K_{GS} + K_c)$, providing us therefore with a large calcium-dependent shift in the negative direction. This shift only occurs if $D' < 0$, with parameters in the range of the values cited above. Note that this behavior is consistent with experiments, see subsection 2.4.2.

Fig. 6.6 shows this situation. We have a situation similar to the previous section, but the twitch being larger due to fact that the slope of the migration of the displacement-force relation has a slope of larger magnitude than the one

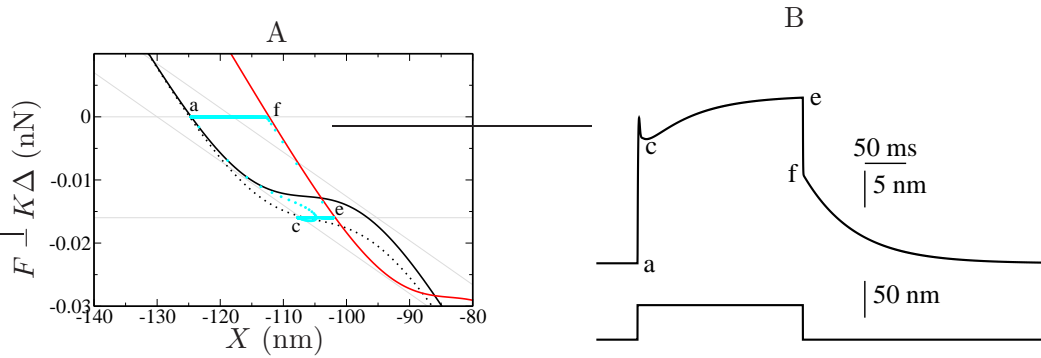


Figure 6.6: Numerical simulation for a displacement-force relation with calcium-dependent gating-swing D . Conventions as in fig. 6.4. Parameter values can be seen in column P of table B.2 in appendix B.

of the previous section 6.1. Additionally, the shape of the displacement-force relation is altered under the influence of a changing internal $[Ca^{2+}]$ concentration. This twitch-mechanism seems to provide results which come quite close to the experimental observations.

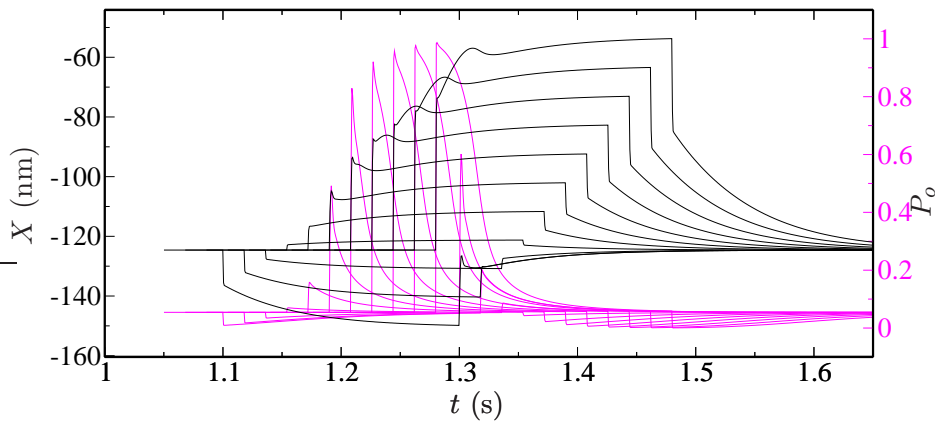


Figure 6.7: Numerical simulations for a series of base-displacements of varying amplitudes, system with calcium-dependent gating-swing $D(C)$. Conventions as in fig. 6.3. Stimulus amplitudes ranged from -53 to 147 nm, in steps of 20 nm. Parameters as in fig. 6.6.

The series of multiple steps in fig. 6.7 shows the evolution of twitch size and form with increasing amplitude of the base displacement. The twitch itself nearly disappears, whereas the bump due to the nonlinearity appears for larger stimuli. The bump can only appear when the force-step covers the nonlinearity region of the displacement-force relation completely.

As a comparison, fig. 6.8 shows the situation for a bundle with compara-

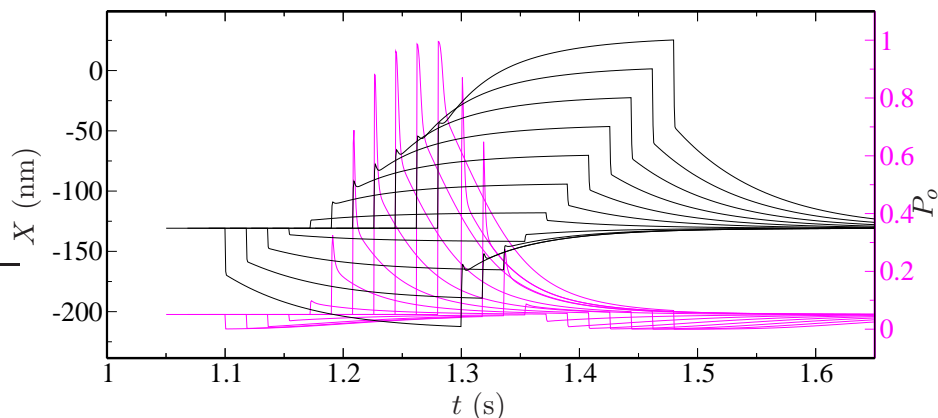


Figure 6.8: Numerical simulations for a series of base-displacements of varying amplitudes, system with $[\text{Ca}^{2+}]$ -dependent gating-swing D , but weaker gating compliance and larger calcium-dependence of D than those which have been used in fig. 6.7. Parameter values can be seen in column Q of table B.2 in appendix B. Conventions as in fig. 6.3. Stimulus amplitudes ranged from -173 to 327 nm, in steps of 50 nm.

tively weak gating compliance, but a larger dependency of D on C . Due to the larger value of δ , larger displacements are necessary to obtain a sizeable twitch. In both cases, the twitch amplitude decreases with growing forces, though this phenomenon is less important for the system having weaker gating compliance, fig. 6.8. Both strong and weak gating compliance provide the system with a brutal decrease in open probability, as seen in the experiments. The strength of this effect depends, of course, on the amplitude of the twitch.

Note that the amplitude of the twitch shown in fig. 6.8 is much smaller than the amplitude of the experimental observations [6], see also fig. 6.12. The size of the twitch depends on several parameters, including the gating-compliance, the stiffnesses, the gating-swing, and the calcium-dynamics. By varying several of the parameters, such as K_{GS} , K_{SP} , D , D' , τ , the amplitude of the twitch does also vary. It is therefore possible that the observed twitch amplitudes can be reproduced by a suitable parameter choice. However, we did not explore the parameter space sufficiently in order to obtain twitch amplitudes of 25 nm.

6.3 Calcium-dependent gating-spring stiffness: $K_{GS}(C)$

The shift of the displacement-force relation is given by:

$$\frac{\partial X_{off}}{\partial K_{GS}} = -\frac{N\Delta G}{K_{GS}^2 D} \quad (6.12)$$

$$\frac{\partial F_D(X_{off})}{\partial K_{GS}} = K_c \frac{N\Delta G}{K_{GS}^2 D} \quad , \quad (6.13)$$

resulting in the slope $-K_c$, which is the same as the one given by the motion of the molecular motors. This situation allows a twitch with $K'_{GS} < 0$ in the following way: increasing calcium-concentration after the displacement leads to a shift of the displacement-force relation down the slope. Initially, the negatively directed motion is small, but once the part with the nonlinearity is reached, this movement is accelerated.

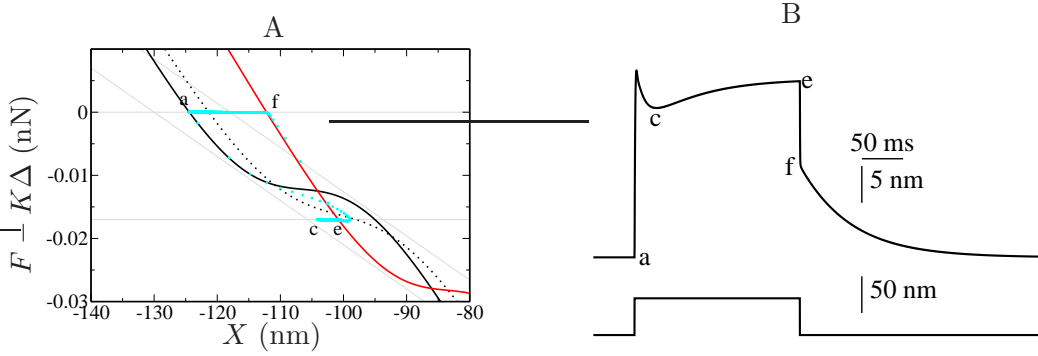


Figure 6.9: Numerical simulation for a displacement-force relation with calcium-dependent gating-spring $K_{GS}(C)$. Conventions as in fig. 6.4. Parameter values can be seen in column R of table B.2 in appendix B.

Fig. 6.9 shows this situation. As can be seen from this figure, the twitch is mainly due to the gating-compliance descending below the external force $-K_F\Delta$, and the overshoot is due to the motors beginning to shift the displacement-force relation to the red curve. This is the same phenomenon which has been described in section 6.1. The shape-change of the displacement-force relation is altered under the influence of a changing internal $[Ca^{2+}]$ concentration, resulting in a weaker gating-compliance.

The series of multiple steps in fig. 6.10 shows the evolution of twitch size and form with increasing amplitude of the base displacement. The twitch itself nearly disappears, whereas the bump due to the nonlinearity appears for larger stimuli. Low gating compliance will lead to even lower amplitudes, because the gating-compliance cannot be used for a fast negatively directed movement. The twitch is constantly low in magnitude, due to the slope of the migration of the displacement-force relation, $-K_c$, being smaller in magnitude than the limiting slope of the displacement-force relation, $-(K_c + K_{GS})$. These observations do not favor the possibility that a calcium-dependent K_{GS} is at the origin of the twitch

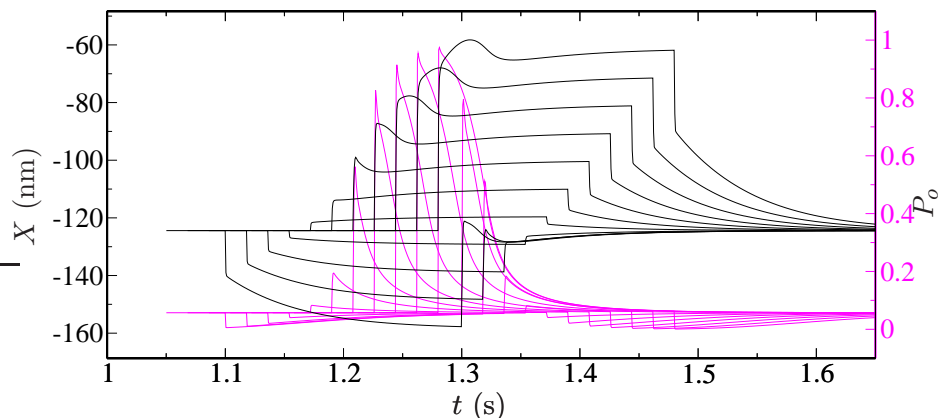


Figure 6.10: Numerical simulations for a series of base-displacements of varying amplitudes, system with calcium-dependent gating-spring $D(C)$. The bump occurs due to the gating-compliance. Conventions as in fig. 6.3. Stimulus amplitudes ranged from -70 to 130 nm, in steps of 20 nm. Parameters as in fig. 6.9.

observed in experiments. However, the positive sign of K'_{GS} , which is necessary to generate this twitching behavior, is consistent with experiments, see subsection 2.4.2.

6.4 Calcium-dependent rest-length of the gating-spring: $X_{GS}(C)$

The shift of the displacement-force relation is the same than the one which has been found at the beginning of the chapter, described by eqs. 6.6 and 6.7.

The situation is, however, slightly changed, because the short calcium-relaxation time allows the displacement-force curve to shift rapidly down the slope $-K_c$, allowing the gating-compliance to yield a fast negatively directed motion.

This situation is very similar to the one described in subsection 6.3, with the only difference that the shape of the displacement-force relation does not change. With $X'_{GS} > 0$, the system yields very similar twitches as compared to the ones described in subsection 6.3. Note that this sign is the same as the one which has been used to obtain the spontaneous oscillations in subsection 3.2.2, see fig. 3.5. However, this sign of X'_{GS} is also the opposite of the one which is necessary to mediate spontaneous oscillations described in subsection 3.2.3.

A peculiar situation arises if $X'_{GS} < 0$ (or $K'_{GS} > 0$). In this case, the displacement-force relation shifts up the corridor given by the slope $-K_c$, yielding finally two twitches: the first is a fast negatively directed movement due to the fact that the slope of the displacement-force relation has a larger magnitude

than $-K_c$, the second one is the twitch due to the gating-compliance, which we have already described.

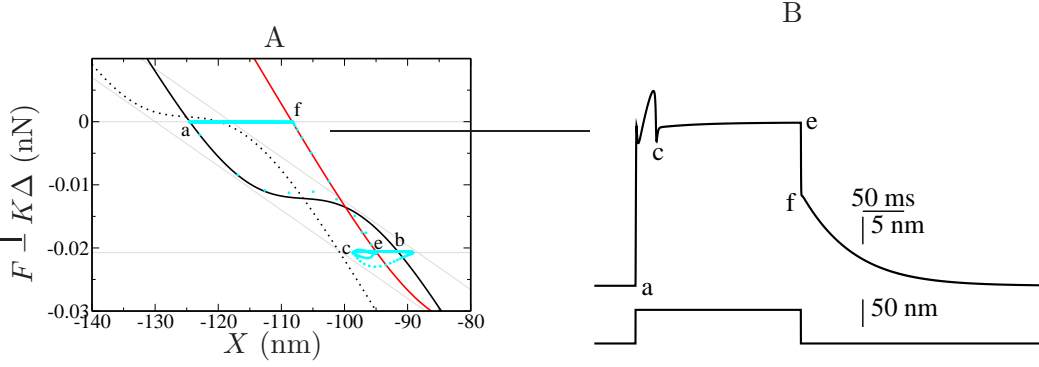


Figure 6.11: Numerical simulation for a displacement-force relation with calcium-dependent gating-swing $X_{GS}(C)$. Conventions as in fig. 6.4. Parameter values can be seen in column S of table B.2 in appendix B.

Fig. 6.11 shows this situation. The two backward twitches are nicely visible. The first twitch begins with the deviation of the trajectory from the black line, in the direction of point c. Before the system has relaxed to this point, the motors begin to move and shift the curve down the corridor, leading to the slow positive movement between the steps. Once the nonlinearity reaches the height $-K_F\Delta$, the second twitch due to the gating-compliance sets in. This kind of twitch has never been observed. The open probability does not decrease in the course of the first negatively directed movement, because point c has actually a higher open probability than point b.

6.5 Conclusion

We have shown that the simple model presented in section 2.4 is not sufficient to reproduce all of the features displayed by a hair-bundle which is subjected to step-displacements of the base of a flexible fiber attached to the bundle's tip. However, under the additional assumption of a calcium-dependence of the parameters ΔG , D , K_{GS} and X_{GS} , the system can yield a twitching behavior with different characteristics. Two mechanisms underly this rapid reaction of the bundle's tip as described by the model presented in this chapter.

First, a change of the displacement-force relationship due to an altered internal $[\text{Ca}^{2+}]$ -concentration via one of the parameters leads to a shift of the displacement-force relationship F_D in such a way that a new stationary point at the intersection between F_D and the external force $-K_F\Delta$ is rapidly assumed by the bundle position X . This shift, associated with the timescale given by the dynamics of the intracellular $[\text{Ca}^{2+}]$, has to possess a timescale situated between the fast mechan-

ical relaxation of the bundle and the slow adaptation of the motors.

Second, the nonlinearity of the displacement-force relationship (gating-compliance) can lead to a small (in magnitude) slope of F_D , so that a slow horizontal shift of this curve results in a fast movement of the bundle position. Both effects are usually combined in the twitches which we have presented.

From all the parameters analyzed, the assumption of a calcium-dependent gating-swing distance $D(C)$ results in the most robust twitch which yields results being closest to the experiments, see fig.6.12. As can be seen in part C of this figure, the amplitude of the twitch grows with the amplitude of deflection of the hair-bundle, reaches a maximum and then vanishes. As a comparison, part D of this figure shows the amplitude of the twitch obtained by numerical simulations. The simulations are in qualitative agreement with the experiments. However, the amplitude of the twitch is approximately 5 times lower than the results of the experiment.

Focusing on the linear term of the dependence of a given parameter on the calcium-concentration, we were able to determine the sign of the linear dependency. The signs which have been found necessary for our model to yield a twitching behavior have been found to be consistent with indirect experimental evidence concerning the dependence of the parameters K_{GS} , D , and ΔG on the calcium-concentration.

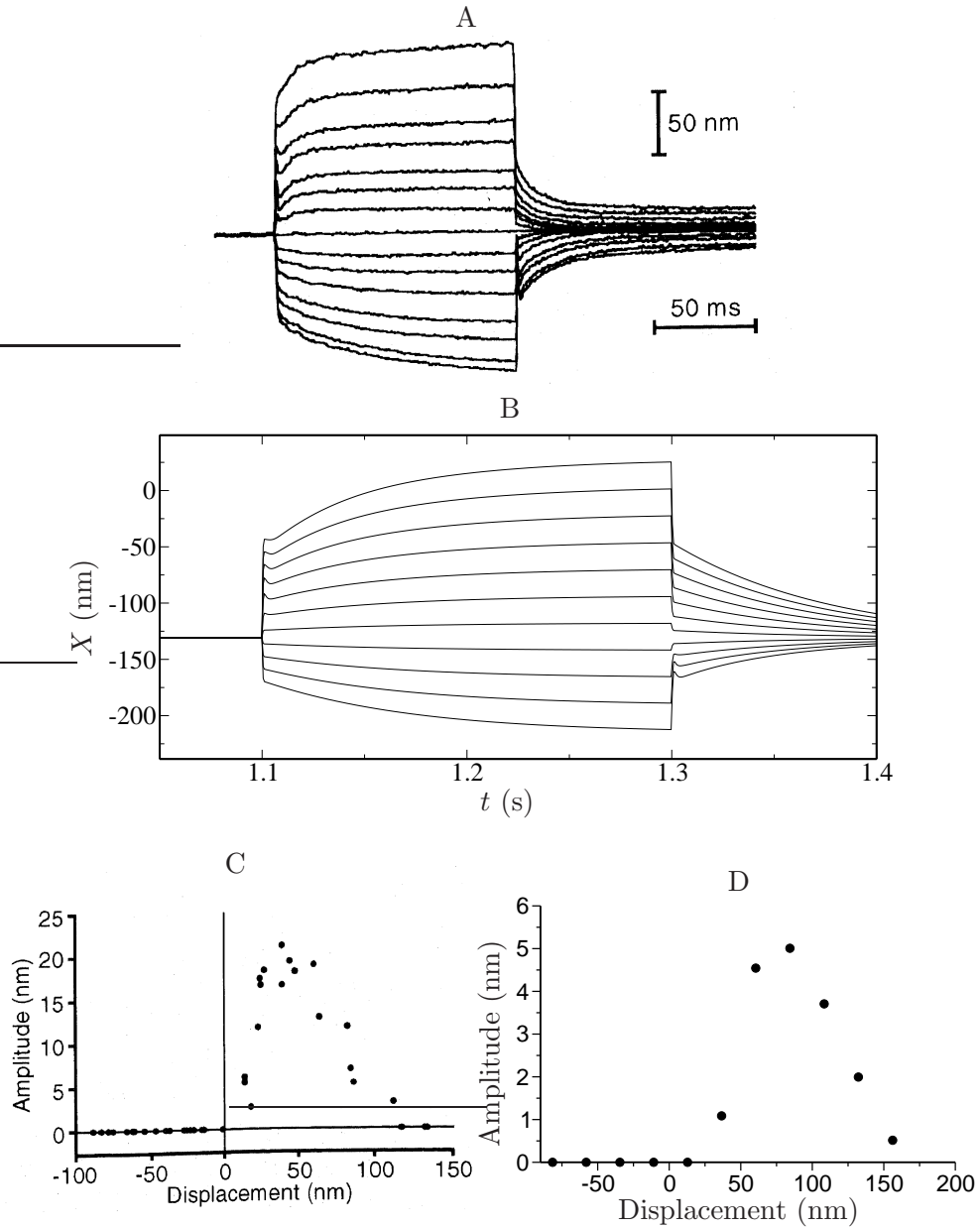


Figure 6.12: Comparison of a series of steps: experimental results and numerical simulations. The twitch varies in amplitude, being larger for intermediate values of displacements, and disappears for large and small displacements. A, Experiments conducted on hair-bundles of the bullfrog's sacculus. Taken from [6]. B, numerical simulations. Same data as fig 6.8. C, Twitch amplitude as a function of hair-bundle displacement. Taken from [6]. D, Twitch amplitude as a function of hair-bundle displacement, numerical simulations. Same data as fig. 6.8.

Chapter 7

Discussion and outlook

Active hair-bundle motility. We have presented a physical description of active hair-bundle motility. Two essential ingredients of hair-bundle spontaneous oscillations have been identified: First, a nonlinear displacement-force relationship, which describes the force with which the bundle is responding to displacements of its tip. Second, a calcium-dependence of the values of some of the parameters describing the hair-bundle mechanics. For fast calcium-relaxation times, our model displays spontaneous oscillations under the assumption of calcium-dependent motor activity. If all of the parameters are independent of the calcium-concentration, spontaneous oscillations do not take place. This mechanism relies on regions of negative stiffness in the bundle's displacement-force relation. These are regions, in which the bundle responds to deflections of its tip with a force which inclines the bundle to move even further in the direction of the deflection, instead of developing a force acting against the deflection. The molecular motors periodically push the system into regions of this negative stiffness.

Under the assumption of a linear relation between the activity of the molecular motors and the internal calcium-concentration, our model displayed spontaneous oscillations which are similar to the low-frequency oscillations ($\sim 10\text{Hz}$) observed in hair-bundles of the bullfrog's sacculus. A linear force-velocity curve characterizing the relation between an external force and the velocity of the motors was sufficient.

We have also presented other mechanisms of oscillations, including nonlinear force-velocity curves characterizing the activity of the molecular motors. These mechanisms are probably not important for the low-frequency oscillations observed in hair-bundles of the bullfrog's sacculus. However, for hair-bundles sensitive to higher frequencies, these oscillations might be of some importance.

The importance of fluctuations. Our description of active hair-bundle motility emphasizes the role played by fluctuations. The mechanical properties of oscillatory hair-bundles can be described quantitatively only if fluctuations are

taken into account. Fluctuations arise in part from Brownian motion of fluid molecules and from the stochastic gating of transduction channels. By consuming energy, the motors power frequency-selective amplification but also generate non-thermal fluctuations that add to the inevitable thermal fluctuations. We have found, however, that the magnitude of fluctuations due to active processes remain below the level of thermal noise.

In the absence of fluctuations, an operating point on the line of Hopf bifurcations in the state diagram would result in diverging sensitivity, infinite frequency selectivity and a compressive nonlinearity over many decades of stimulus magnitudes. This situation is ideal for detecting oscillatory stimuli [14, 13, 27, 56, 26]. As exemplified by our analysis, fluctuations restrict the system's sensitivity and frequency selectivity to oscillatory stimuli. They also restrict the range of stimulus magnitudes in which the compressive nonlinearity of the bundle's response occurs. Despite fluctuations, a single hair-bundle amplifies its response to small stimuli and, correspondingly, the characteristic compressive nonlinearity that arises near a Hopf bifurcation remains (fig. 5.5). One can define the gain of the amplification process as the ratio of the sensitivity at resonance to small stimuli $|\tilde{\chi}_0|$ to that to intense stimuli. Both experiments and simulations indicate that active hair-bundle motility provides a gain of about ten. Our theoretical analysis demonstrates that significant amplification happens inside the area of the state diagram where the noiseless system oscillates (fig. 5.2). Interestingly, the global optimum of mechanosensitivity is obtained at an operating point located near the center of the oscillatory region in the state diagram, that is far from the line of Hopf bifurcations of the noiseless system. Furthermore, the sensitivity is largest if the open probability of the transduction channels is 0.5. In addition, variations of $|\tilde{\chi}_0|$ to small stimuli in the state diagram mirror that of the quality factor $Q \simeq \omega_0 \Lambda / 2K$ (see for example 5.6). In particular, the point at which Q is at a global maximum is near the global optimum of sensitivity.

Sensitivity and friction. The value of the coefficient λ that characterizes the friction of the hair-bundle has a significant effect on the sensitivity $|\tilde{\chi}_0|$ that the system can achieve. Decreasing this friction coefficient to the physical limit $\lambda \simeq \lambda_h \simeq 2 \cdot 10^{-7} \text{Ns/m}$ given by hydrodynamic friction, indeed results in a threefold increase of sensitivity. This coefficient was estimated previously in experiments where the hair cells were immersed entirely in standard saline solution and did not, or very rarely, show spontaneous oscillations of their hair-bundles [23]. As the calcium-concentration in standard saline is 16 times higher than in artificial endolymph, the feedback strength $S = -C_M p' / p(0)$ is probably much stronger in standard saline. A more efficient calcium-feedback could explain why the system operates in a monostable state with transduction channels mostly closed (fig. 3.1). Under these circumstances, experiments suggest that hydrodynamic friction alone accounts for the observed hair-bundle friction. For hair-bundles immersed in artificial endolymph, our present analysis indicates instead that the contribution of

channel clatter dominates friction $\lambda \simeq \lambda_c \simeq 3 \cdot 10^{-6} \text{Ns/m}$. This apparent discrepancy can be explained by considering the calcium-dependence of the transduction channels' open probability P_o and of the channels' gating swing d . In standard saline, the channel swing and the average open probability are reduced to $d \simeq 4 \text{nm}$ [44] and $P_o \simeq 0.15$ [37, 15], which is enough to reduce the contribution of channel clatter to friction to the level of hydrodynamic friction (see Eq. 5.8). In addition, the dwell time τ_c of transduction channels is also probably shorter in standard saline than it is in artificial endolymph [88]. Faster transduction channels would yield greater mechanosensitivity than that observed so far in the bullfrog's sacculus. A dwell time of $\tau_c \simeq 1 \text{ms}$ is probably fast enough for saccular hair cells to operate in a frequency range of 5 – 130 Hz, but auditory hair cells could have shorter dwell times, therefore reduced friction λ and increased mechanosensitivity.

Twitching behavior of the hair-bundle in response to mechanical stimulations We have presented a theoretical and numerical analysis of the rapid movements of the hair-bundle's tip in response to mechanical stimulations using a flexible fiber. We have found that the simple model which has been shown to quantitatively reproduce the characteristic response of the hair-bundles spontaneous oscillations does not display all of the properties of the twitch. However, our model of the hair-bundle displays twitch-like behaviors under the assumption that some of the parameters are calcium-dependent.

If the hair-bundle is to display a twitching behavior, the timescale of the calcium-dynamics should be slower than the relaxation time of the hair-bundle's tip, but faster than the typical timescale of the molecular motors. Focusing on the general characteristics of the effects of calcium-dependent parameters, we have restricted our analysis to the linear term of the calcium-dependence, and found that the value of the gating-spring K_{GS} and of the gating swing D have to decrease with $[\text{Ca}^{2+}]$ in order to allow for the twitch, whereas the intrinsic energy difference ΔG between the open and the closed state of an ion-channel has to increase with $[\text{Ca}^{2+}]$. These results are consistent with previous experimental findings.

Outlook The hair cells of the sacculus of the bullfrog, which are sensitive to low frequencies ($\sim 5 - 130 \text{ Hz}$ [110]), display spontaneous oscillations with frequencies of the same order of magnitude. Experiments have shown, that only hair-bundles displaying spontaneous oscillations display a high sensitivity and frequency selectivity in their response to oscillatory stimuli [81, 80]. In the absence of fluctuations, the optimal operating point of the hair-bundle is the point where it undergoes the Hopf bifurcation. In the presence of fluctuations, the optimum of the sensitivity and of the frequency selectivity (which is characterized by the quality factor Q) are no longer situated in the vicinity of the Hopf bifurcation of the noiseless system, but in a region where the noiseless system displays spontaneous oscillations.

We can only speculate about what determines the operating point of the hair-bundle. It has been suggested that a general self-regulation mechanism adjusts a

control parameter of the system to bring it close to a point of high sensitivity [13]. Our model displays properties which quantitatively matches the properties of the experimental observations at a point which represented 75% of the global optimum of sensitivity. It is an important issue to identify possible parameters that the cell could regulate to optimize its behavior. Our work suggests that the feedback strength S and the maximal motor force f_{\max} are natural candidates. If the hair cell could regulate both parameters, it could achieve high sensitivity by moving towards the point where the quality factor Q is the largest. For that purpose, the hair cell might take advantage of a filter [107], such as that provided by an electrical oscillator in the basolateral membrane of the hair cell [17, 53]. The hair cell might also control one parameter, for instance if the maximal motor force f_{\max} were determined only by the intrinsic properties of the adaptation motors and the number of motors per stereocilium. By regulating S at fixed f_{\max} , the hair cell could nevertheless find an operating point of high sensitivity if the properties of the motors were of such a kind that f_{\max} fell in an appropriate range. The hair cell could regulate the feedback strength S for example by controlling the intracellular level C_0 of calcium. Such a mechanism would also affect f_{\max} .

The ability of a single hair-bundle to detect oscillatory stimuli is limited by fluctuations. This limitation could be overcome if an ensemble of hair cells with similar characteristic frequencies were mechanically coupled. Coupled noisy oscillators could approach the ideal case of a critical oscillator near a Hopf bifurcation [90]. In an intact mammalian cochlea, the gain that characterizes amplification of basilar-membrane motion is up to 10^3 [96], which can be compared to a gain of only about 10 for a single hair-bundle in the bullfrog's sacculus. This suggests that in the cochlea the effects of fluctuations of individual hair cells are reduced by the cooperative action of many oscillatory cells, independent of the oscillation mechanism.

A similar phenomenon might take place in the sacculus of the bullfrog: although the otolithic membrane probably represents a load on an individual hair cell and therefore probably decreases its sensitivity and its quality factor (fig. 5.6), it might also effectively couple several neighboring cells and thereby increasing the performance of the ensemble.

Our description of active hair-bundle mechanics has used a simplified description. Whenever it has been possible, we have used linear approximations to describe the interdependence of the parameters of the problem. The only nonlinearity in our description is represented by the dependence of the open probability on the displacement of the hair-bundle. Our hair-bundle consists of N identical stereocilia, each of them showing an identical motor-position X_a . The fluctuations present in the system have only been taken into account in their low-frequency limit, justified by the observation that the typical timescale of the slow oscillations of hair-bundles of the bullfrog's sacculus is much larger than the timescale associated with the major contributions of non-thermal noise, the channel clatter and the binding process of the molecular motors. Despite these simplifications,

our model has proven to be able to reproduce quantitatively the properties of spontaneously oscillating hair-bundles at low frequencies.

Our analysis has been inspired by the properties of the hair cells of the bullfrog's sacculus, a low-frequency hearing organ. In particular, the oscillation mechanism which has mainly been analyzed (see chapter 5), involves the displacement of the adaptation motors in order to push the bundle periodically into regions of negative stiffness. Due to the restricted velocity of the molecular motors, such a mechanism is probably much less effective at higher frequencies. Hair cells which are sensitive to frequencies higher than ~ 100 Hz could present active hair-bundle motility which relies on other physical mechanisms. Two such mechanisms have been evoked: a nonlinear force-velocity curve of ensembles of molecular motors, and a mechanism relying on an instability due to the calcium-dynamics (subsection 3.2.3).

The mechanism underlying the twitching behavior is connected to active movements of the hair-bundle [87]. Recently, it has been proposed that a calcium-dependent gating-spring stiffness mediates electrically evoked hair-bundle oscillations in the range of several hundred kHz [8]. A closer investigation of the twitching behavior, which might rely on calcium-dependent parameters, can therefore result in a better understanding of hair-bundles which are sensitive to higher frequencies.

The ears of insects do not contain hair cells. Their detection of sound is based on cuticular mechanoreceptors, where mechanical stimulation results in a squeezing or pinching of a sensory neuron [31]. Insects have developed different mechanical means to stimulate these neurons. To detect sound-pressure variations of environmental sound, some insects have developed eardrum-like flexible membranes connected with the neurons. To detect velocity waves, some insects have developed specialized antennae. Sound induces vibrations of the antennae, which is then detected by neurons situated at the base of the antennae [109, 35]. Recent experiments indicate that these sound detectors might also rely on activity [36]. It would therefore be interesting to investigate this phenomenon theoretically.

Appendix A

Table of Symbols

Table A.1: List of Symbols

Symbol	Description	First used
θ	control parameter, normal form of Hopf bifurcation	section 1.3
θ_c	critical value of θ , normal form of Hopf bifurcation	“
Z	dynamical variable, normal form of Hopf bifurcation	“
r	stability parameter, normal form of Hopf bifurcation	“
ω_0	angular frequency, normal form of Hopf bifurcation	“
u	cubic coefficient, real part, normal form of Hopf bifurcation	“
X	dynamical displacement variable	“
F	external force	“
\widehat{F}	dominant Fourier amplitude of F	“
ω	angular frequency of F	“
X_i	Fourier amplitudes of X	“
\widetilde{X}	dominant Fourier amplitude of X	“
$A(\omega, \theta)$	linear coefficient, generic response of critical oscillators	“
$B(\omega, \theta)$	cubic coefficient, generic response of critical oscillators	“
ω_c	critical value of angular frequency	“

Symbol	Description	First used
ϕ	angle between a stereocilium and the apical epithelial surface	section 2.1
Q	elevation of the insertion point of a stereocilium above the ground plate	“
k_{GS}, K_{GS}	gating-spring stiffness	“
r	radius of a stereocilium	“
h	height of a stereocilium	“
P	distance between adjacent stereocilia	“
l	extension of the gating-spring	“
x_a, X_a	position of motors	“
γ	projection factor relating the extension of the tip-link to experimentally observable motion	“
K_{SP}	bulk stiffness of the hair-bundle	section 2.1
s	shear between adjacent stereocilia	“
X_r	resting position of the hair-bundle	“
E_o	free-energy of a channel complex in open state	section 2.2
E_c	free-energy of a channel complex in closed state	“
ΔG	intrinsic free-energy difference between open and closed state	“
E_n	mechanical energy of stereocilium number n	“
N	Number of stereocilia in a hair-bundle	“
x_{SP}, X_{SP}	rest-length of the spring associated with the stereociliary pivot elements, K_{SP}	“
σ_n	state of channel-complex n ; 1 for open, 0 for closed state	“
E	mechanical energy of the whole hair-bundle	“
d, D	gating-swing distance	section 2.2
k_E, K_E	extent spring stiffness	“
x_E, X_E	rest-length of the extent spring k_E	“
x_{GS}, X_{GS}	rest-length of the gating-spring, k_{GS}	“
Z	partition function of the hair-bundle	“
z_n	partition function of stereocilia n	“
l_n	extension of gating-spring n	“
k_B	Boltzmann constant	“
T	Temperature	“
P_o	mean open probability of all the channels of a hair-bundle	“
F	forces acting on the molecular motors due to the elastic elements of the bundle;	“

Symbol	Description	First used
f_{mot}	force exerted by the elastic elements on the molecular motors of a stereocilium	section 2.2
A	coefficient used in the expression for P_o	“
N_s	number of molecular motors per stereocilium	section 2.3
f_l	external load applied to an ensemble of molecular motors	“
f_0	stall force: force which stops the spontaneous motion of an ensemble of molecular motors	“
ξ_a	inverse of slope of force-velocity relation of the molecular motors; inverse of “friction”	“
f	average force of an individual motor attached to the actin filament	“
C	Calcium-concentration inside the cell	“
C_0	Calcium-concentration inside the cell at closed channels	“
C_M	Calcium-concentration inside the cell at open channels	“
p	probability that a given motor is bound to the actin filament	“
p'	dependence of the attachment probability p on the Calcium-concentration C	“
p_0	maximum attachment probability (i. e. when $C = 0$)	“
τ	time-constant characterizing the Calcium-dynamics	“
δ	coefficient used for the expression of P_o ; indicates the strength of the nonlinearity	section 2.4
f_{max}	maximum force of the ensemble of all motors of the hair-bundle	“
S	feedback-strength	“
F_{ext}	external force applied to the tip of the hair-bundle	“
λ_a	effective friction coefficient of the molecular motors	“
R	coefficient used for the calculation of stationary states	subsection 2.4.1
R'	coefficient used for the calculation of stationary state	“
K_P	permutation of stiffnesses	“

Symbol	Description	First used
X_S	displacement necessary to activate half the maximum transduction current	subsection 2.4.2
D_S	coefficient characterizing the dependence of X_S on the external Calcium-concentration	“
X_e	adaptive shift of the displacement-current curve of the hair-bundle in response to static deflections	subsection 2.4.3
λ_{eff}	effective drag coefficient for two-dimensional description of the hair-bundle	section 3.2
k	effective stiffness for two-dimensional description of the hair-bundle	“
F_A	effective active force for two-dimensional description of the hair-bundle	“
β	coefficient characterizing the time-dependence of active adaptation for two-dimensional description of the hair-bundle	“
\bar{k}	coupling between active elements and the movement of the hair-bundle for two-dimensional description of the hair-bundle	“
$s_{1,2}$	Eigenvalues of the two-dimensional description of the hair-bundle	“
Tr	Trace of the matrix determining the two-dimensional description of the hair-bundle	“
Δ	Determinant of the matrix determining the two-dimensional description of the hair-bundle	“
K_{GP}	coefficient characterizing the nonlinearity due to channel gating on the stiffness of the bundle	“
P'_o	dependence of the open probability on the displacement of the bundle's tip	“
K_{PP}	permutation of stiffnesses including nonlinear effects due to channel gating	“
ω_c	critical frequency of spontaneous oscillations at the Hopf bifurcation	subsection 3.2.1
X_{off}	offset of the displacement-force relation $F(X)$	“
μ	parameter measuring the feedback-strength due to the Calcium-dynamics	subsection 3.2.2
$\Delta G'$	dependence of ΔG on the internal Calcium-concentration	“

Symbol	Description	First used
X'_{GS}	dependence of X_{GS} on the internal Calcium-concentration	subsection 3.2.3
$\xi_{a,3}$	cubic coefficient characterizing the nonlinear force-velocity relation for molecular motors	subsection 3.2.4
Γ	inertial coefficient for movements of the hair-bundle	“
V_a	velocity of the molecular motors	“
ω_f	frequency of stimulation of the hair-bundle	section 4.1
a	coefficient describing the dependency of $A(\omega, \theta)$ on the frequency ω	“
b	coefficient describing the dependency of $A(\omega, \theta)$ on the control parameter θ	“
$\Re(z), \Im(z)$	Real part and imaginary part of a complex variable z	“
\sim	Designates the Fourier transform	“
χ	Sensitivity of the hair-bundle with respect to sinusoidal stimuli	“
χ_0	linear part of the sensitivity, for small stimuli	“
α	Phase factor; coefficient of the generic response function	section 4.2
K	Effective stiffness; coefficient of the generic response function	“
Λ	Effective friction; coefficient of the generic response function	“
ω_s	frequency of spontaneous oscillations	section 4.3
\widehat{X}_f	Fourier mode of the system at the frequency of the stimulus	“
\widehat{X}_s	Fourier mode of the system at the frequency of the spontaneous oscillations	“
\overline{B}	cubic coupling coefficient	“
A_{eff}	effective linear response	“
$\xi(t)$	variable designing stochastic forces	section 4.4
I	intensity of noise	“
C_0	autocorrelation function	“
Δ	stimulus amplitude	section 5.1

Symbol	Description	First used
η	stochastic forces acting on the position of the bundle	section 5.2
η_a	stochastic forces acting on the position of the molecular motors	“
δc	stochastic variable indicating fluctuations in the Calcium-concentration	“
λ_c	friction coefficient due to channel clatter	“
λ_h	friction coefficient due to hydrodynamics	“
τ_c	characteristic dwell time of a channel's open and closed state	“
$\tau_{1,2}$	lifetimes of an attached respectively detached motor	“
τ_a	characteristic time of force production by a motor : $\tau_a = (\tau_1^{-1} + \tau_2^{-1})^{-1}$	“
η_m	force-fluctuations of the molecular motors due to stochastic binding/unbinding	“
T_m	“effective Temperature” indicating the intensity of the fluctuations η_m	“
η_c	force-fluctuations of the molecular motors due to variations of the Calcium-concentration	“
T_c	“effective Temperature” indicating the intensity of the fluctuations η_c	“
T_a	“effective Temperature” indicating the intensity of all the force-fluctuations of the molecular motors	“
Q	quality factor of spontaneous oscillations	section 5.3
ν	characteristic frequency of spontaneously oscillating hair-bundles: $\nu = \omega_s/2\pi$	“
$\delta\nu$	width of the peak of the spectral density of spontaneously oscillating hair-bundles	“
K_F	stiffness of the fiber used to stimulate a hair-bundle	chapter 6
K_c	combined stiffness of fiber and hair-bundle: $K_c = K_{SP} + K_F$	“
X_{off}	offset of the displacement-force relation	“
F_D	displacement-force relation in absence of the external force	

Appendix B

Parameter values

Several of the parameters used in the numerical simulations have been measured by a number of experiments. References to some of the experiments are indicated. Note that the value of K_{SP} is to be understood as $K_{SP} + K_F$, with K_F the stiffness of the flexible fiber attached to the bundle, in the simulations which reproduce experiments conducted with the help of such a fiber.

The experimental observations concerning the value of the gating-swing distance, d , display values from $\sim 2 - 9$ nm. The highest values have been measured using the two-compartment technique introduced in the introduction, and in an environment containing low values of $[\text{Ca}^{2+}]$ [82].

The value of τ , the timescale attributed to the dynamics of intracellular $[\text{Ca}^{2+}]$, is generally thought to be below 1 ms [68]. However, the reduction of this complex dynamics to only one timescale is a very strong simplification.

In this work, the calcium-dependence of the parameters has always been restricted to the linear term. This is not meant to reflect the real dependence of the parameters on the intracellular $[\text{Ca}^{2+}]$, which is a complex problem. Still, this description allows us to develop an idea of the general effects of calcium-dependent parameters.

Each column refers to a different numerical simulation, as described in the text.

Table B.1: Parameter values for the simulations

Parameter	Reference	unit	A	B	C	D	E	F	G	H	I	J	K
λ	[44]	$\mu\text{Ns}/\text{m}$		2.8				0.5	2.8	0.28	0.25	$2.8 \cdot 10^{-4}$	2.8
λ_a	[37]	$\mu\text{Ns}/\text{m}$	30		10			30			10		-10
K_{GS}	[82]	$\mu\text{N}/\text{m}$		600				800	750			600	
K_{SP}	[82]	$\mu\text{N}/\text{m}$		400				500	600	400	400	200	400
K_E	[99]	$\mu\text{N}/\text{m}$		150				0	0	150	150		150
D	[82],[44]	nm	20	17	7	40	55	61	61	61	30		40
τ	[88],[68]	ms			0.1					20	10		0.1
C_0		mM							0				
C_M		mM	0.1	varied						0.1			
ΔG	[49]	$k_B T$							10				
T		K							300				
S		1	0.2	varied		0	varied	0.65				0	
f_{\max}		pN	1050	1440	1982	352	varied	352	0			874	465
γ	[54]	1						0.14					
N	[54]	1						50					
Calcium-dependent parameters													
K'_{GS}		$\mu\text{Ns}/\text{m}/\text{mM}$							-				
D'		nm/mM							-				
X'_{GS}		nm/mM								800		-2050	-
$\Delta G'$		$k_B T/\text{mM}$								29		-	-
Parameters for nonlinear force-velocity relationship													
Γ		$\mu\text{Ns}^2/\text{m}$							-				0.01
$\lambda_{a,3}$		nNs^3/nm^3							-				10^{-11}
Fluctuations													
$\langle \eta(t)\eta(0) \rangle$		-							-				
$\langle \eta_a(t)\eta_a(0) \rangle$		-							-				
$\langle \delta_c(t)\delta_c(0) \rangle$		-							-				

Table B.2: Parameter values for the simulations

Parameter	Reference	unit	L	M	N	O	P	Q	R	S
λ	[44]	$\mu\text{Ns}/\text{m}$		2.8				0.3		
λ_a	[37]	$\mu\text{Ns}/\text{m}$		10 00				30		
K_{GS}	[82]	$\mu\text{N}/\text{m}$		750		995		862		995
K_{SP}	[82]	$\mu\text{N}/\text{m}$		600				700		
K_E	[99]	$\mu\text{N}/\text{m}$			0					
D	[82],[44]	nm		61		41.3		34.3		41.3
τ	[88],[68]	ms		0.1				1		
C_0		mM			0					
C_M		mM			0.1					
ΔG	[49]	$k_B T$			10					
T		K		300				290		
S		1	0.65	varied		0.64		0.6		0.64
f_{\max}		pN	351.7	varied		460		489.3		460
γ	[54]	1			0.14					
N	[54]	1		50				65		
Calcium-dependent parameters										
K'_{GS}		$\mu\text{Ns}/\text{m}/\text{mM}$		-				-	-2000	-
D'		nm/mM		-		-	-42	-142		-
X'_{GS}		nm/mM		-				-		-200
$\Delta G'$		$k_B T/\text{mM}$		-		10				-
Parameters for nonlinear force-velocity relationship										
Γ		$\mu\text{Ns}^2/\text{m}$								
$\lambda_{a,3}$		nNs^3/mm^3								
Fluctuations										
$\langle \eta(t)\eta(0) \rangle$		-							$2k_B T \lambda \delta(t)$	-
$\langle \eta_a(t)\eta_a(0) \rangle$		-							$2k_B T \lambda_a \delta(t)$ with $T_a = 1.5T$	-
$\langle \delta_c(t)\delta_c(0) \rangle$		-							$2C_M^2 N^{-1} 0.25\delta(t)$	-

Bibliography

- [1] B. Alberts, A. Johnson, J. Lewis, M. Raff, K. Roberts, and P. Walter. *Molecular biology of the cell*. Garland Science, New York, 4th edition, 2002.
- [2] J. F. Ashmore. A fast motile response in guinea-pig outer hair-cells - the cellular basis of the cochlear amplifier. *Journal of Physiology-London*, 388:323–347, 1987.
- [3] J. A. Assad and D. P. Corey. An active motor model for adaptation by vertebrate hair-cells. *Journal of Neuroscience*, 12(9):3291–3309, 1992.
- [4] M. Badoual, F. Jülicher, and J. Prost. Bidirectional cooperative motion of molecular motors. *Proceedings of the National Academy of Sciences of the United States of America*, 99(10):6696–6701, 2002.
- [5] C. Batters, C. P. Arthur, A. Lin, J. Porter, M. A. Geeves, R. A. Milligan, J. E. Molloy, and L. M. Coluccio. Myo1c is designed for the adaptation response in the inner ear. *Embo Journal*, 23(7):1433–1440, 2004.
- [6] M. E. Benser, R. E. Marquis, and A. J. Hudspeth. Rapid, active hair bundle movements in hair cells from the bullfrog’s sacculus. *Journal of Neuroscience*, 16(18):5629–5643, 1996.
- [7] C.I. Berlin and R.P. Bobbin, editors. *Hair Cells: Micromechanics and Hearing*. Singular Thomson Learning, San Diego, 2001.
- [8] D. Bozovic and A. J. Hudspeth. Hair-bundle movements elicited by transepithelial electrical stimulation of hair cells in the sacculus of the bullfrog. *Proceedings of the National Academy of Sciences of the United States of America*, 100(3):958–963, 2003.
- [9] W. E. Brownell, C. R. Bader, D. Bertrand, and Y. Deribaupierre. Evoked mechanical responses of isolated cochlear outer hair-cells. *Science*, 227(4683):194–196, 1985.
- [10] S. Burlacu, W. D. Tap, E. A. Lumpkin, and A. J. Hudspeth. Atpase activity of myosin in hair bundles of the bullfrog’s sacculus. *Biophysical Journal*, 72(1):263–271, 1997.

- [11] G. von Békésy. *Experiments in Hearing*. American Institute of Physics, New York, 1989.
- [12] S. Camalet. *Oscillations critiques de systèmes biologiques. Du battement ciliaire à la détection du son*. PhD thesis, Université Paris VI, 2001.
- [13] S. Camalet, T. Duke, F. Jülicher, and J. Prost. Auditory sensitivity provided by self-tuned critical oscillations of hair cells. *Proceedings of the National Academy of Sciences of the United States of America*, 97(7):3183–3188, 2000.
- [14] Y. Choe, M. O. Magnasco, and A. J. Hudspeth. A model for amplification of hair-bundle motion by cyclical binding of Ca^{2+} to mechano-electrical-transduction channels. *Proceedings of the National Academy of Sciences of the United States of America*, 95(26):15321–15326, 1998.
- [15] D. P. Corey and A. J. Hudspeth. Kinetics of the receptor current in bullfrog saccular hair-cells. *Journal of Neuroscience*, 3(5):962–976, 1983.
- [16] A. C. Crawford, M. G. Evans, and R. Fettiplace. The actions of calcium on the mechano-electrical transducer current of turtle hair-cells. *Journal of Physiology-London*, 434:369–398, 1991.
- [17] A. C. Crawford and R. Fettiplace. An electrical tuning mechanism in turtle cochlear hair-cells. *Journal of Physiology-London*, 312(MAR):377–412, 1981.
- [18] A. C. Crawford and R. Fettiplace. The mechanical-properties of ciliary bundles of turtle cochlear hair-cells. *Journal of Physiology-London*, 364(JUL):359, 1985.
- [19] P. Dallos. The active cochlea. *Journal of Neuroscience*, 12(12):4575–4585, 1992.
- [20] P. Dallos, A. N. Popper, and R. R. Fay, editors. *The Cochlea*. Springer, New York Berlin Heidelberg, 1996.
- [21] H. Davis. An active process in cochlear mechanics. *Hearing Research*, 9(1):79–90, 1983.
- [22] W. Denk, J. R. Holt, G. M. G. Shepherd, and D. P. Corey. Calcium imaging of single stereocilia in hair cells: Localization of transduction channels at both ends of tip links. *Neuron*, 15(6):1311–1321, 1995.
- [23] W. Denk, W. W. Webb, and A. J. Hudspeth. Mechanical properties of sensory hair bundles are reflected in their brownian-motion measured with a laser differential interferometer. *Proceedings of the National Academy of Sciences of the United States of America*, 86(14):5371–5375, 1989.

- [24] P. van Dijk, H. P. Wit, and J. M. Segenhout. Spontaneous otoacoustic emissions in the european edible frog (*rana-esculenta*) - spectral details and temperature-dependence. *Hearing Research*, 42(2-3):273–282, 1989.
- [25] T. Duke. Push or pull? teams of motor proteins have it both ways. *Proceedings of the National Academy of Sciences of the United States of America*, 99(10):6521–6523, 2002.
- [26] T. Duke and F. Jülicher. Active traveling wave in the cochlea. *Physical Review Letters*, 90(15):158101, 2003.
- [27] V. M. Eguiluz, M. Ospeck, Y. Choe, A. J. Hudspeth, and M. O. Magnasco. Essential nonlinearities in hearing. *Physical Review Letters*, 84(22):5232–5235, 2000.
- [28] R. Fettiplace and A. J. Ricci. Adaptation in auditory hair cells. *Current Opinion in Neurobiology*, 13(4):446–451, 2003.
- [29] R. Fettiplace, A. J. Ricci, and C. M. Hackney. Clues to the cochlear amplifier from the turtle ear. *Trends in Neurosciences*, 24(3):169–175, 2001.
- [30] J. E. Frank, V. Markin, and F. Jaramillo. Characterization of adaptation motors in saccular hair cells by fluctuation analysis. *Biophysical Journal*, 83(6):3188–3201, 2002.
- [31] A. S. French. Mechanotransduction. *Annual Review of Physiology*, 54:135–152, 1992.
- [32] P. G. Gillespie and R. G. Walker. Molecular basis of mechanosensory transduction. *Nature*, 413(6852):194–202, 2001.
- [33] T. Gold. Hearing .2. the physical basis of the action of the cochlea. *Proceedings of the Royal Society of London Series B-Biological Sciences*, 135(881):492–498, 1948.
- [34] T. Gold and R. J. Pumphrey. Hearing .1. the cochlea as a frequency analyzer. *Proceedings of the Royal Society of London Series B-Biological Sciences*, 135(881):462–491, 1948.
- [35] M. C. Gopfert and D. Robert. The mechanical basis of drosophila audition. *Journal of Experimental Biology*, 205(9):1199–1208, 2002.
- [36] M.C. Gopfert and D. Robert. Motion generation by Drosophila mechanosensory neurons. *Proc. Natl. Acad. Sci. U. S. A.*, 100:5514–5519, 2003.
- [37] N. Hacohen, J. A. Assad, W. J. Smith, and D. P. Corey. Regulation of tension on hair-cell transduction channels - displacement and calcium dependence. *Journal of Neuroscience*, 9(11):3988–3997, 1989.

- [38] H. von Helmholtz. *Die Lehre von den Tonempfindungen als Physiologische Grundlage fuer die Theorie der Musik*. Vieweg, Braunschweig, 1913.
- [39] H. Higuchi and S. A. Endow. Directionality and processivity of molecular motors. *Current Opinion in Cell Biology*, 14(1):50–57, 2002.
- [40] J. R. Holt, D. P. Corey, and R. A. Eatock. Mechanoelectrical transduction and adaptation in hair cells of the mouse utricle, a low-frequency vestibular organ. *Journal of Neuroscience*, 17(22):8739–8748, 1997.
- [41] J. R. Holt, S. K. H. Gillespie, D. W. Provance, K. Shah, K. M. Shokat, D. P. Corey, J. A. Mercer, and P. G. Gillespie. A chemical-genetic strategy implicates myosin-1c in adaptation by hair cells. *Cell*, 108(3):371–381, 2002.
- [42] T. Holton and A. J. Hudspeth. The transduction channel of hair-cells from the bullfrog characterized by noise-analysis. *Journal of Physiology-London*, 375:195–227, 1986.
- [43] J. Howard and A. J. Hudspeth. Mechanical relaxation of the hair bundle mediates adaptation in mechanoelectrical transduction by the bullfrogs saccular hair cell. *Proceedings of the National Academy of Sciences of the United States of America*, 84(9):3064–3068, 1987.
- [44] J. Howard and A. J. Hudspeth. Compliance of the hair bundle associated with gating of mechanoelectrical transduction channels in the bullfrogs saccular hair cell. *Neuron*, 1(3):189–199, 1988.
- [45] J. Howard, W. M. Roberts, and A. J. Hudspeth. Mechanoelectrical transduction by hair-cells. *Annual Review of Biophysics and Biophysical Chemistry*, 17:99–124, 1988.
- [46] A. J. Hudspeth. Mechanoelectrical transduction by hair-cells in the acoustico-lateralis sensory system. *Annual Review of Neuroscience*, 6:187–215, 1983.
- [47] A. J. Hudspeth. Transduction and tuning by vertebrate hair-cells. *Trends in Neurosciences*, 6(9):366–369, 1983.
- [48] A. J. Hudspeth. How the ears works work. *Nature*, 341(6241):397–404, 1989.
- [49] A. J. Hudspeth. Hair-bundle mechanics and a model for mechanoelectrical transduction by hair cells. In D. P. Corey and Roper S. D., editors, *Sensory Transduction*, pages 357–370. Rockefeller university press, 1992.
- [50] A. J. Hudspeth. How hearing happens. *Neuron*, 19(5):947–950, 1997.
- [51] A. J. Hudspeth. Mechanical amplification of stimuli by hair cells. *Current Opinion in Neurobiology*, 7(4):480–486, 1997.

- [52] A. J. Hudspeth and P. G. Gillespie. Pulling springs to tune transduction - adaptation by hair-cells. *Neuron*, 12(1):1–9, 1994.
- [53] A. J. Hudspeth and R. S. Lewis. A model for electrical resonance and frequency tuning in saccular hair-cells of the bull-frog, *rana-catesbeiana*. *Journal of Physiology-London*, 400:275–297, 1988.
- [54] R. A. Jacobs and A. J. Hudspeth. Ultrastructural correlates of mechano-electrical transduction in hair-cells of the bullfrogs internal ear. *Cold Spring Harbor Symposia on Quantitative Biology*, 55:547–561, 1990.
- [55] F. Jülicher, A. Ajdari, and J. Prost. Modeling molecular motors. *Reviews of Modern Physics*, 69(4):1269–1281, 1997.
- [56] F. Jülicher, D. Andor, and T. Duke. Physical basis of two-tone interference in hearing. *Proceedings of the National Academy of Sciences of the United States of America*, 98(16):9080–9085, 2001.
- [57] F. Jülicher and J. Prost. Cooperative molecular motors. *Physical Review Letters*, 75(13):2618–2621, 1995.
- [58] F. Jülicher, J. Prost, and P. Martin. Spontaneous oscillations and noise near a hopf bifurcation: A description of hair-bundle oscillations. unpublished.
- [59] B. Kachar, W. E. Brownell, R. Altschuler, and J. Fex. Electrokinetic shape changes of cochlear outer hair-cells. *Nature*, 322(6077):365–368, 1986.
- [60] B. Kachar, M. Parakkal, M. Kurc, Y. Zhao, and P. G. Gillespie. High-resolution structure of hair-cell tip links. *Proceedings of the National Academy of Sciences of the United States of America*, 97(24):13336–13341, 2000.
- [61] N. G. van Kampen. *Stochastic Processes in Physics and Chemistry*. North-Holland Personal Library, Amsterdam, revised and enlarged edition edition, 1992.
- [62] H. Koyama, E. R. Lewis, E. L. Leverenz, and R. A. Baird. Acute seismic sensitivity in the bullfrog ear. *Brain Research*, 250(1):168–172, 1982.
- [63] H. Kunz. Introduction aux systeme dynamiques. In S. Ciliberto, T. Dauxois, and M. Droz, editors, *Physics of Complexity*. Editions Frontieres, Gif-sur-Yvette, 1995.
- [64] C. Köppl and G. A. Manley. Spontaneous otoacoustic emissions in the bob-tail lizard .1. general-characteristics. *Hearing Research*, 71(1-2):157–169, 1993.
- [65] L.D. Landau and E.M. Lifschitz. *Lehrbuch der theoretischen Physik - Band V - Statistische Physik*. Akademie Verlag, Berlin, 1966.

- [66] S. Leibler and D. A. Huse. Porters versus rowers - a unified stochastic-model of motor proteins. *Journal of Cell Biology*, 121(6):1357–1368, 1993.
- [67] E. A. Lumpkin and A. J. Hudspeth. Detection of ca^{2+} entry through mechanosensitive channels localizes the site of mechano-electrical transduction in hair-cells. *Proceedings of the National Academy of Sciences of the United States of America*, 92(22):10297–10301, 1995.
- [68] E. A. Lumpkin and A. J. Hudspeth. Regulation of free ca^{2+} concentration in hair-cell stereocilia. *Journal of Neuroscience*, 18(16):6300–6318, 1998.
- [69] E. A. Lumpkin, R. E. Marquis, and A. J. Hudspeth. The selectivity of the hair cell's mechano-electrical-transduction channel promotes ca^{2+} flux at low ca^{2+} concentrations. *Proceedings of the National Academy of Sciences of the United States of America*, 94(20):10997–11002, 1997.
- [70] M. O. Magnasco. A wave traveling over a hopf instability shapes the cochlear tuning curve. *Physical Review Letters*, 90(5), 2003.
- [71] G. A. Manley. Evidence for an active process and a cochlear amplifier in nonmammals. *Journal of Neurophysiology*, 86(2):541–549, 2001.
- [72] G. A. Manley and L. Gallo. Otoacoustic emissions, hair cells, and myosin motors. *Journal of the Acoustical Society of America*, 102(2):1049–1055, 1997.
- [73] G. A. Manley, L. Gallo, and C. Köppl. Spontaneous otoacoustic emissions in two gecko species, gekko gekko and eublepharis macularius. *Journal of the Acoustical Society of America*, 99(3):1588–1603, 1996.
- [74] G. A. Manley, D. L. Kirk, C. Köppl, and G. K. Yates. In vivo evidence for a cochlear amplifier in the hair-cell bundle of lizards. *Proceedings of the National Academy of Sciences of the United States of America*, 98(5):2826–2831, 2001.
- [75] G. A. Manley and C. Köppl. Phylogenetic development of the cochlea and its innervation. *Current Opinion in Neurobiology*, 8(4):468–474, 1998.
- [76] V. S. Markin and A. J. Hudspeth. Gating-spring models of mechano-electrical transduction by hair-cells of the internal ear. *Annual Review of Biophysics and Biomolecular Structure*, 24:59–83, 1995.
- [77] R. E. Marquis and A. J. Hudspeth. Effects of extracellular ca^{2+} concentration on hair-bundle stiffness and gating-spring integrity in hair cells. *Proceedings of the National Academy of Sciences of the United States of America*, 94(22):11923–11928, 1997.

- [78] P. Martin, D. Bozovic, Y. Choe, and A. J. Hudspeth. Spontaneous oscillation by hair bundles of the bullfrog's sacculus. *Journal of Neuroscience*, 23(11):4533–4548, 2003.
- [79] P. Martin and A. J. Hudspeth. Active hair-bundle movements can amplify a hair cell's response to oscillatory mechanical stimuli. *Proceedings of the National Academy of Sciences of the United States of America*, 96(25):14306–14311, 1999.
- [80] P. Martin and A. J. Hudspeth. Compressive nonlinearity in the hair bundle's active response to mechanical stimulation. *Proceedings of the National Academy of Sciences of the United States of America*, 98(25):14386–14391, 2001.
- [81] P. Martin, A. J. Hudspeth, and F. Jülicher. Comparison of a hair bundle's spontaneous oscillations with its response to mechanical stimulation reveals the underlying active process. *Proceedings of the National Academy of Sciences of the United States of America*, 98(25):14380–14385, 2001.
- [82] P. Martin, A. D. Mehta, and A. J. Hudspeth. Negative hair-bundle stiffness betrays a mechanism for mechanical amplification by the hair cell. *Proceedings of the National Academy of Sciences of the United States of America*, 97(22):12026–12031, 2000.
- [83] B. Nadrowski, P. Martin, and F. Jülicher. Active hair-bundle motility harnesses noise to operate near an optimum of mechanosensitivity. *Proceedings of the National Academy of Sciences of the United States of America*, 101(33):12195–12200, 2004.
- [84] S. M. van Netten, T. Dinklo, W. Marcotti, and C. J. Kros. Channel gating forces govern accuracy of mechano-electrical transduction in hair cells. *Proceedings of the National Academy of Sciences of the United States of America*, 100(26):15510–15515, 2003.
- [85] M. Ospeck, V. M. Eguiluz, and M. O. Magnasco. Evidence of a hopf bifurcation in frog hair cells. *Biophysical Journal*, 80(6):2597–2607, 2001.
- [86] J. O. Pickles. *An introduction to the physiology of hearing*. Academic Press, 2nd edition, 2003.
- [87] A. J. Ricci, A. C. Crawford, and R. Fettiplace. Active hair bundle motion linked to fast transducer adaptation in auditory hair cells. *Journal of Neuroscience*, 20(19):7131–7142, 2000.
- [88] A. J. Ricci, A. C. Crawford, and R. Fettiplace. Tonotopic variation in the conductance of the hair cell mechanotransducer channel. *Neuron*, 40(5):983–990, 2003.

- [89] A. J. Ricci, Y. C. Wu, and R. Fettiplace. The endogenous calcium buffer and the time course of transducer adaptation in auditory hair cells. *Journal of Neuroscience*, 18(20):8261–8277, 1998.
- [90] T. Risler, J. Prost, and F. Jülicher. Universal critical behavior of noisy coupled oscillators. *Physical Review Letters*, 93(17), 2004.
- [91] D. Riveline, A. Ott, F. Jülicher, D. A. Winkelmann, O. Cardoso, J. J. Lacapere, S. Magnusdottir, J. L. Viovy, L. Gorre-Talini, and J. Prost. Acting on actin: the electric motility assay. *European Biophysics Journal with Biophysics Letters*, 27(4):403–408, 1998.
- [92] W. M. Roberts, J. Howard, and A. J. Hudspeth. Hair-cells - transduction, tuning, and transmission in the inner-ear. *Annual Review of Cell Biology*, 4:63–92, 1988.
- [93] L. Robles and M. A. Ruggero. Mechanics of the mammalian cochlea. *Physiological Reviews*, 81(3):1305–1352, 2001.
- [94] L. Robles, M. A. Ruggero, and N. C. Rich. Basilar-membrane mechanics at the base of the chinchilla cochlea .1. input-output functions, tuning curves, and response phases. *Journal of the Acoustical Society of America*, 80(5):1364–1374, 1986.
- [95] J. G. Roederer. *The Physics and Psychophysics of Music*. Springer Verlag, New York, 1995.
- [96] M. A. Ruggero, N. C. Rich, A. Recio, S. S. Narayan, and L. Robles. Basilar-membrane responses to tones at the base of the chinchilla cochlea. *Journal of the Acoustical Society of America*, 101(4):2151–2163, 1997.
- [97] M. A. Ruggero, L. Robles, and N. C. Rich. Basilar-membrane mechanics at the base of the chinchilla cochlea .2. responses to low-frequency tones and relationship to microphonics and spike initiation in the viii nerve. *Journal of the Acoustical Society of America*, 80(5):1375–1383, 1986.
- [98] P. M. Sellick, R. Patuzzi, and B. M. Johnstone. Measurement of basilar-membrane motion in the guinea-pig using the mossbauer technique. *Journal of the Acoustical Society of America*, 72(1):131–141, 1982.
- [99] G. M. G. Shepherd and D. P. Corey. The extent of adaptation in bullfrog saccular hair-cells. *Journal of Neuroscience*, 14(10):6217–6229, 1994.
- [100] G. M. G. Shepherd, D. P. Corey, and S. M. Block. Actin cores of hair-cell stereocilia support myosin motility. *Proceedings of the National Academy of Sciences of the United States of America*, 87(21):8627–8631, 1990.

- [101] J. Siemens, C. Lillo, R. A. Dumont, A. Reynolds, D. S. Williams, P. G. Gillespie, and U. Muller. Cadherin 23 is a component of the tip link in hair-cell stereocilia. *Nature*, 428(6986):950–955, 2004.
- [102] C. Sollner, G. J. Rauch, J. Siemens, R. Geisler, S. C. Schuster, U. Muller, and T. Nicolson. Mutations in cadherin 23 affect tip links in zebrafish sensory hair cells. *Nature*, 428(6986):955–959, 2004.
- [103] R. L. Stratonovich. *Topics in the Theory of Random Noise*. Gordon and Breach, New York, 1963.
- [104] S. T. Strogatz. *Nonlinear Dynamics and Chaos*. Addison-Wesley, Reading, MA, 1997.
- [105] G. Taschenberger and G. A. Manley. Spontaneous otoacoustic emissions in the barn owl. *Hearing Research*, 110(1-2):61–76, 1997.
- [106] L. G. Tilney, E. H. Egelman, D. J. Derosier, and J. C. Saunders. Actin-filaments, stereocilia, and hair-cells of the bird cochlea .2. packing of actin-filaments in the stereocilia and in the cuticular plate and what happens to the organization when the stereocilia are bent. *Journal of Cell Biology*, 96(3):822–834, 1983.
- [107] A. Vilfan and T. Duke. Two adaptation processes in auditory hair cells together can provide an active amplifier. *Biophysical Journal*, 85(1):191–203, 2003.
- [108] R. H. Withnell, L. A. Shaffer, and D. J. Lilly. What drives mechanical amplification in the mammalian cochlea? *Ear and Hearing*, 23(1):49–57, 2002.
- [109] D. D. Yager. Structure, development, and evolution of insect auditory systems. *Microscopy Research and Technique*, 47(6):380–400, 1999.
- [110] X. L. Yu, E. R. Lewis, and D. Feld. Seismic and auditory tuning curves from bullfrog saccular and amphibian papillar axons. *Journal of Comparative Physiology a-Sensory Neural and Behavioral Physiology*, 169(2):241–248, 1991.

Résumé

L'oreille interne est un des organes sensoriels les plus importants chez les vertébrés. Elle fait preuve d'une performance extraordinaire, avec une grande gamme dynamique, une excellente discrimination fréquentielle et une grande sensibilité.

Il s'agit d'un système qui fait preuve d'activité : l'oreille interne peut émettre des ondes sonores, un phénomène appelé émissions spontanées oto-acoustique.

Le sens d'audition est basé sur la transformation de stimuli mécaniques en stimuli électriques, tâche accomplie par la cellule sensorielle de l'oreille interne, la cellule ciliée. L'organelle mécanosensible de la touffe ciliée est la touffe ciliaire. Les touffes ciliaires du sacculé de la grenouille peuvent osciller d'une manière spontanée. Ces oscillations spontanées sont donc un candidat naturel pour la source d'activité de l'oreille interne.

Ce travail est une étude théorique des propriétés mécaniques de la touffe ciliaire.

Nous discutons les principes physiques qui sous-tendent la détection d'oscillations basée sur des oscillateurs critiques, ainsi qu'une description détaillée de mécanismes spécifiques qui peuvent mener à un comportement actif et des oscillations spontanées de touffes ciliaires. Nous présentons un diagramme d'états et nous montrons que des fluctuations ont une influence majeure sur les fonctions de réponse du système. Nous discutons des sources différentes de fluctuations et estimons leurs influences sur les propriétés mécaniques de la touffe ciliaire. Les fonctions de réponse linéaire et non-linéaire calculées numériquement sont en accord quantitatif avec des expériences.

Abstract

The inner ear is one of the most important sensitive organs of all vertebrates. It shows an extraordinary performance, with a large dynamic range, high sensitivity and an exquisite frequency selectivity.

The inner ear is not simply a passive detector, but a nonlinear active amplifier. The most striking manifestation of this activity is the fact that the ear does not only detect sound, but it can also emit one to several tones: the so-called spontaneous oto-acoustic emissions.

The auditory sense is based on the transformation of mechanical stimuli into electrical signals, which is done by the sensory cells of the inner ear, the haircells. The mechanosensitive organelle of the haircell is the hair-bundle.

Hair-bundles are active structures, they are namely displaying spontaneous oscillations. These spontaneous oscillations are a natural candidate for the active process underlying the activity of the inner ear. This work is a theoretical study of the mechanical properties of the hair-bundle.

We discuss the physical principles underlying detection based on critical oscillations as well as specific mechanisms that can lead to oscillations and active behavior by hair-bundles. We present a simple description of active hair-bundle mechanics. We calculate the state diagram and show that fluctuations fundamentally change the mechanical response functions. We discuss different sources of fluctuations and estimate their influence on the hair-bundle's mechanical properties. Furthermore, the linear and nonlinear response functions calculated numerically account for the observed properties of active hair-bundles.